Crack bridging of surface structured z-reinforcements in CFRP laminates

Manuel Tiago von Hafe Pérez Ferreira da Silva

Dissertação de Mestrado

Orientador na FEUP: Prof. Paulo Tavares de Castro, Prof. Pedro Ponces Camanho

Orientador na empresa: Eng. Michael Juergens

Mestrado Integrado em Engenharia Mecânica

Janeiro 2016

To my parents, Teresa and Tiago,
for their encouragement and support.

Framework

The current work presents and concludes investigations carried out over a period of eleven months (February to December 2015) with “Airbus Group Innovations” of Airbus Group, department of Metallic Technologies & Surface Engineering, located in Munich, Germany.

This research was part of the public funded "Transhybrid" project (Federal Ministry of Education and Research, Germany, (BMBF)), dedicated to the development of innovative joining technologies in a multi material design environment.

Within this period, one scientific article was submitted for publication [1] and contributions to other two publications [2, 3] were made by the author of this work.

Abstract

Mode I and mixed-mode I/II testing methods are proposed to determine the pull- and shear-out failure behaviour of interleaving mettalic z-reinforcements in fibres-reinforced polymer (CFRP) laminates. A detailed description of the mechanics involved during the distinct bridging stages is presented, with respect to the reinforcements' material and means of applied surface pretreatment, supported by theoretical approaches based on structural-micromechanics on a single-pin level. Comprehensive research suggests an elastically dominated failure of traditional carbon-fibre (CF) z-pins under both mode I and mode II loading conditions. An additional stage of plasticization, supported by improved surface pretreatment induced adhesion properties and macroscopic mechanical interlocking of an undercut pin geometry, resulted in better energy absorption capacities of the novel z-reinforcing technology under investigation in the current work.

Mechanical, wet-chemical and physical applied pretreatments create a macro-, micro- and nano-scaled surface morphology, respectively, on both, stainless steel and titanium reinforcements. Enhanced adhesion features of a clean and chemically activated nano-structured spike's surface endures, on the one hand, higher bridgigng forces prior to adhesive failure but lacks of frictional attributes after pins have debonded. Both, a large macro roughness surface morphology resulting from a Al_2O_3 blasting treatment and a low mismatch between CTE of metallic z-reinforcements and surrounding laminate seem to determine the energy dissipation capacity during pull- and shear-out tests due to increased mechanical interlocking and coefficients of friction at the debonded interface.

Experimental single-pin pull- and shear-out derived bridging laws can be used for describing and predicting the delamination process of more complex z-reinforced structures. Hence, an analytical model for mode I delamination resistance, based on that developed for z-pinning, is adapted. However, particular necessary assumptions considered in this model resulted in a quantitative divergence between simulated and theoretical results.

Acknowledgments

First and foremost, I would like to express my sincerest gratitude to my supervisor at the company, Michael Juergens, for giving me the opportunity to work at Airbus Group Innovations. All you taught me, the constructive criticism, the constant assistance and the cheerful and relaxed but serious (when it had to be) atmosphere at work were essential for moving forward with my investigations.

I am also very thankful to my local supervisors at FEUP, Prof. Paulo Tavares de Castro and Prof. Pedro Ponces Camanho, for all the support and guidance given during this period in all kinds of matters, which were not always related with my Master thesis.

To my colleagues and friends I have made at Airbus Group, Steffen Reichler, Gabriel de la Cruz, Norbert Karpen, Beatriz Rico Oller, Luigi Aloé, Carina Costa, Benedikt Rauh and Jana Haag, I want to thank you for integrating me so rapidly on the company's day-to-day life and for turning this year of mine in Munich into a fantastic experience.

Last but not least, to my parents and brother and sister that were always present and whose advice, patience, support and constant encouregement, that started long before this time, allowed me to arrive where I am today. Thank you.

Contents

Acronyms list

NDT	Non-destructive testing
CF	Carbon-fibre
FRP	Fibre-Reinforced Polymer
CFRP	Fibres-Reinforced Polymer
CTE	Coefficient of Thermal Expansion
CMT	Cold-metal-transfer
HYPER	Hybrid penetrative reinforcement
ALM	Additive Layer Manufacturing
TRL	Technology Readiness Level
DCB	Double-Cantilever-Beam
PC	Polycarbonate
UD	Unidirectional
Ti	Titanium 15V-3Cr-3Al-3Sn alloy
St	SAE 304 stainless steel
RA	Release agent
GB	Grit-blasting
La	Laser irradiation
Turco	Alkaline etching with Turco® 5578 solution
HF/HNO_3	Acid etching with HF/HNO_3 solution
Ti-S-RA	Titanium straight release agent pretreated reinforcement
Ti-S-GB	Titanium straight grit-blasted reinforcement
Ti-S-Turco	Titanium straight wet-chemically pretreated reinforcement
Ti-S-La	Titanium straight laser pretreated reinforcement
Ti-A-Ra	Titanium arrowhead release agent pretreated reinforcement
Ti-A-La	Titanium arrowhead laser pretreated reinforcement
St-S-RA	Stainless steel straight release agent pretreated reinforcement
St-S-GB	Stainless steel straight grit-blasted reinforcement
$St-S-HF/HNO_3$	Stainless steel straight wet-chemically pretreated reinforcement
St-S-La	Stainless steel straight laser pretreated reinforcement
St-A-RA	Stainless steel arrowhead release agent pretreated reinforcement
St-A-La	Stainless steel arrowhead laser pretreated reinforcement

List of Figures

List of tables

1 Introduction

In the past few years, a huge effort has been made in the aeronautics industry regarding design and assembly of structural parts. The purpose is to get lighter structures, enhance performance and significantly reduce fuel consumption [4]. Hence, new material concepts offering weight savings and better performance are in high demand.

Composite systems have been known for many years, but only recently they have been used in full scale structural components [5]. The usage of such materials for aircraft structural applications is basically confined to fibres-reinforced polymers (CFRPs). With flexible and easy fabrication processes, CFRPs can achieve relevant characteristics such as high specific stiffness and strength, dimensional stability, corrosion resistance, electrical conductivity and even good fire/smoke performance [4, 5]. In civil aircraft, structural content of CFRP has already surpassed the 50% wt. barrier with the introduction of the AIRBUS' A350 XWB and the BOEING's 787 and the trend is for this value to further increase [6, 7].

Development of laminated composite systems for aircraft applications brought up new challenges. A major concern has been to establish effective assemblies between fibre-reinforced polymer (FRP/FRP) parts or FRP/metal parts. FRP present anisotropic properties whilst metals are generally isotropic. In addition, when joined together, problems like galvanic corrosion and mismatch between their coefficients of thermal expansion (CTE) may further weaken the joint.

Joining of composite materials is currently done by three methods: adhesive bonding, mechanical fastening or a combination of bonding and fastening [8]. Mechanical fastening represents the primary joining technique for composite structures due to the thorough knowledge and reliability achieved in the past for metallic structures. However, its application for joining of composite parts is not as simple as for metals [9, 10]. The introduction of fasteners which requires drilling of FRP parts results in stress concentrations around the holes due to the lack of plasticity and high notch-sensitivity exhibited by these materials. Other issues like low sealing performance, weight addition, increased costs and complex failure modes also represent major challenges for designing proper mechanically fastened joints for FRP structures [8-11].

Adhesive bonding emerged in the early 50's as a gentle, non-destructive joining technique for two different materials [12-14]. Notwithstanding many advances, problems like sudden joint failure, poor out-of-plane properties, need for relatively large bonding areas and lack of appropriative non-destructive testing (NDT) methods [8, 12, 14, 15] confines the certification of pure adhesively bonded joints only to non-critical aircraft structures. For safety considerations, mechanical fasteners are then added to overcome the unpredictability of bonded only joints by creating a secondary loading path [15]. But this implies destruction of fibres and further weight and costs increase due to the drilling process of thousands of holes for all joints in an aircraft structure.

Laminated composites are manufactured by stacking together a number of differently orientated plies, which enables them to provide in-plane reinforcement to the laminate structure

[16]. Since no fibres are positioned across the laminate (through its thickness), interlaminar failure becomes the most common failure mode for this material.

Progress in a variety of through-thickness reinforcement techniques for laminated composite structures have been made recently in an attempt to overcome the above mentioned issues. Stitching [17, 18], tufting [19, 20] and 3D-weaving [21], among others, emerged in the early 90's as effective z-reinforcement techniques, where important properties were improved. However, at that time, only one technique- z-pinning- was suitable for reinforcing uncured pre-preg laminates, often used in aeronautics structures [22]. This technique became very attractive since properties like delamination resistance, out-of-plane stiffness and joint strength were significantly enhanced. Nonetheless, such gains were only possible by sacrificing in-plane elastic/strength properties of the laminates itself [23, 24]. Besides that, even when partially automated, this was still a lengthy and costly process. Therefore, various novel technologies have been intensively investigated, including COMELD^{TM} [25], CMT [26] and HYPER [27]. The goal is to provide through-thickness reinforcement and establish an effective bond between CFRP/CFRP and CFRP/metal joints by combining adhesive bonding with the mechanical interlocking effect of the reinforcements without significant deterioration of in-plane properties.

A novel cost and time efficient joining technology has been developed by the Airbus Group, where a low thickness metallic sheet (stainless steel or titanium), with orthogonally bent reinforcements (pins), is placed between two CFRP adherents before or during the co-bonding process [28, 29]. This way, fibres are not cut but only deflected. Furthermore, the flexible manufacture process of these reinforcements, where spikes' contour stamping and bending is performed in an integrated tooling allows them to be designed depending on the actual loading case; typically straight for shear and with an arrowhead tip for supressing tensile or peel stresses [29].

These bent spikes work as damage arresting features by transferring ("bridging") loads between crack faces of the delamination and in this way, creating an additional load path. Different mechanisms by which these bent reinforcements resist to crack opening (mode I) and sliding (mode II) are involved, depending on the reinforcements' material and structural properties. This research focuses on characterizing those mechanisms on a single-pin level and ultimately establishing generic pull- and shear-out "bridging laws" that relate bridging forces of the reinforcements with the associate crack displacement.

Related technologies featuring carbon-fibre (CF) or titanium z-pins have successfully shown improvements on delamination toughness by resisting to crack opening and sliding [30-32]. Bridging mechanics of by which those pins provide closure forces were already thoroughly investigated. Under pull-out loading conditions, they were found to be dominated by debonding and frictional pull-out of the pins, simply described by a bi- or tri-linear bridging law [33-36]. More complex mechanisms were unveiled for shear loads involving debonding, substrate plasticization, lateral deformation of the pins and also friction, typically represented by a bi-linear force-displacement curve [31, 37]. A further mechanism of energy absorption is expected to be found for the technology under investigation, due to the elasto-plastic failure behaviour exhibited by these metallic spikes in contrast to the elastically dominated fracture of CF z-pins.

Contrary to traditional CF z-pins, the sheet bending technique discussed in this work, allows to benefit from the increased surface of the continuous pin carrying structure by pretreating it and in this way establishing further mechanical interlocking with the surrounding epoxy resin and adhesive on a milli-, micro- or even nano-scale level [38]. Mechanical, wet-chemical and physical surface pretreatments are therefore applied to the reinforcement elements. The aim was to roughly assess and compare the bridging behaviour of a surface featuring enhanced adhesion attributes or a larger macro-roughness scale resulting from a nano-structuring laser or a grit-blasting surface pretreatment, respectively.

Derived “bridging laws” are of utmost importance as they can be used for development of analytical or numerical solutions that describe/predict the delamination behaviour of more complex reinforced composite structures [32, 36, 39, 40]. When these experimental curves show a similar trend and a well-defined shape, a closed-form mathematical expression that relates bridging forces to crack displacement, can be set. For this purpose, various theoretical and numerical approaches have been successfully implemented. In an attempt to predict the delamination behaviour of laminates reinforced through this technology, an analytical approach based on elementary beam theory and fracture mechanics fundamentals was adapted from that developed for z-pinning [36].

2 Literature review on 3D-reinforcement techniques

In the following chapters, a detailed review on the most popular through-thickness reinforcement techniques for CFRP/metal and CFRP/CFRP joints is presented. A distinction between traditional (z-pinning and stitching and tufting) and novel (COMELD^{TM}, CMT, HYPER and RHEA) 3D-reinforcement techniques is made and the most relevant characteristics of each approach are pointed out.

2.1 Traditional 3D-reinforcement techniques for CFRP structures/joints

Stitching and tufting

Reinforcement of polymer matrix composites by means of stitching has come to light in the latest 90's due to the thorough insight on sewing fabrics achieved in the past for the textile industry [17]. Similar to the manufacture of textiles, stitching involves sewing a high tensile yarn such as carbon, glass or aramid (Kevlar) through the thickness of the laminate structure using a sewing machine. Aramid and glass are the preferred materials to be employed as the reinforcement yarn due to its greater flexibility.

In this process, prior to curing, a stack of plies is penetrated and locked together with the aid of a hollow needle and/or bobbin threads. The final stitched composite is usually then consolidated via resin film infusion or resin transfer molding. Fig. 1 illustrates the different styles of stitches employed for reinforcing composites. Among the most common styles of stitching, the modified lock stitch (Fig. 1 c)) is the most popular because it is the one that causes less fibre distortions and therefore less weakening of in-plane mechanical properties. However, even with this method, significant distortions of both in-plane fibres and fibres within the stitches are unavoidable as fibres are forced to bend to accommodate the stitches and stitches are crimped during laminate consolidation and compaction due to pressing of in-plane plies. These and other important flaws such as resin pockets, broken fibres and fibre kinking that are also introduced during stitching and represent the determinant factors that control the weakening on in-plane mechanical properties of stitched composites [18, 41].

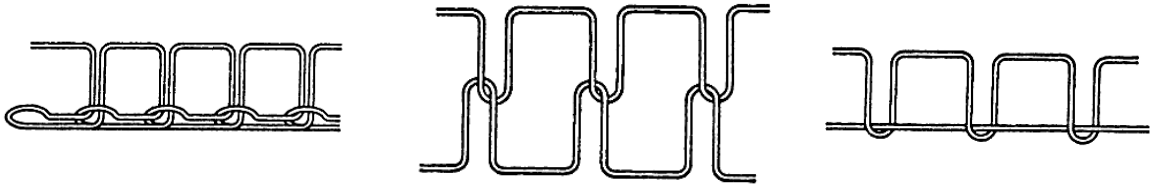

(a) chain stitch (b) lock stitch (c) modified lock stitch

Fig. 1- Typical stitch styles [41]

The fact that this technology uses a dual-threading system (upper and lower threads) to form the loops or knots makes it unrealistic for use in large and complex structural applications [17]. Moreover, the formation of locked stitches and the resulting tensioning of the threads results in crimping effects that can significantly weaken the in-plane mechanical properties of the stitched composite. For these reasons, a more advanced and reliable technology, similar to stitching, was developed- tufting.

Tufting is a single-thread sewing method in which the formation of loops is possible with a loose and tension-free insertion of a threaded needle that has less adversely effects on the material [17, 19]. The needle pushes the yarn inside the preform with the aid of an elastic foam

tool and its removal from the fabric is made along the opposite trajectory (Fig. 2a)); hence, only access to one side of the structure is required. Prior to resin infusion, the thread pathway allows the formation of a loose loop that remains in place relying on the friction between the yarn itself and the host fabric preform, as shown in Fig. 2 b). The actual reinforcement comes only after resin injection from the bonding between matrix and thread.

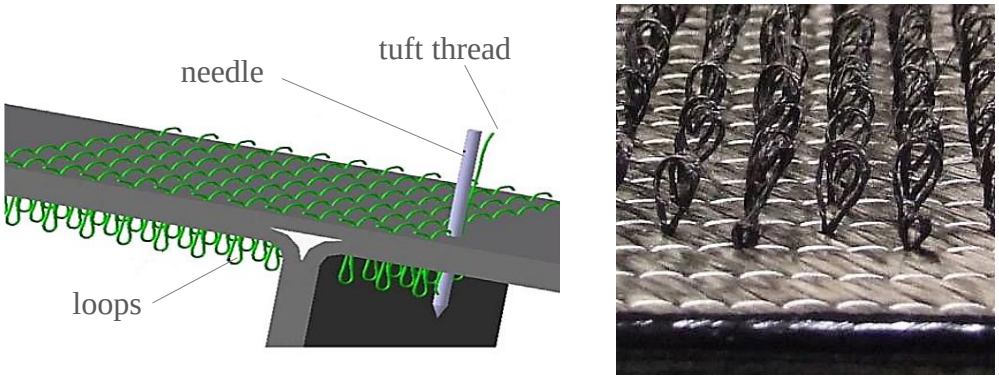

(a) schematic of the tufting process [20] (b) CF tufts in a non-crimp fabric [42]

Fig. 2- Tufting process.

According to Mouritz *et al.* [41], stitching reduces in-plane properties by up to 20%, while drop-downs with the tufting method stay below 10% [19]. On the other hand, "tufts" or "stitches" have shown to improve compression strength after low velocity and ballistic impacts of around 95% and 50%, respectively [43]. The presence of stitches on CFRP laminates was also found to improve the delamination resistance against crack propagation under both modes I and II of about 15 and 4 times, respectively [44, 45].

Stitched and tufted laminates have already being widely used in aircraft structures, such as fuselages, wing panels and blade-stiffened components [41, 46]. A serious limitation that still exist for these technologies, as well as for almost all classical through-thickness reinforcement techniques, has to do with the fact that they are only suitable for textile laminates made using dry fabric plies containing the reinforcement prior to resin infusion. There were already some attempts to reinforce pre-preg laminates, but the presence of uncured resin resulted in needle fouling that promotes even more severe damage to the in-plane fibres of the laminate [18]. This is a serious limitation, especially when it comes to aircraft structures since many highly-loaded components are manufactured by using pre-preg laminates [24]. At that time, only one technology was capable of reinforcing pre-preg laminates along its thickness - z-pinning.

Z-pinning

Z-pinning was first patented in the early 90's by the Aztex Corporation for reinforcing 2D laminates. Z-pins or z-fibres^{TM} are short rods made from a high strength/stiffness extruded wire material (titanium alloy, steel or fibrous carbon composite) that act as thin nails capable of locking the different laminate layers together by a combination of friction and adhesion. They are used in a diameter range of 0.15 to 1.0 mm and are present in laminates with a volume density in the range of 0.5 to 4%, which is equivalent to about 8 to 70 z-pins/cm^2 [24].

The most common manufacture process of z-pinned laminates is the UAZ® process (Ultrasonic Assisted Z-Fibre) also developed by Aztex Inc.. The process is well described in [47]. Consisting on inserting z-pins into an uncured pre-preg stack by using an ultrasonic tool, the process can be either automated, where one obtains better results in terms of accurate insertion and spacing between pins or can be operated manually by a trained operator, as schematically described in Fig. 3. When the process is fully automated, only access to one side

of the structure is required which represents another great advantage in relation to other classical techniques.

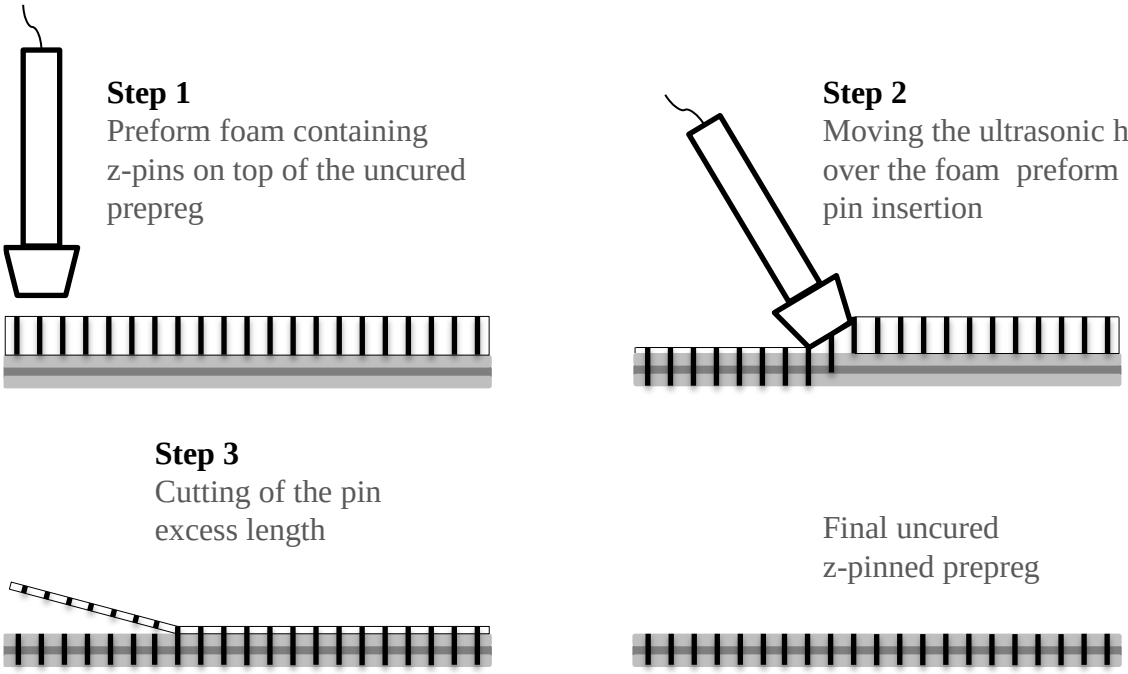

Fig. 3- Schematic of the UAZ® process.

Z-pinning is an effective and simple way to enhance delamination resistance, damage tolerance, out-of-plane stiffness and joint strenght of pre-preg laminates/joints. There are many published papers reporting z-pinning induced impacts on pre-preg laminates [23, 24, 47-49]. The bridging effects produced by z-pins (that will be described further bellow in chapter 3.1) can increase the delamination resistance of up to 160% and 100% under mode I and II loading conditions, respectively [49]. As a consequence, impact resistance is also increased and damage areas are of up to 64% smaller for z-pinned laminates. Residual compression-after-impact strength is also improved by z-pinning, with pinned laminates presenting around 45% higher residual strenght than their unpinned counterparts [50]. At last, important improvements in the z-properties of CFRPs such as tensile modulus can also be achieved by introducing z-pins into laminates, with the out-of-plane stiffness of z-reinforced laminates being increased by 50% or more with relative modest amount of pins (~ 4% by volume) [51].

Evidently, such gains on the through-thickness properties are only possible by sacrificing the in-plane mechanical properties. Although a general agreement on the causes for deterioration of such properties exists, the extent of damage induced to the in-plane properties due to the presence of z-pins, reported on the available papers, is not consistent. For example, Mourtiz *et al.* in [24] stated that the loss of stiffness and strength stays typically under 5-10%, while Steeves *et al.*[48] documented a 27-30% in-plane strength knock-down.

To be able to understand the benefits and damage induced to laminates caused by z-pinning, a full understanding of the microstructural changes is essential. It is believed that the harm induced to the in-plane elastic and strength properties is due to the microstructural damage caused by z-pinning, particularly fibre breakage and waviness as well as crimping, resin-rich zones and pin offset, as schematically depicted in Fig. 4. Swelling of the laminate and residual cure stresses are also believed to have a reciprocal impact on the in-plane properties of z-pin reinforced laminates [24, 47].

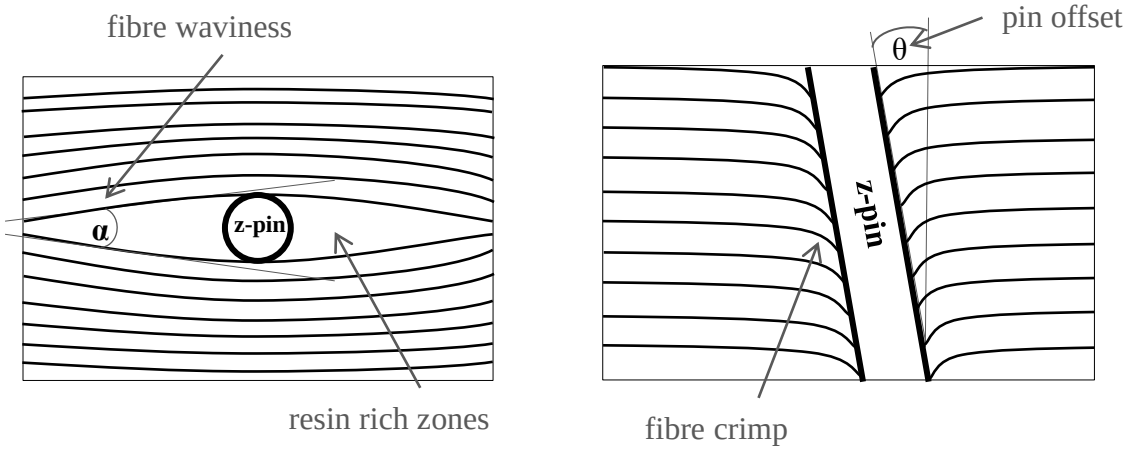

(a) fibre waviness and resin-rich zones (b) z-pin offset and fibre crimp

Fig. 4- Z-pinning induced microstructural damage.

2.2 Novel hybrid reinforcement technologies

COMELD™

COMELD™ (composite-to-metal) is a recent hybrid joining technology developed by the The Welding Institute (TWI) for manufacture of CFRP/metal joints, that aims to combine mechanical interlocking with adhesive bonding. The Surfi-sculpt® surface treatment, also patented by the TWI, provides the basis for the development of this hybrid joining method [25]. The main advantages of the Surfi-sculpt process in relation to other additive processes, such as direct metal deposition or additive layer manufacturing, is that it does not require complicated extra feed systems of wire or powder [52].

In this technique, prior to laying up the composite fabrics, an electron beam locally melts the surface of the metal substrate and displaces it to sculpt an array of protrusions and cavities. As shown in Fig. 5, translation of a focused beam over the metal surface induces the movement of material from bulk substrate to surface.

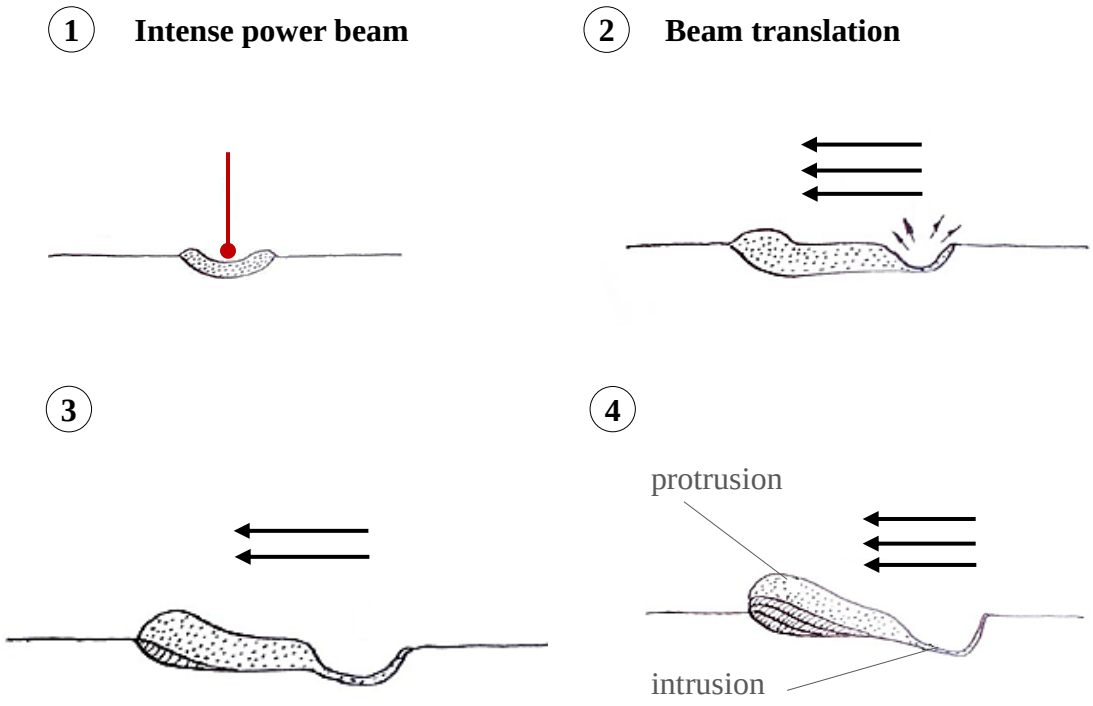

Fig. 5- Process steps involved in the generation of a simple Surfi-Sculpt® feature as in Fig. 6 a).

With appropriated parameter selection, this process can be employed to a wide range of materials including titanium and nickel alloys as well as stainless steels. The sculpted metal surface features or "proggles" are usually designed to lean in the opposite direction to the applied load [53] and can be shaped into different geometries and patterns, as shown in Fig. 6: single protrusions (Fig. 6 a)), wall features (Fig. 6 b)) and conical features (Fig. 6 c)) of up to 3.2 mm [52]. Bonding of the texturized metals to composite laminates forms the COMELD™ joint.

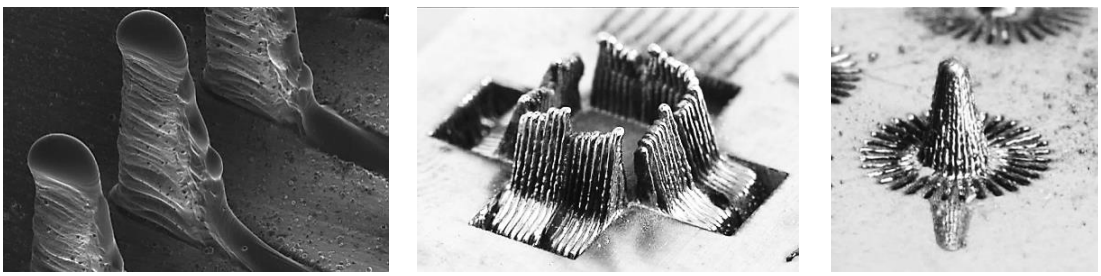

(a) single protrusion (b) integrated wall feature (c) conical shaped feature

Fig. 6- Tyical COMELD™ protrusions produced in titanium part [52].

Although being a relatively recent technology, investigations have already been carried out to assess the enhanced static performance of COMELD™ joints (titanium and stainless steel proogles) over pure adhesively bonded control joints [54, 55]. All studies revealed significantly greater load carrying capabilities as well as enhanced levels of energy absorption (up to 4 times higher), allowing a more progressive and damage tolerant failure of the joint.

Cold-Metal-Transfer (CMT)

Another similar technique was also recently developed by the Fronious Company. The Cold-Metal-Transfer (CMT), first developed for welding of thin aluminium sheets, is the basis for producing a high strength and damage tolerant joint between metals and composite parts [56]. CMT is a modified metal inert gas (MIG) welding process characterized by no spatter welding and low heat input, that results in small affected zones. This technology is similar to the afore mentioned COMELD^{TM} technique with the difference that instead of melting the metal substrate itself to shape the spikes, a filler wire with a certain height is melted onto the surface of the substrate with application of a high-current short circuit. These pieces of welding wire- the pins- remain attached to the metal acting as "mini-rivets". The process steps involved in the production of these reinforcements are schematically depicted in Fig. 7.

(a) Warmup phase (closed circuit)

(b) Deposition phase (open circuit)

(c) Sculpturing phase: rearward movement of the wire assists droplet detachment

Fig. 7- CMT welding process steps.

These "mini-rivets" or pins can present a variety of different shapes, as well as dimensions. The most common shapes are the cylindrical, the ball-head, and spiked pins illustrated in Fig. 8 a), b) and c), respectively. The spiked pins were designed as an alternative to the erstwhile cylinder and ball-head pins since, presumably, they would assist and ease the subsequent step of laying up the dry fibres. However, it seems that joints reinforced with this type of pins and with cylindrical ones have an equivalent performance in terms of mechanical behaviour [26].

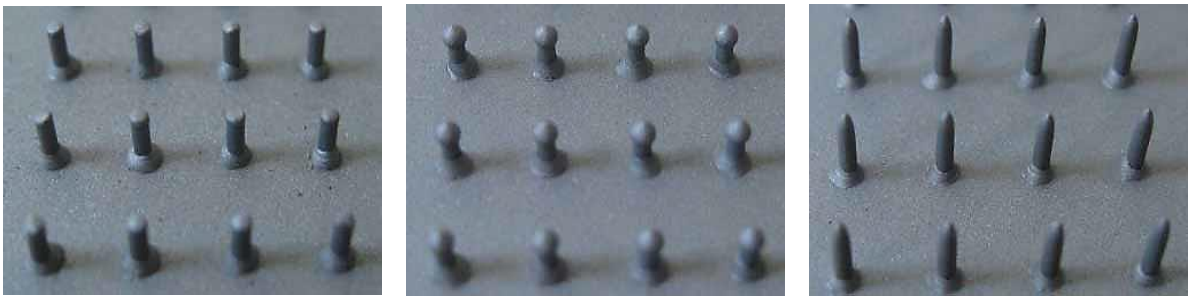

(a) cylindrical pins

(b) ball-head pins

(c) spiked pins

Fig. 8- Different pin shapes produced by the CMT technology [26].

Investigations performed so far to assess the enhanced performance of implementing this technology to a stainless steel-CFRP double-lap shear joint revealed that it is possible to obtain an increase in ultimate force of around 53%, 10 times more local strains and 30 times more energy absorption capacity when compared to conventional adhesively bonded joints. Furthermore, as opposed to what happened with pure adhesively bonded joints, which exhibit

a linear-elastic behaviour and fail catastrophically at the maximum force, the elasto-plastic behaviour detected in pinned reinforced joints, enables a progressive and detectable failure, with minor damages growing until a certain extent, that can be detected via visual inspection before losing structural integrity. Fig. 9 illustrates a failed CMT-reinforced double-lap shear joint with considerable composite damage and deformation of the pins.

Fig. 9- CMT-reinforced (cylinder pins) double-lap failed shear joint [26].

CMT is a fast and automated technique to introduce small metal reinforcements on composite structures with high reproducibility. However, subsequent stacking of dry laminate layers on top of the aligned pins is still a lengthy process that needs to be improved [26, 56].

HYPER

HYPER (Hybrid Penetrative Reinforcement) is a novel type of hybrid joining method also for reinforcement of CFRP/metal joints that is under investigation by the Airbus Group UK since 2007. Like the previously mentioned techniques, consists in producing a hybrid joint by co-curing together a composite and a metal part featuring an array of reinforcements (HYPINS) protruding from its surface. The difference in this case, is that HYPER uses Additive Layer Manufacturing (ALM) technology to enable a cost-effective manufacture of the complex features (Fig. 10). ALM is a new type of rapid prototyping technique where the parts (the pins in this case), given in a 3D CAD file, are built up layer by layer through a wire or powder feed system. The main advantages of this technology are that no material is wasted during manufacture and almost no constrains exist regarding the pins' geometry [57].

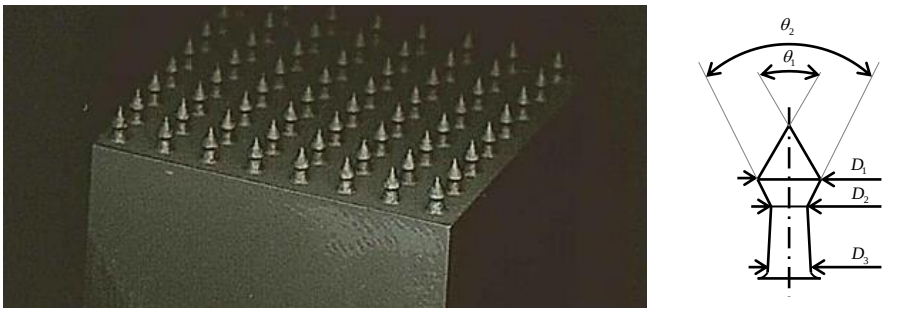

(a) Additively manufactured titanium HYPER pins [27] (b) detail of a HYPIN

Fig. 10- HYPER joining technology.

Although this technology is still at a low level of technology readiness level (TRL), investigations to date have shown impressive results over unpinned counterparts and other technologies. This is probably due to the unique complex pin shape that can only be produced through ALM technology [58] (Fig. 10 b)). Under shear loading, tests performed so far showed an increase of 300 % and 128 % in ultimate load when compared with bolted and bonded joints, respectively. The mean elongation at maximum load can be increased by over 400% and the energy absorption capacity can be more than 80 times higher, when HYPIN reinforcements are present [27]. Also, significant improvements of up to 6.5 times were encountered in terms of shear strength. In terms of pull-off strength and ultimate force, bolted and HYPER joints reveal an equivalent performance, with the failure mode being dependent upon the feature geometry

and array density. Progressive failure with visible damage of the joint ensures the main purpose of producing an extremely ductile and damage tolerant joint. Preliminary investigations also showed feasibility for implementation of a suitable ultrasonic NDT method for damage inspection [58], no corrosion issues, good fatigue performance [59] and that when subjected to lightning strikes, HYPINS do not incur in safety issues.

RHEA

RHEA (Redundant High Efficiency Assembly) is the former name assigned to the technology that is under investigation in the current work. This technology emerged in 2012 with the AIRBUS Operations GmbH, as a novel damage tolerant joining technique for CFRP structures with potential to improve performance and replace classical techniques for a more cost- and time-efficient technology [29, 57]. This project was primarily targeted for reinforcing fuselage and stringer/frames (Fig. 11 a)) CFRP structures of the Airbus A350 series.

As depicted in Fig. 11 b), this technique involves placing a low thickness metallic foil (0.2 or 0. 4 mm) made of a titanium alloy or stainless steel, with bent spiked features, between two CFRP adherents before or during the co-bonding process. Penetration of these pins into the laminate during the curing cycle is made by simply realigning the fibres, with almost no fibres being cut. These out-of-plane elements work as damage arresting features by providing an additional load path through a meso-scale mechanical interlocking, allowing a more progressive and predictable failure of the joint. Unlike the straight cylindrical shaped carbon-fibre (CF) pins used with z-pinning technology and others, this sheet bending technique allows to benefit from the increased surface of the continuous pin carrying structure by pretreating it and in this way establishing further mechanical interlocking with the surrounding epoxy resin and adhesive on a milli-, micro- or even nano-scale level. Perhaps even more important, is the additional level of energy absorption achieved with these pins through its plastic deformation in contrast with the dominating elastic fracture properties of CF z-pins.

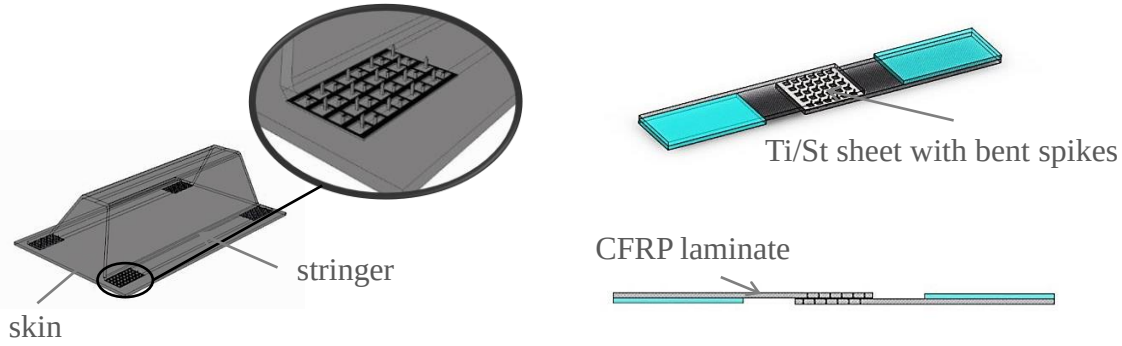

(a) skin-stringer RHEA joint (b) single-lap shear RHEA joint

Fig. 11- RHEA joints.

These metallic reinforcement elements were originally manufactured by means of laser-cutting (to shape the pins' contour) followed by orthogonal bending of the spikes. A new integrated tooling developed by Hölzel Stans- und Feinwerktechnik GmbH+Co. KG, where the spike's contour is stamped and then bent in a single tool enables huge cost and time savings and in this way, consideration for high-rate serial production. This flexible process allows the pins to be designed according to the actual loading case. A straight pin geometry (Fig. 12 a)) is usually considered for shear stress conditions whereas an undercut geometry (Fig. 12 b)) is normally preferred for out-of-plane or peel stresses. Stainless steel (SAE 304/1.4301) and Titanium 15-3 meta-stable β-alloy are the selected metals for manufacturing of the reinforcements since they offer good cold formability (necessary for the sheet metal forming

process), high strength, good galvanic corrosion resistance and relative good compatibility between CTE values of these and surrounding CFRP adherents.

(a) straight pins (b) arrowhead pins

Fig. 12- Typical RHEA reinforcement sheet structures [28, 57].

Recent studies revealed the potentiality of this sheet bending technique for enhancing the through-thickness properties of CFRP joints. When compared with co-bonded coupons, RHEA joints have shown improvements in terms of static strength, maximum joint deformation, damage tolerance and fatigue life. Shear strength of joints reinforced through this particular technique can be enhanced by up to 55% with more than the double of elongation at failure. Moreover, tests performed adopting this technology to the standard DCB and ENF geometries, revealed improvements in the fracture toughness of up to 100% for mode I and 75% for mode II loading conditions, respectively. The same kind of z-reinforced specimens exposed to hot/wet environment prior to testing, revealed further improvements of interfacial strength through the introduction of surface structured metallic reinforcements. The explanation for this fact is related with the relief of thermal residual post co-curing induced stresses through the expansion of the water saturated laminates. This gain in interfacial strength between metallic reinforcements and CFRP adherent is also a result from the surface pretreatment applied to the metallic carrying structure. Among others, a novel physical surface pretreatment based on laser irradiation stands out by modifying the metal's surface to a nano-range roughness level and in this way, creating an additional mechanism of mechanical interlocking. Early investigations carried out to assess the impact of these metallic z-reinforcements on the fatigue life of CFRP laminates, revealed improvements of over one order of magnitude with the spikes providing a crack arresting mechanism from certain crack delamination length onwards [28]. Yet, latter studies unveil that compared to a co-bonded reference, no significant increase of the fatigue performance is attained with this technology [60].

3 Theoretical background

3.1 Bridging of z-reinforcements in composite delamination

A long-standing problem with FRP laminates is their low delamination resistance. This is because fibre composites are manufactured by stacking together a number of different plies, orientated in a way that enables them to provide in-plane reinforcement to the laminate structure [39]. Since no fibres are positioned across the laminate, interlaminar weakness is an inherent problem of these structures. Hence, one of the most sought benefits when inserting z-reinforcements into laminates, is to enhance their delamination toughness.

Z-pinning and other sorts of z-reinforcements provide through-thickness strength to the composite laminate by transferring loads between fracture surfaces, as shown in Fig. 13. In general, these spikes or stitches are not effective at resisting the initiation or propagation of short delaminations [24]. However, for long delamination cracks, they are remarkably effective. This is most probably because they are placed only a few millimetres ahead from the potential site for crack onset. As the crack propagates reaching the several rows of reinforcements, these are subjected to axial tension. As a reaction, they provide closure bridging forces that act against further crack growth [22, 39]. When the distance (vertical for mode I and horizontal for mode II) between fracture faces is large enough, the pins are pulled out from the composite structure or sheared-off.

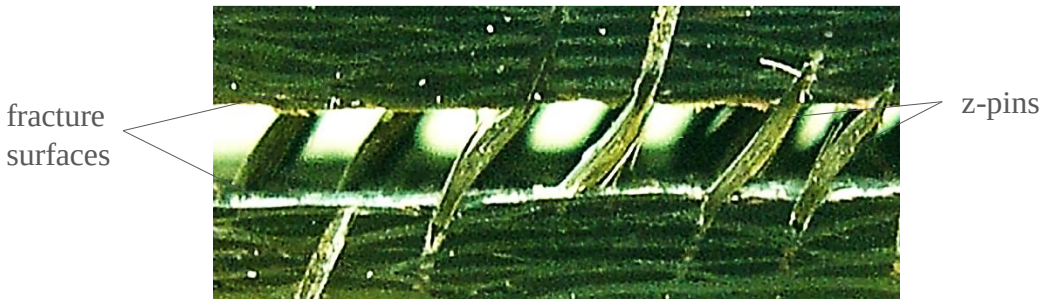

Fig. 13- Detail of z-pins' transfering loads between crack faces [24].

The above mentioned toughening mechanism for mode I and II loads is schematically illustrated in Fig. 14 and can be expressed by the force-displacement curve of a single pin/ rod/ tuft pull-/shear-out test.

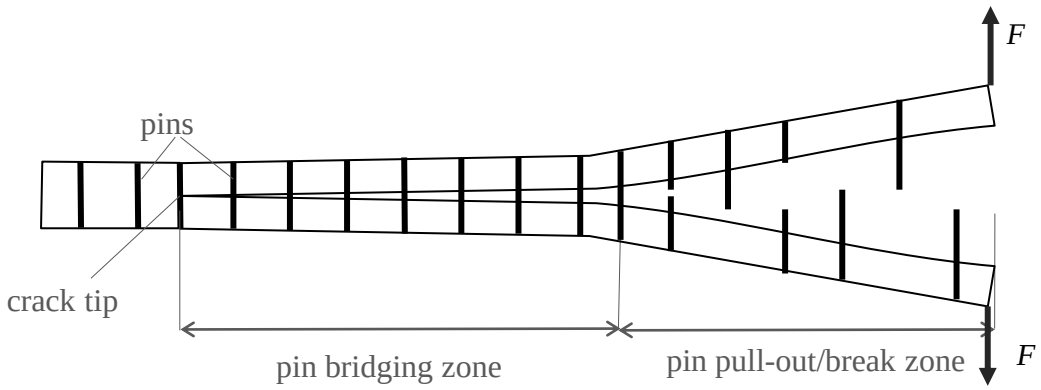

(a) mode I z-pinning toughening mechanism

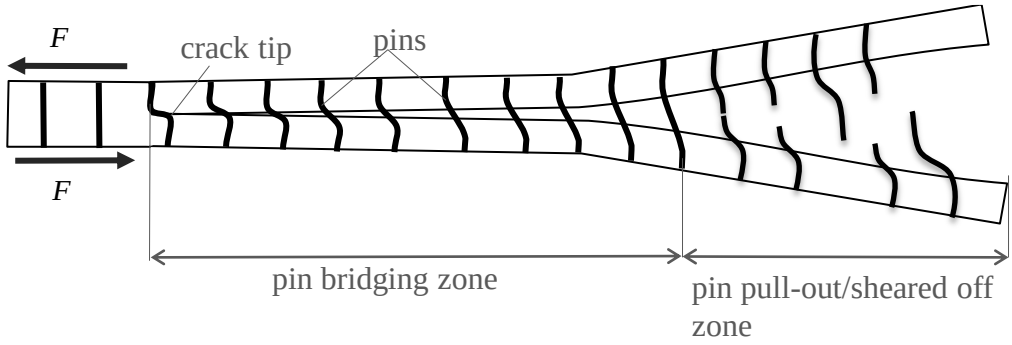

(b) mode II z-pinning toughening mechanism

Fig. 14- Bridging toughening mechanism in z-pinned composites.

The functional relationship between reinforcements' closure forces and associated crack displacement is named bridging law and is very important to characterize the effectiveness of the through-thickness technology. Bridging laws are obtained experimentally by pulling out a single reinforcement from within the laminate. When these experimental curves show a similar trend and a well-defined shape, a closed-form analytical expression that relates bridging forces to crack displacement can be set. This is extremely useful since it can be used for development of theoretical or numerical solutions that describe the delamination process of more complex reinforced composite structures.

In the following sections, pull/shear-out tests and derived bridging laws are presented for CF and titanium z-pins and tufts. The mechanisms by which z-pins or tufts provide bridging forces are quite similar and were already intensively investigated in [18, 30, 31, 33-35, 37, 39, 40, 42, 44, 45, 49, 61]. For mode I loading conditions, the mechanisms acting against crack growth are typically dominated by elastic deformation and friction between spike and substrate. Mode II shear tests revealed more complex mechanics involving elastic deformation, debonding, snubbing and pin shear-induced pull-out. Snubbing is the enhancement of friction for a pin that is deflected into the laminate near the fracture plane due to a pin/laminate contact pressure increase [37]. An additional level of energy absorption capacity is expected to be found for the technology discussed in the current work as for these reinforcements, in addition to elastic deformation, a significant plasticization should also be encountered, as opposed to what happened for CF pins/tufts.

3.1.1 CF and titanium z-pins bridging laws

Z-pin mode I bridging law

In order to determine the relationship between bridging forces and associated crack opening displacement of z-pinned laminates during mode I loading conditions, *i.e.* the z-pin bridging law, pull-out tests have been carried out by several researchers for CF z-pins [33, 34, 39, 49] and titanium rods [31, 37].

Dai *et al.* [33] developed a test set-up where an array of 3x3 CF z-pins is vertically inserted into the central area of two insulated pre-pregs before curing, as depicted in Fig. 15 a). More details on how this test was prepared can be found in [33]. The overall force applied on the specimens was divided by the number of z-pins to derive the average bridging force of a single pin. Tests for "small" and "big" CF z-pins (0.28 and 0.5 mm diameter, respectively) revealed curves with very similar patterns with two typical pull-out curves being distinguished, depending on the bonding quality between pin and surrounding laminate (Fig. 15 b)).

In this study, a noticeable debonding load-drop was detected during pull-out of "small" CF z-pins, suggesting a strongly bonded interface (solid curve in Fig. 15 b)). Thus, bridging law for such reinforcements can be defined by a tri-linear function defined by four parameters: maximum debonding force (P_d), maximum frictional force (P_f) and their corresponding displacements (δ_d) and (δ_f). Different mechanisms of energy absorption are involved in the distinct stages. In the first stage, the interface of the z-pin is considered to be completely bonded to the laminate with bridging forces causing elastic deformation only of the z-pin. As the pin stretches, interfacial shear stresses increase up to the interfacial shear strength of the interface between CF pin and surrounding laminate. At this point, debonding starts, represented by a sharp load drop and with curve characteristics entering the subsequent second linear stage. Closure forces at this stage result from pin elastic stretching (bonded part) and interfacial friction between the debonded part of the pin and surrounding laminate. Once the pin is fully debonded, pull-out from the laminate begins, with frictional pull-out as the only mechanism acting against crack opening. The derived functional analytic expression that relates bridging forces and z-pin displacement can be written as follows

$$P_s = \begin{cases} \dfrac{\delta}{\delta_d} P_d \quad (0 \le \delta \le \delta_d) \\ \dfrac{\delta_f - \delta}{\delta_f - \delta_d} P_d + \dfrac{\delta - \delta_d}{\delta_f - \delta_d} P_f \quad (\delta_d \le \delta \le \delta_f) \\ P_f + \dfrac{\delta_f - \delta}{h - \delta_f} P_f \quad (\delta_f \le \delta \le h) \end{cases} \tag{1.1}$$

where,

h is half-length of the z-pin;

P_d and P_f are the maximum debonding and frictional pull-out forces, respectively;

δ_d and δ_f are the corresponding displacements, respectively.

In the same investigation, it was shown that when "big" CF pins are used instead, a bi-linear law should be considered as no debonding spontaneous load-drop was detected (dotted curve in Fig. 15 b)). In this scenario, the interface between pins and laminate is assumed fully frictional due to weak bonding between spikes and neighbouring laminate. Under this scenario,

the bridging law is simplified to a bi-linear function determined by two parameters: maximum force P_f and corresponding displacement δ_f. The functional relationship between bridging force and associate opening displacement is, in this case, represented by the dotted curve of Fig. 15 b) and can then expressed by the following expression

$$P_s = \begin{cases} \dfrac{P_f}{\delta_f}\delta & \left(0 \le \delta \le \delta_f\right) \\ P_f - \dfrac{P_f}{h-\delta_f}\left(\delta - \delta_f\right) & \left(\delta_f \le \delta \le h\right) \end{cases} \tag{1.2}$$

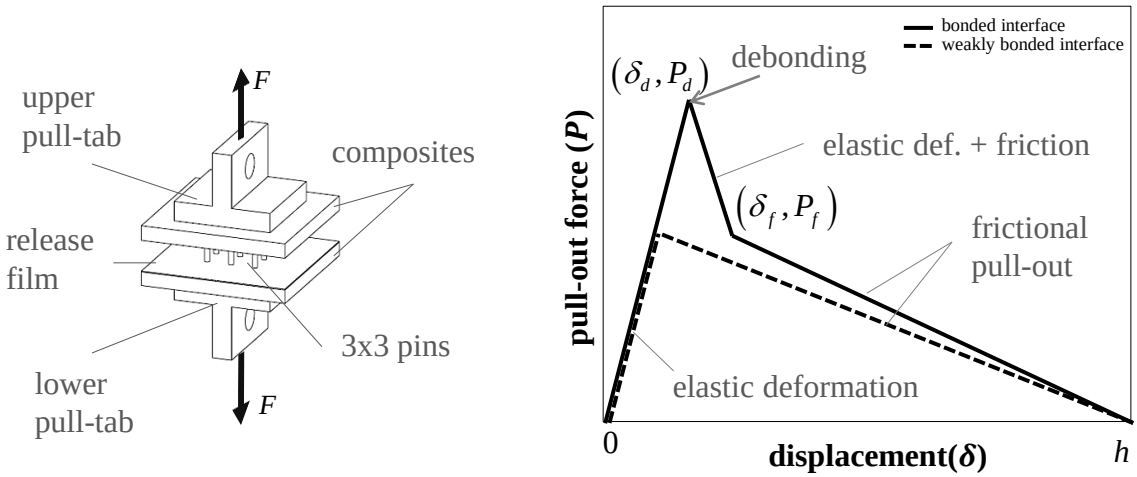

(a) experimental configuration for 3x3 z-pin mode I pull-out test

(b) mode I CF and titanium z-pin bridging laws

Fig. 15- Mode I CF and titanium z-pin pull-out.

A related study [31, 37], also conducted to explore the mechanics involved in the pull-out process of single CF and titanium rods inserted into a carbon/epoxy composite or polycarbonate (PC), have come to slightly different conclusions. PC was used to allow visual observation of the failure behaviour of the pins. According to this investigation, pull-out of z-pins from a cracked laminate can also be described by a bi- or tri-linear bridging law, as in Fig. 15 b). Yet, for Cartié *et al.* [31], other facts explain the observed differences between the two bridging laws (dotted and solid line from Fig. 15 b)). At the beginning of the first stage, the pin is also fully bonded to the surrounding laminate. However, elastic stretching of the pin at this stage is considered to be accompanied by gradual debonding, instead of an almost spontaneous adhesion failure at the peak force, followed by a rapid force drop, that was documented by Dai *et al.* [33]. The sudden sharp force drop documented for some specimens in this study (second stage of the solid bridging curve in Fig. 15 b)), is considered to happen when the necessary force for complete debonding is greater than the max. frictional force. A similar failure behaviour between the two reinforcements' materials was documented. The main pointed difference was that debonding of the titanium pins was not always linear as opposed to what happened for a CF pin. Yet, one would expect for the plastic capacity of the titanium spikes to provide a further mechanism of energy absorption. This did not happen most probably because adhesion between pin and surrounding laminate was not strong enough to withstand the necessary level of forces to provoke plasticization of those spikes, *i.e.* the adhesive interface fails even before bridging loads reach the material's yield strength.

In the above mentioned studies, no reference is made to applied surface pretreatments to the z-pins, with the purpose of improving adhesion. Grit blasting or laser pretreatments do not seem practical due to the geometry of the z-pins. However, a wet-chemical surface pretreatment could have been applied to such pins. This would probably enhance the bonding quality between rod and surrounding epoxy resin and eventually allow debonding forces to be high enough to provoke the plasticization of the titanium rod.

Z-pin mode II and mixed-mode I/II bridging laws

Mode II z-pin pull-out from laminated composites is a complicated process but is well explained in [30, 35]. During this process, the pin bends and then pulls out completely as illustrated in Fig. 16 b) or breaks-off as depicted in Fig. 17. As the shear force increases linearly, the crack faces move relatively to each other and the pin deforms along the crack growth direction. When a peak value of force (T_a) is reached at a (δ_a) displacement, pull-out of the pin is initiated and forces decreases gradually to zero. At this point, the relative displacement between crack faces is approximately equal to half-thickness (h) of the laminate and the pin has been completely pulled out from the laminate. This functional relationship between pull-out force (T) and associated shear displacement (2δ) can be described by the bi-linear bridging law depicted in Fig. 16 b) and expressed by equation (1.3)

$$T = \begin{cases} \dfrac{T_a}{\delta_a}\delta & (0 \le \delta \le \delta_a) \\ T_a - \dfrac{T_a}{h-\delta_a}(\delta - \delta_a) & (\delta_a \le \delta \le h) \end{cases} \tag{1.3}$$

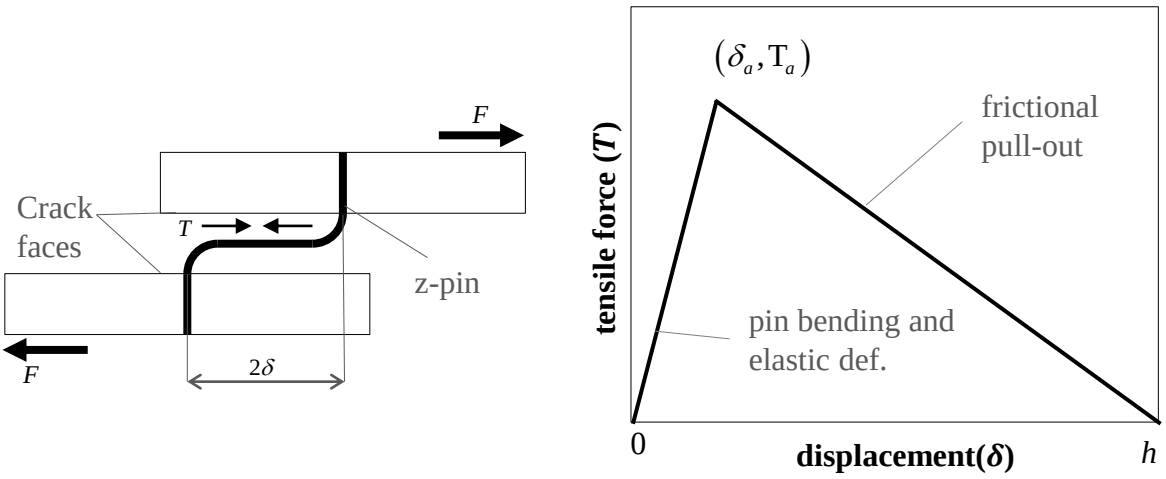

(a) experimental configuration and schematic for mode II CF z-pin pull-out process

(b) mode II CF z-pin pull-out bridging law

Fig. 16- Mode II CF z-pin pull-out.

It is important to point out that for the development of the present model, three assumptions were considered. Firstly, since the opening crack was very small and crack growth was predominantly mode II, pin bending effects were neglected [30]. Secondly, since ENF experiments performed in [31] suggested that the crack faces are kept open during delamination growth, frictional effects between crack surfaces were also not taken into account. At last, this model is valid only when the entire length of the pin is pulled-out from within the laminate, without its breakage. However, depending on the pin and host laminate material, z-pin breakage

may occur before complete pull-out. In this case, depending on whether the pin breaks before or after passing the peak force (T_a) , the curve shown in Fig. 17 a) or b) should be considered instead.

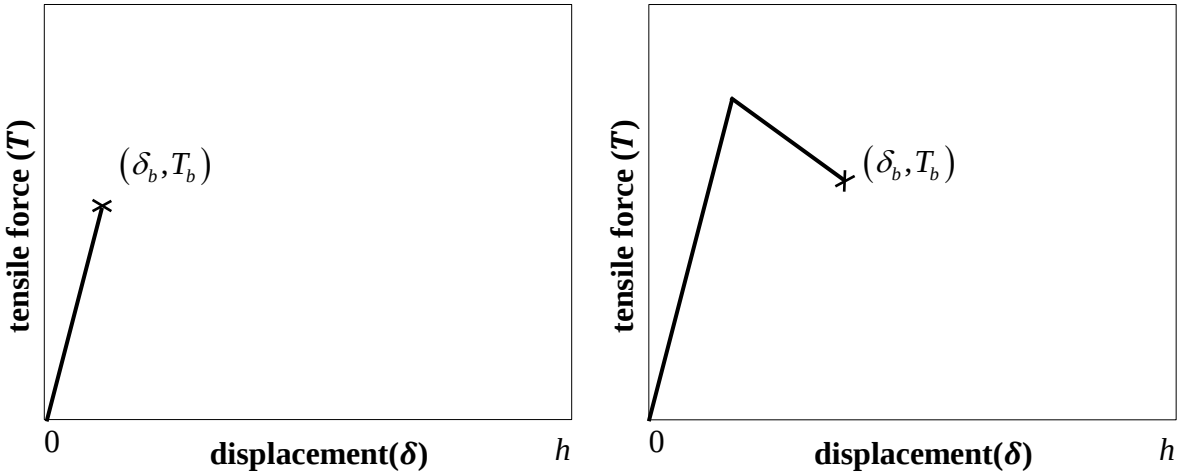

(a) mode II CF z-pin pull-out bridging law (pin breakage before peak load)

(b) mode II CF z-pin pull-out bridging law (pin breakage after peak load)

Fig. 17- Mode II CF z-pin pull-out with pin breakage.

Cartié *et al.* [31, 37] also conducted shear-out tests of titanium and CF rods inserted into UD composite laminates and PC. The test rig designed for this investigation is similar to that schematically depicted in Fig. 18 a). For applying pure mode II loading conditions, transverse opening had to be constrained by using a U-section block, as sketched in Fig. 18 a). Mixed-mode I/II tests, where specimens were free to rotate, *i.e.* with unconstrained crack opening, were also conducted. Depending on the reinforcement's material and whether opening is constrained or not, the pin pulls out completely or breaks in shear. Titanium rods endure all imposed loads until final pull-out with or without opening constrain. In contrast, CF pins pull-out completely only if opening displacement is allowed. Load-displacement curves of composite pins revealed a similar triangular shape to that described above in the study carried out by Yan *et al.* [30] and as depicted in Fig. 18 b) (dotted curve). If titanium rods are used instead, more complex energy absorbing mechanism are involved. Three main stages were distinguished as highlighted in Fig. 18 b) (solid curve): a pre-pull-out stage, a stable pull-out stage and a final unstable pull-out stage. As the pin bends at the pre-pull-out stage, shear displacement is limited by the elastic stiffness of the rod because the frictional zone has not yet reach its ends. At the consecutive stable pull-out stage, specimen's apparent stiffness decreases with both rod and substrate deforming plastically. Loss of mechanical stability occurs at the peak load with axial stresses at the rod falling and further pin deflection being limited. For larger displacements at the end of this stage, a more gradual force decrease was reported. An explanation for this fact, was found to be the enhancement of frictional forces due to an extended deflection of the pin against the fracture faces of the substrate.

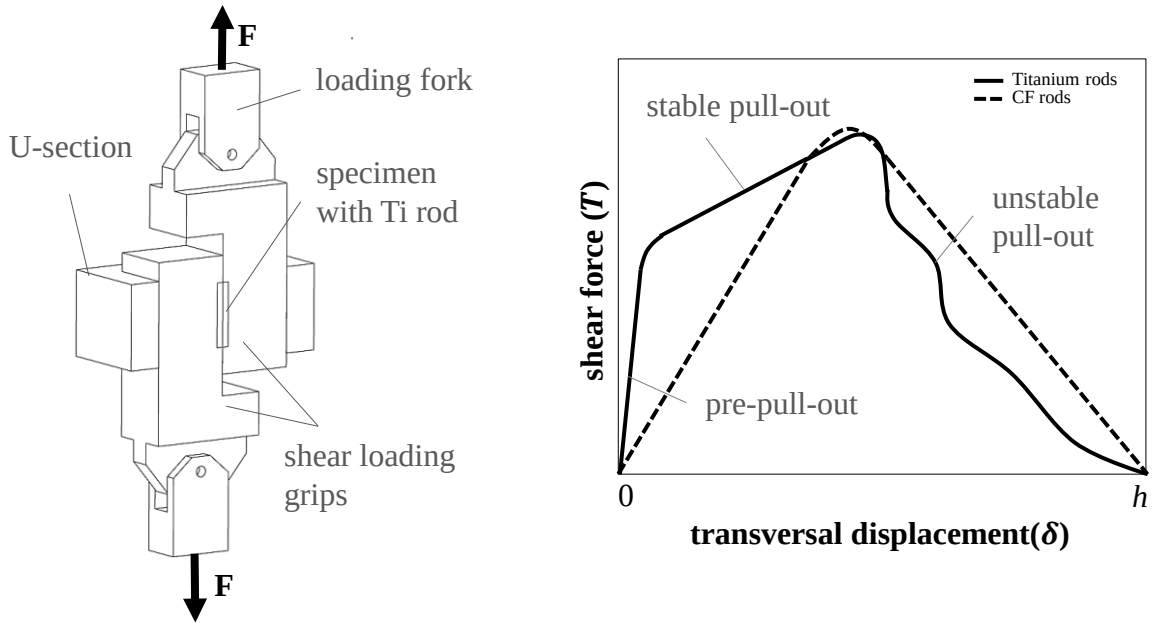

(a) experimental configuration for mode II and mixed-mode I/II CF and Ti rod shear-out process

(b) mixed-mode I/II Ti (solid line) and CF (dotted line) rods' bridging laws

Fig. 18- CF and Ti single-rod shear-out.

3.1.2 CF and glass tufts bridging laws

Tensile and shear tests were also performed in [42, 44, 45, 61] for determination of crack bridging laws of single tufts. It is very difficult to conduct a test in which pure mode II is applied due to crack opening mechanisms. Thus, Treiber *et al.* [42] suggested a mixed mode I/II testing procedure where most of the bridging forces are used for shear crack closure, but where also part of the energy is dissipated in acting against crack opening. In his investigation, glass and carbon tufts were introduced into dry preforms (non-crimp, twill woven and UD fabrics) to determine the relationship between bridging force of a single tuft and associated crack displacement under mode I and mixed-mode I/II loading conditions. An artificial pre-crack was created by placing an insulation release film in the middle plane of the dry preforms. More details on the tuft insertion process and on testing procedure can be found in [42].

Tuft mode I bridging law

The experimental configuration for mode I pull-out test is schematically illustrated in Fig. 19 a). Ten specimens of each tuft and composite material combination were tested until tuft failure. Identical tuft pull-out response was found for non-crimp and UD fabrics. For such specimens, a three-stage force-displacement curve was documented (Fig. 19 b)). In the first stage, a linear increase of bridging forces causes the fully bonded tuft and laminate to stretch elastically. Adhesion between thread and surrounding laminate starts to fail at the artificial crack interface, at loads close to 70 N and propagates along the tuft towards the outer surfaces of the laminate. At this point, curve characteristics enter a non-linear second stage where bridging forces increase at a lower rate, in a quadratic proportion with the opening displacement. As forces increase, resulting stresses reach the material's strength and the tuft fails spontaneously with broken threads being pulled-out under friction. Frictional pull-out of broken yarns was proved to contribute only by a small amount to the dissipated energy since most of the tufts failed at the crack interface. Similar pull-out failure behaviour was detected for tufted twill woven

fabrics with the difference that in this case, the tuft fails more progressively because yarn components of the tuft fail separately.

For comparison between different tufts' materials, three pull-out tests were also performed for specimens featuring non-crimp fabrics reinforced with single carbon and glass tufts. Lower stiffness and circumference of the glass yarns resulted in a 40% energy absorption decrease and lower levels of max. bridging forces when compared to the carbon counterparts (Fig. 19 b)).

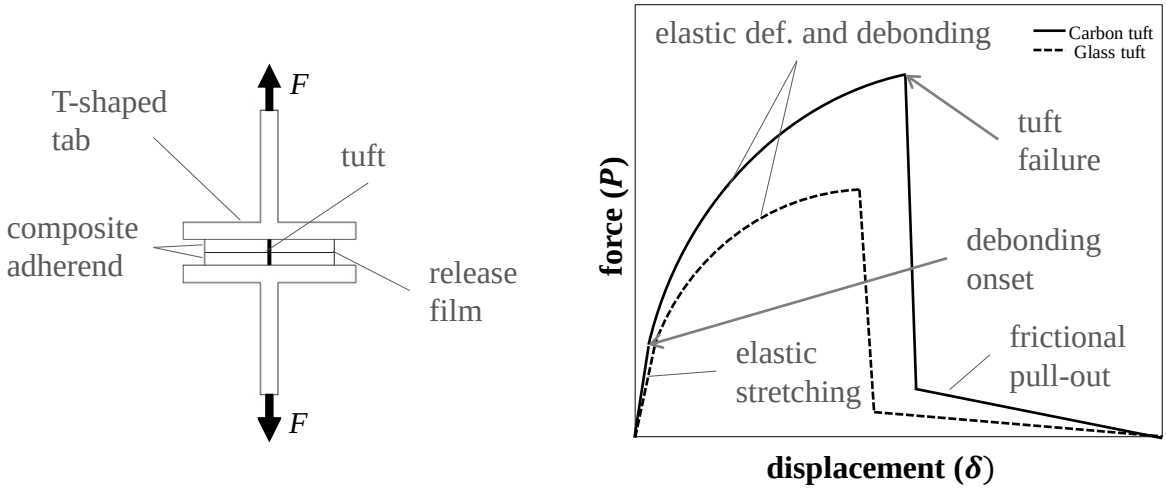

(a) experimental configuration for single-tuft mode I pull-out test

(b) mode I CF (solid line) and glass (dotted line) single-tuft pull-out bridging laws

Fig. 19- Mode I single-tuft pull-out.

Tuft mixed-mode I/II bridging law

Testing setup for mixed-mode I/II tuft pull-out is schematically depicted in Fig. 20 a). Two opposite pull arms were designed to allow rotation, thus enabling crack opening. When separating shear and opening effects into two plots, a completely different tuft failure behaviour was detected. For mode I loading conditions, the surrounding composite has little influence on the pull-out failure behaviour. In contrast, single-tufts response to mixed-mode I/II loads highly depends on the mechanical properties and geometrical aspects of the laminate.

As depicted in Fig. 20 b), an initial linear elastic stage was documented. However, as the crack propagates, bridging forces of the single tufts changes significantly depending on the surrounding laminate and main fibres' alignment. For UD or non-crimp tufted fabrics, if the fibres at the laminate's crack interface are aligned with the applied load, the tuft debonds and ploughs into the resin pocket formed to accommodate the tuft during its insertion. Maximum bridging forces are low, but can be sustained for large shear displacements until resulting stresses in the tuft are higher than its strength. If load is applied orthogonally to the fibres' direction, higher bridging forces can be achieved, but shear displacement is constrained by the 90° aligned fibres leading to reduced levels of dissipated energy. Final tuft shear failure normally follows an "S" shaped curve, with splitting and debonding of the tuft threads.

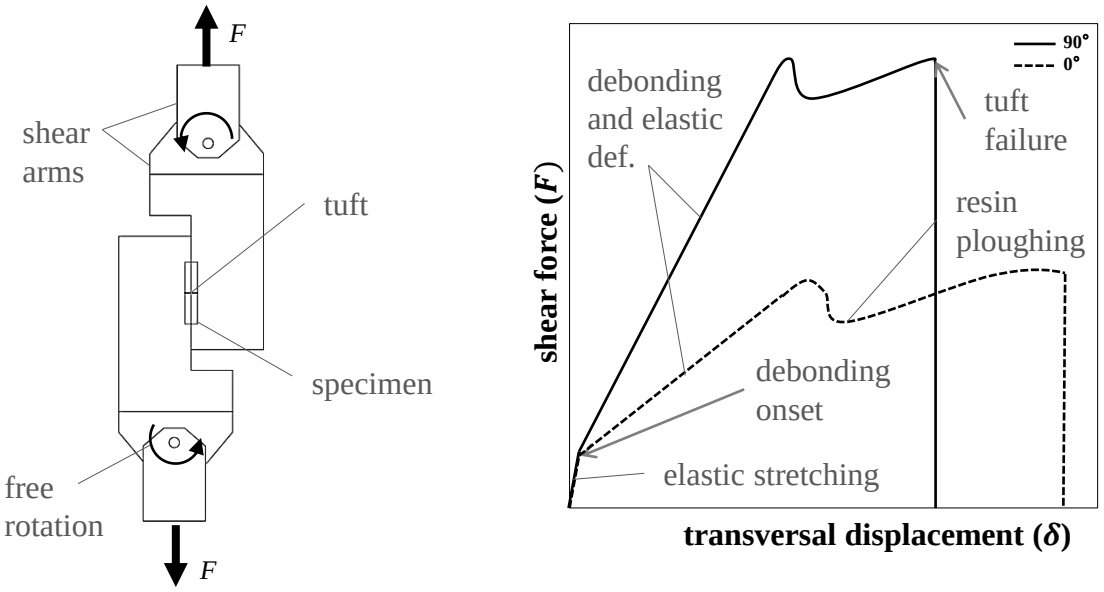

(a) experimental configuration for mixed-mode I/II single-tuft pull-out test

(b) mixed-mode I/II single-tuft bridging laws with applied load against (solid line) and aligned (dotted line) with fibres' orientation at the crack face

Fig. 20- Mixed-mode I/II single-tuft pull-out.

3.1.3 Analytical solution for mode I delamination prediction of z-pinned laminates

To investigate the delamination behaviour and evaluate the efficiency of z-pins introduced into a composite laminate, several analytical approaches were developed [32, 36, 40]. The aim is to predict the failure behaviour of complex z-reinforced structures through elementary beam theory and fracture mechanics fundamentals by using the results obtained from the simple single-pin pull-out experiments.

For its model, Liu *et al.* [36] considered an adapted reinforced DCB specimen which is the standard geometry to study mode I delamination toughness of composite laminates. As depicted in Fig. 21, an initial pre-crack divides the DCB specimen into two beams reinforced by c columns and r rows of z-pins. Due to symmetry, only one beam may be considered for this model.

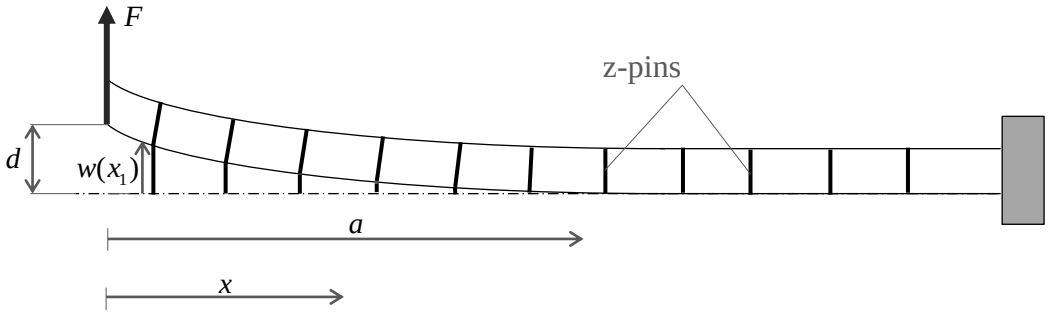

Fig. 21- Schematic of a DCB test for z-pinned composite laminate.

Fracture energy method is used as the delamination criterion [62]. The strain energy release rate at the crack front $(x = a)$ is calculated as follows

$$G_I = \frac{1}{b}\frac{\partial U}{\partial a} \tag{2.1}$$

where b is the width of the beam and U is the total strain energy of the deformed beam, which according to Castigliano's theorem equals to

$$U = \int_0^a \frac{M(x)^2}{2EI} dx \tag{2.2}$$

in which EI is the flexural rigidity of the laminated beam and M is the bending moment. By combining equations (2.1) and (2.2), one obtains

$$G_I = \frac{1}{2EIb}\frac{\partial}{\partial a}\left[\int_0^a M(x)^2 dx\right] \tag{2.3}$$

If this calculated value of strain energy release rate is greater than the critical intrinsic toughness of the laminated beam- G_{IC} - the crack propagates.

Before the crack has passed the first column of pins $(a \le x_1)$, the bending moment M is simply given by

$$M(x) = Fx \tag{2.4}$$

Thus, equation (2.3) can be easily solved. Yet, after the crack has passed the first column of pins $(a > x_1)$, the bending moment M is dependent not only on the applied force F, but also on the total closure forces P_i provided by the active z-pins. It can be expressed as follows

$$M(x) = Fx - \sum_{i=1}^{c} P_i (x - x_i) \tag{2.5}$$

Where P_i and x_i are the bridging force and the location of the ith column of z-pins, respectively. The bridging force P_s provided by each pin of ith column is assumed to be equal. Thus, it is possible to describe the total bridging force of the ith column of pins as follows

$$P_i = rP_s \tag{2.6}$$

The bridging force P_s of a single z-pin is estimated through the previously mentioned bridging law (chapter 3.1.1), which is a function of the flexural displacement w of the beam. From the generalized beam theory, the equation that expresses the deflection w of the beam, at the location x, is

$$\frac{\partial^2 w(x)}{\partial x} = \frac{M(x)}{EI} \tag{2.7}$$

Since the bending moment M is dependent on the bridging force P_s, it is mathematically difficult to obtain a closed-form solution of equation (2.7). Thus, an iteration method is considered instead. Two possibilities exist for application of the iterative calculation. The way how these iteration methods are implemented is well explained in [36] and [32]. The basic idea consists in either adding the applied displacement d or the force F, step by step, until the energy release rate is higher than the fracture toughness of the unreinforced laminated beam. At this point, the crack length a is added, step by step instead, with no further displacement d or force F. The key point of this method is to neglect any bridging force of the z-pins when the crack front has just passed their location. This way, it is possible to calculate the deflection of the beam right at the pin location. Then, by introducing the obtained displacement of the

beam into the bridging law (chapter 3.1.1), the actual bridging force P_s of the pin can be recalculated. Following this iteration method and considering the appropriate boundary conditions in equation (2.7), a simple expression for the displacement of the ith column of z-pins can be obtained as follows

$$w(x_i) = \frac{1}{EI}\left[\frac{Fx_i^3}{6} - \sum_{m=1}^{i-1}\frac{P_m}{6}\left(x_i - x_m\right)^3 + Cx_i + EId\right] \tag{2.8}$$

in which,

$$F = \frac{1}{2a^3}\left[\sum_{m=1}^{c} P_m\left(a - x_m\right)^2\left(2a + x_m\right) + 6EId\right] \tag{2.9}$$

$$C = -\frac{1}{2}Fa^2 + \sum_{m=1}^{c}\frac{1}{2}P_m\left(a - x_m\right)^2 \tag{2.10}$$

Verification of the suggested bridging laws is then made by plotting the obtained values of force F at each displacement d. The analytical results should be similar to the experimental data obtained during the DCB test when the appropriated material properties and geometrical parameters are considered.

4 Specimen conceptualization: materials, geometry and configuration

The main goal of this study was to evaluate the mechanical interactions between a single reinforcing spike and surrounding polymer. The ideal specimen would therefore, consist of a single pin penetrating into a CFRP laminate. However, due to manufacture constraints, this was not feasible. Hence, a specimen concept consisting on an interleaving metallic sheet with several pins penetrating into a CFRP laminate was designed as depicted in Fig. 22. Since the metallic reinforcement sheet incorporates a continuous pin carrying structure, a thin release film covering this structure was employed, to ensure only spikes to mechanically and chemically interact with the surrounding resin. In this chapter, a detailed presentation of materials, dimensions and architecture of the parts that compose the specimen is provided.

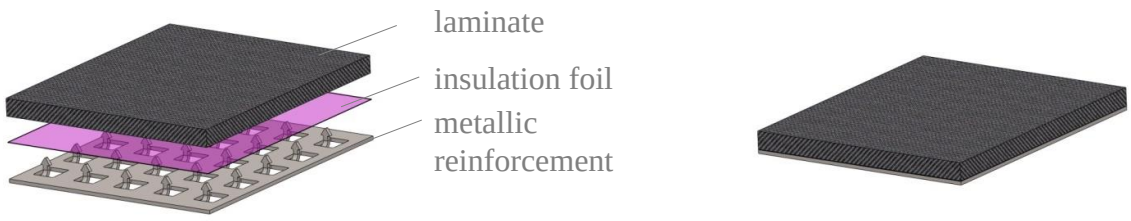

(a) stacking of a 5x5 multi-pin specimen before curing (b) specimen after curing

Fig. 22- Specimen concept.

4.1 Material selection

CFRP pre-preg adherent

Investigations carried out in the framework of this project considered a pre-preg CFRP adherent as the composite material to be reinforced. This material was selected by the Airbus Group since it is similar to that utilised in primary structural parts of the A350 series [57].

The CFRP investigated in this work was the Hexply® M21/35%/198/T800S medium grade unidirectional pre-preg, provided by the Hexcel Corporation. 35% represents the resin weight percentage, 198 the fibre areal weight (g/m^2) and T800S is the type of fibre that forms this pre-preg material. Each uncured layer of this material has a nominal thickness of 0.193 mm. The T800S carbon-fibres of high tensile strength are pre-impregnated in an M21 epoxy resin system that-besides displaying an excellent toughness, in particular at high energy impacts-presents high residual compression strength after impact, good hot-wet properties (of up to 150°C) and low exothermic behaviour.

Metallic z-reinforcements

As shown in chapter 3, the main goal of placing reinforcement inserts between two composite laminates is to enhance crack propagation resistance and improve damage tolerance through a crack bridging mechanism. Thus, it is intuitive that the best candidates to provide a high joint performance are the high-strength metals and its alloys. However, as it will be referred in the following chapters, a sheet metal forming or stamping process was selected for manufacture of

the metallic reinforcement inserts [28, 29, 57]. This way, it is also essential that the selected metals can be cold worked, in order to bend the inserts. Metals and its alloys that do not offer cold workability would just fracture during the bending process [57]. It is also important to choose a material featuring a CTE similar to that of the CFRP adherent since otherwise, post-curing induced thermal stresses could compromise the structural integrity of the joint. Furthermore, it is also critical to choose a metal that do not bring up corrosion issues when in contact with the CFRP adherents. For these reasons, aluminium and its alloys are not suitable. Considering all these issues, two materials were selected: stainless steel (SAE 304/1.4301) and the cold-workable meta-stable β-alloy Ti-15-3 (AMS 4914A), that will be characterized further bellow and have the following properties presented in Table 1.

Table 1- Mechanical properties of selected reinforcements' materials [63-65].

	SAE 304/1.4301	**Ti 15-3**
Density (g/cm^3)	8	4.78
Yield strength (MPa)	200	1050
Ultimate tensile strength (MPa)	500-700	1060
Young's modulus (GPa)	200	103-111
Elongation at break (%)	45	11
CTE (µm/(m°C)). linear 250 °C	17.8	9.2

Stainless steel (SAE 304/1.4301)

SAE 304 is an austenitic stainless steel that contains chromium (17-20%) and nickel (8-11%) as the main non-iron constituents. It also contains around 0.08% of carbon, 2% of manganese, 1% of silicon, 0.045% of phosphorus, and 0.03% of sulphur. It is not very electrically or thermally conductive, and is non-magnetic. It has a higher corrosion resistance than regular, promoted by its nickel content and relative good strength. This type of stainless steel is widely used essentially because of its good cold workability and weldability [63]. In relation to the titanium counterpart, this material represents a more cost-efficient benchmark but features higher values of CTE, Young's modulus and obviously higher density.

Ti 15-3 alloy (AMS 4914A, aerospace specification)

Ti-15-3 is a shortened designation for the Ti-15V-3Cr-3Al-3Sn alloy that contains 15% of vanadium, 3% of chromium, 3% of aluminium and 3% of tin. The commonly used α+β-alloys (e.g. Ti-2.5 and Ti-6Al-4V alloys) lack of cold formability and therefore they were replaced by the meta-stable β-alloy Ti-15-3 (AMS 4914A) from Timet Inc. to manufacture the metallic reinforcements of 0.4mm thickness [65]. Besides their cold workability and aptitude to be heat treated that is essential for the manufacture process designated for this technology, Ti β-alloys are known for their higher yield strength and toughness when compared to the classical α+β alloys. Furthermore, this alloy displays relatively high levels of elongations, strength and a low Young's modulus [64, 65]. Even though this is an expensive alloy, its main properties like high specific strength, excellent corrosion resistance, good formability and compatibility between CTE values of this alloy and the CFRP adherents make it a very promising material to be employed as the reinforcement element.

4.2 Geometry and configuration

CFRP adherent

Since this investigation was primarily targeted for fuselage structures, a quasi-isotropic laminate layup [+45°/-45°/0°/90°/0°]s was selected for all specimens, which represents the commonly used stacking sequence of fuselages and skin/stringer structures [57]. Each layer of this pre-preg material has a nominal thickness of 0.193 mm, forming in this way uncured laminates of approximately 1.93 mm thickness (ten layers per specimen).

Metallic z-reinforcement

The first reinforcement prototypes were made from a 0.2 and 0.4 mm thick metallic sheet. However, the high pressure values required for the curing cycle (up to 7 bar) for pins' penetration and laminate consolidation, irreversibly damaged the thin 0.2 mm thick spikes [29]. Hence, only 0.4 mm thick metallic reinforcement sheets were considered for the current investigation.

Several arrays can be considered for the reinforcing sheets by varying pin spacing, number of pins per window, design of the carrying sheet structure and pin head shape. In related investigations for CF multi-pin pull-out test [33, 34], spike array selection ranges from a 3x3 up to 7x7 layout. In the present work, an array of 5x5 pins was selected to stick close to the areal density of 1.2% investigated in previous researches [38, 60]. Each sheet to be applied in one specimen was 25 mm wide and 30 mm length. These dimensions were determined by constrains related to the manufacturing process of the 5x5 pins reinforcement sheets.

Pin tip shapes can be designed depending on the actual loading case. Straight pins (Fig. 23 a) and c)) can be used for shear and tensile loading conditions and spikes featuring an undercut geometry (Fig. 23 b) and d)) are mainly used to supress bending stresses. Both shapes were considered in this study to distinguish between the impact of the surface pretreatment and geometry induced effect on the specimens' failure behaviour. The two distinct geometries considered for the metallic reinforcements are detailed in Fig. 23.

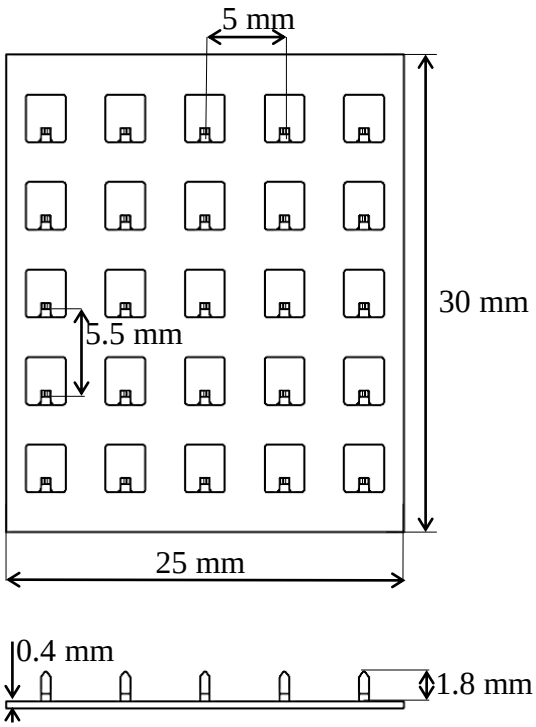

(a) reinforcement sheet with bent straight pins

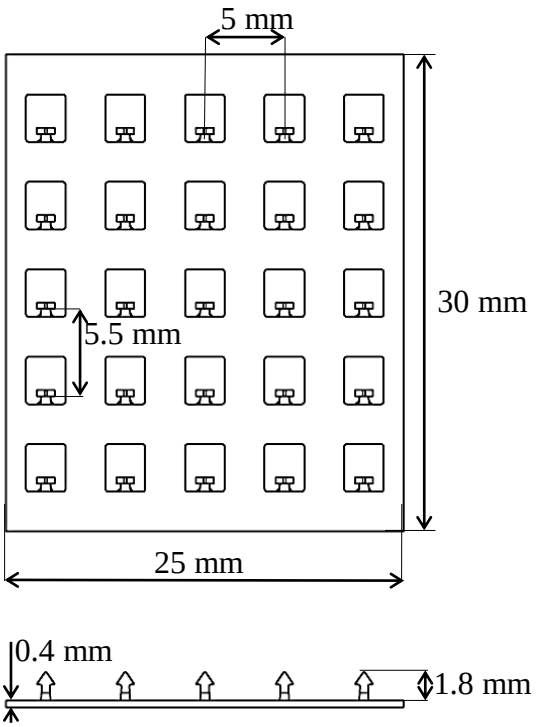

(b) reinforcement sheet with bent arrowhead pins

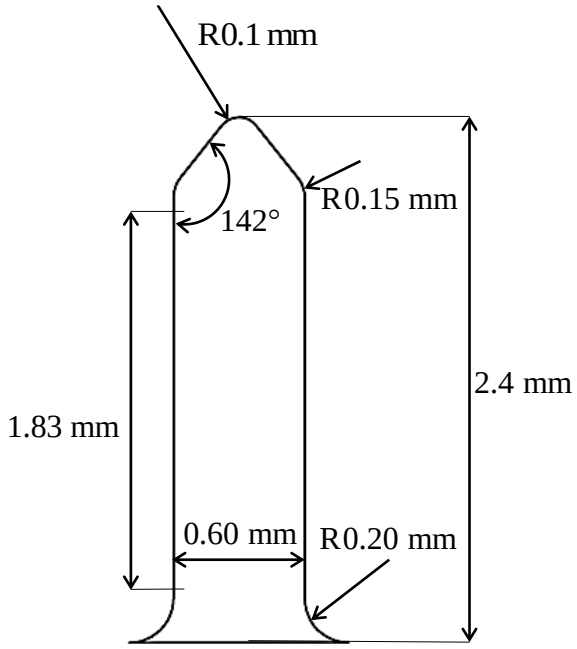

(c) detail and dimensions of a straight pin

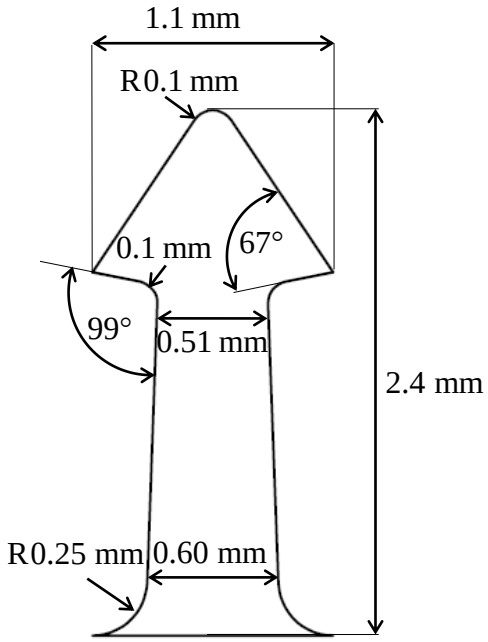

(d) detail and dimensions of an arrowhead pin

Fig. 23- Geometry and dimensions of the reinforcement sheets considered for this investigation.

Pull-out tabs

According to the testing procedures for both mode I and mixed-mode I/II pull-out tests, some kind of pull-out loading tabs should have been glued to the upper and lower surfaces of the specimen, to ensure no undesirable damage was induced to the specimens during testing. Pull-

out tabs made from current steel were therefore, manufactured to allow simple mounting and an even stress distribution along the specimen during testing. The final configuration of the specimen is depicted in Fig. 24.

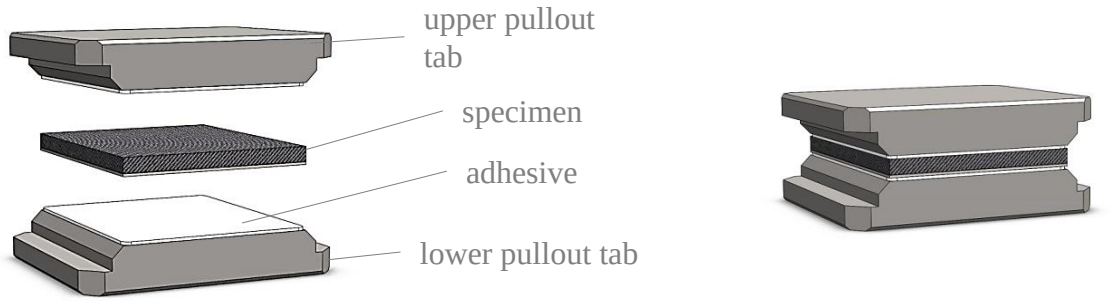

(a) specimen set-up before bonding (b) specimen equipped with pull-out tabs

Fig. 24- Final configuration of the specimen

5 Manufacturing

5.1 Manufacturing of the reinforcement sheets

Steel and titanium sheets were initially laser cut into strips containing seven reinforcement arrays separated by rips that were used to clamp and drive the strips during bending operation- Fig. 25. In a subsequent step, the reinforcement spikes were bent in the out-of-plane direction with the aid of a tooling developed by Hölzel Stanz- und Feinwerktechnik GmbH+Co. KG. With this tooling it is also possible to stamp the metal sheets instead of laser-cutting them, allowing this way huge cost savings since production of the reinforcement sheets (laser-cutting and stamping) is performed in one single integrated tool.

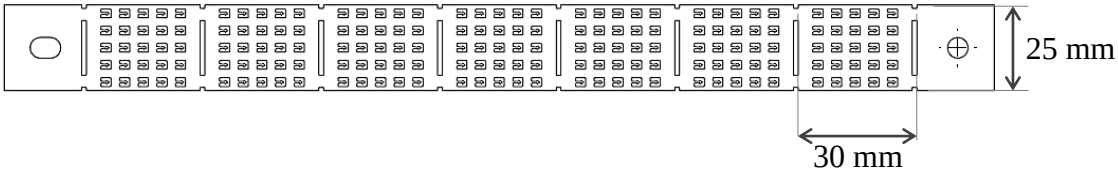

Fig. 25- reinforcement strips before bending process.

When bending the metallic sheets, there are two main aspects to be considered to ensure a crack free bent process: rolling direction of the metallic sheets and the ratio between spikes' bending radius and sheet thickness [63-66]. First of all, it is crucial to bend the spikes in the parallel direction of the previous rolling process in order to take the maximum advantage of the metal´s robustness. Secondly, a minimum value for the ratio between bending radius and sheet thickness should be respected to produce a crack free reinforcement. The literature typically recommends a value for the bending radius of around half of the thickness of steel bent parts [63]. Due to the more difficult formability of titanium alloys, higher minimum bending radius are recommended for this material, of up to four times its thickness [64-66].

Cutting of the reinforcement edges (that were necessary to clamp and drive the reinforcement strips during bending operation) was the last step also performed through laser-cut technology. Final metallic reinforcement sheets are shown in Fig. 26.

(a) reinforcement sheet featuring straight pins (b) reinforcement sheet featuring arrowhead pins

Fig. 26- Final reinforcement sheets.

5.2 Surface pretreatment

The surface pretreatment is one of the most important steps in terms of adhesion properties between metal and polymer [67]. In the present work, a co-bonding process where pins are introduced into the laminate during the curing cycle, was selected for manufacturing of the specimens. Thus, the metal substrate surface is the only one to be pretreated since before curing cycle, the adherent (CFRP pre-preg) is in an uncured state.

Lately, many surface pretreatment techniques have been investigated and developed to replace traditional grit blasting techniques for an improved long-term durable adhesion quality of titanium and stainless steel parts [13, 68, 69]. These investigations showed that in some cases, wet-chemical processes like alkaline etching and anodizing can enhance the bonding performance by creating a surface morphology in the range of a nano-scale. However, major drawbacks such as the use of environmental unfriendly chemicals and unique bath setups for different metals are stimulating the development of new techniques [67]. Dry laser pretreatments processes have also proved to be successful in modifying the surface of titanium on a nano-range, resulting in an enhanced bonding quality due to an increased surface. Rechner *et al.* [70] showed that with high laser intensity, contamination removal and chemical activation of the metal surface is also possible [60].

The current investigation was not focused on the chemical interactions between metallic spikes and surrounding polymer. However, a comparison between the impact of the most popular surface pretreatment techniques including wet-chemical processes, grit blasting and laser irradiation on the bridging mechanisms of the reinforcing spikes was a sought issue during this investigation. Therefore, mechanical, wet-chemical and physical surface pretreatments were applied to titanium and stainless steel reinforcement sheets, as described in [71]. An additional set of specimens was release agent treated by applying one coat of Marbocote TRE45ECO before the autoclave co-curing cycle to distinguish between the impact of mechanical interlocking and adhesion on the energy absorbing mechanisms of the reinforcing spikes.

Typical Ti 15-3 and SAE 304 morphologies post surface pretreatment are illustrated in Fig. 27 to contrast between distinct roughness scales created on such surfaces after the above mentioned surface treatments. Al_2O_3 pretreatment (Fig. 27 a) and d)) creates the largest morphology scale (> 0.1 µm), whereas a physically laser based treatment (Fig. 27 c) and f)) creates the smallest scale of < 100nm. Alkaline or acid etched surfaces (Fig. 27 b) and e)) commonly display a microscale morphology (0.1- 1 µm) as demonstrated in [2, 67, 68]. In the coming chapters, a brief description on how such surface pretreatments were applied is made.

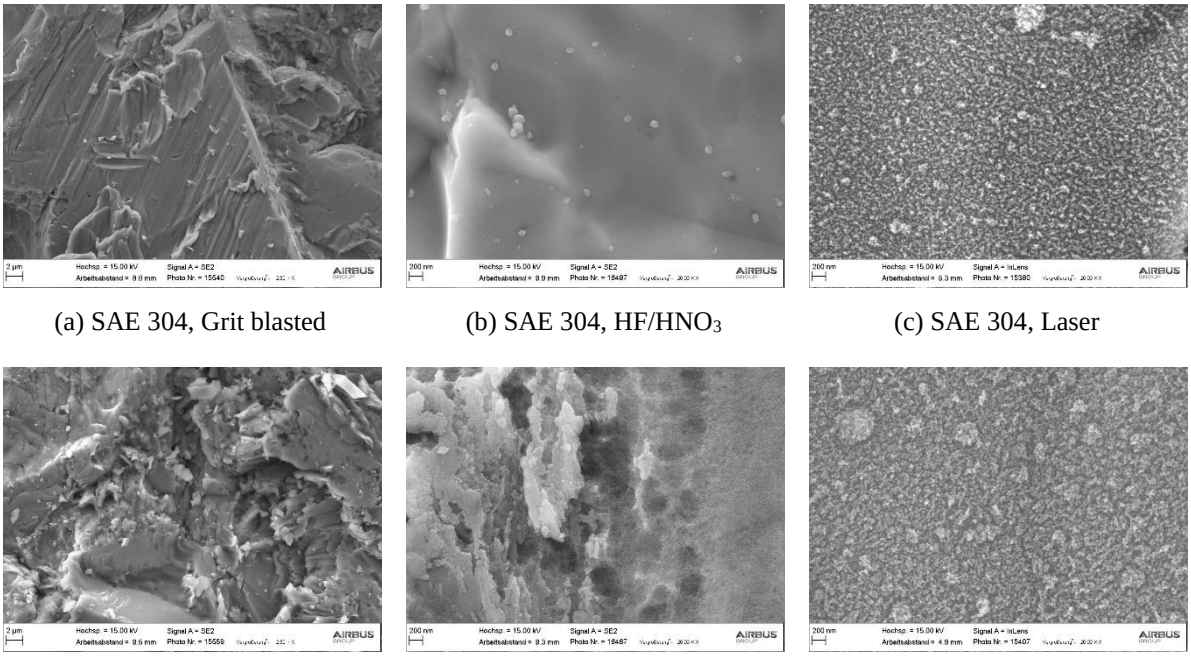

(a) SAE 304, Grit blasted (b) SAE 304, HF/HNO_3 (c) SAE 304, Laser

(d) Ti 15-3, Grit blasted (e) Ti15-3, Turco 5578® (f) Ti 15-3, Laser

Fig. 27- High magnification detail of typical surface morphologies resulting from the investigated surface pretreatments [2, 60].

Mechanical surface pretreatment: grit blasting

Abrasive grit-blasting with Al_2O_3 (grain size 250-500 µm and 7 bar of blasting pressure) was applied to the metallic reinforcements of a set of specimens in order to roughen and increase the active surface. Subsequently, mechanically pretreated surface sheets were plasma-treated to chemically convert manufacturing-related contaminations (such as silicon residues from the pressure plate) into compounds that are harmless to the bonding process [71].

Titanium grit blasted reinforcements typically display fragmented and brittle fracture surfaces (Fig. 27 d)) post mechanical surface treatment due to its lower ductility and tenacity in comparison with the austenitic SAE 304 stainless steel (Fig. 27 a)) [60, 71].

Wet-chemical surface pretreatment: alkaline and acid etching

Prior to the wet-chemical surface pretreatment, all metallic sheet surfaces were cleaned with the alkaline cleaner P3 Almeco 18.30 g/l (Henkel AG & Co. KGaA) at 60°C±3 for 15 min. Etched titanium reinforcement sheets were then placed in a Turco® 5578 g/l (Henkel AG & Co. KGaA) bath whereas etched steel reinforcement sheets were exposed to a 40/52% HF/HNO_3 solution. Acid etching process was performed for 5 min at RT, while the alkaline process was made under 95°C for 5 min.

Pickling environment of the acid etching treatment precludes the formation of an oxide layer on SAE 304 surfaces due to its chromium dissolving attributes which results in a smooth or flat surface [72]. For the Ti 15-3 wet-chemically treated surfaces, a more robust oxide layer of 20-30 nm thickness was documented.

Physical surface pretreatments: laser irradiation

The physical surface pretreatment was applied by a short pulse laser system Powerline E25 (Rofin-Sinar Laser GmbH, Nd: YVO_4) with a wavelength of 1064 nm. The set of parameters used for laser nano-structuring of both beta-alloy Ti-15-3 and SAE 304 surfaces was developed by Kurtovic [67] for Ti-6Al-4V (Table 2).

Table 2- Laser parameters considered for laser irradiation pretreatment [67]

Velocity (mm/s)	800
Working distance (mm)	207
Current (A)	43
Average Power (W)	25
Frequency (kHz)	10
Repetition rate (--)	1

For the best possible quality of the laser treatment, reinforcements' surfaces to be physically pretreated were focused horizontally in a 90 degrees angle to the normal incidence in ambient atmosphere. As shown in Fig. 28 a), reinforcement spikes are bent orthogonally and so, the metallic sheet was subsequently inclined to a maximum contingence angle of 60 degrees, limited by geometrical constrains. Yet, Juergens *et al.* [38] showed that irradiation angles that are greater than 45 degrees are sufficient to create an oxide nano-structure layer that is thicker than 150 nm. Fig. 28 b) shows a picture of a titanium straight reinforcement sheet whose pins are being pretreated by means of laser irradiation.

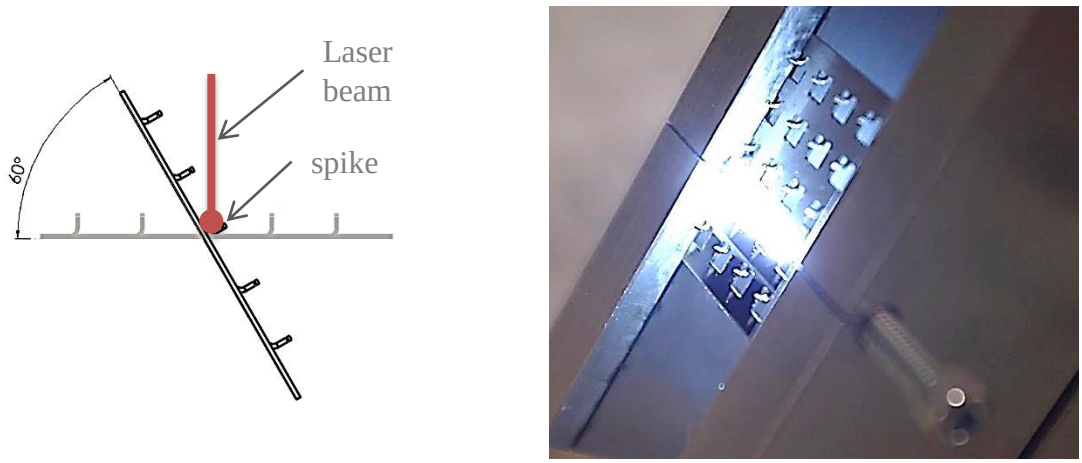

(a) schematic of sheet positioning for laser treatment [38] (b) laser irradiation of Ti pins

Fig. 28- Laser irradiation pretreatment.

5.3 Preparation for the autoclave

Stacking of pre-preg plies

As it was referred before, a quasi-isotropic layup [+45°/-45°/0°/90°/0°]s was the selected stacking sequence for manufacture of the specimens' adherents. As shown in Fig. 29, ten pre-preg layers of 305 mm wide, 205 mm length and 0.193 mm thickness were carefully stacked together forming a laminate of approximately 1.93 mm thickness that was used to produce a set of 20 specimens.

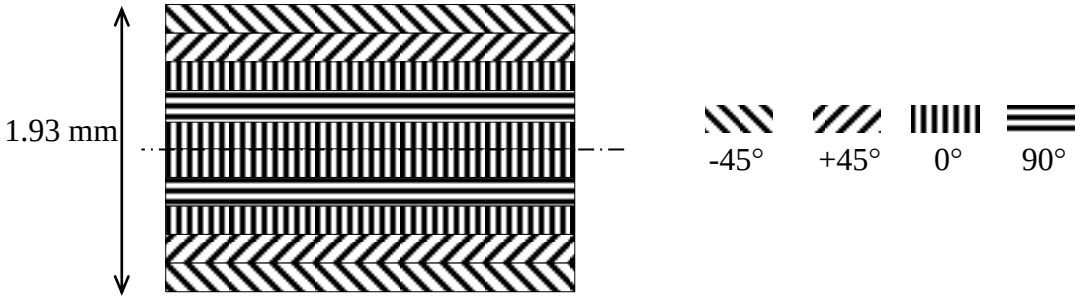

Fig. 29- CFRP laminate stacking sequence.

Debulking and cutting of the pre-preg plate

After stacking the pre-preg layers, the assembled pre-preg plate was placed under vacuum for 15 minutes at room temperature. This ensured an even consolidation and that air was removed off the laminate, before final curing.

After debulking, the M21 pre-preg material had to be cut to the right dimensions with the aid of a sharp cutter. Since the pre-preg plate was going to be placed on top of the metallic reinforcement sheets and inside a base plate, it was necessary to ensure the pre-preg plate to cover the entire area occupied by the reinforcements and that was smaller than the inner area of the base plate. The last demand is imposed due to the greater value of CTE exhibited by the pre-preg plate in comparison to the aluminium base plate. In fact, in the first manufacturing trials, a pre-preg plate of approximately the same dimensions as the inner area of the base plate was used. What happened was that, when the cured CFRP laminate was removed from inside

the autoclave, it bent during cooling damaging the specimens and hindering its removal from inside the plate. For this reason and to avoid edge effects, the 305 x 205 mm pre-preg layers used for stacking were already planned for having an additional 10 mm length and width to be discarded before the autoclave cycle (Fig. 30).

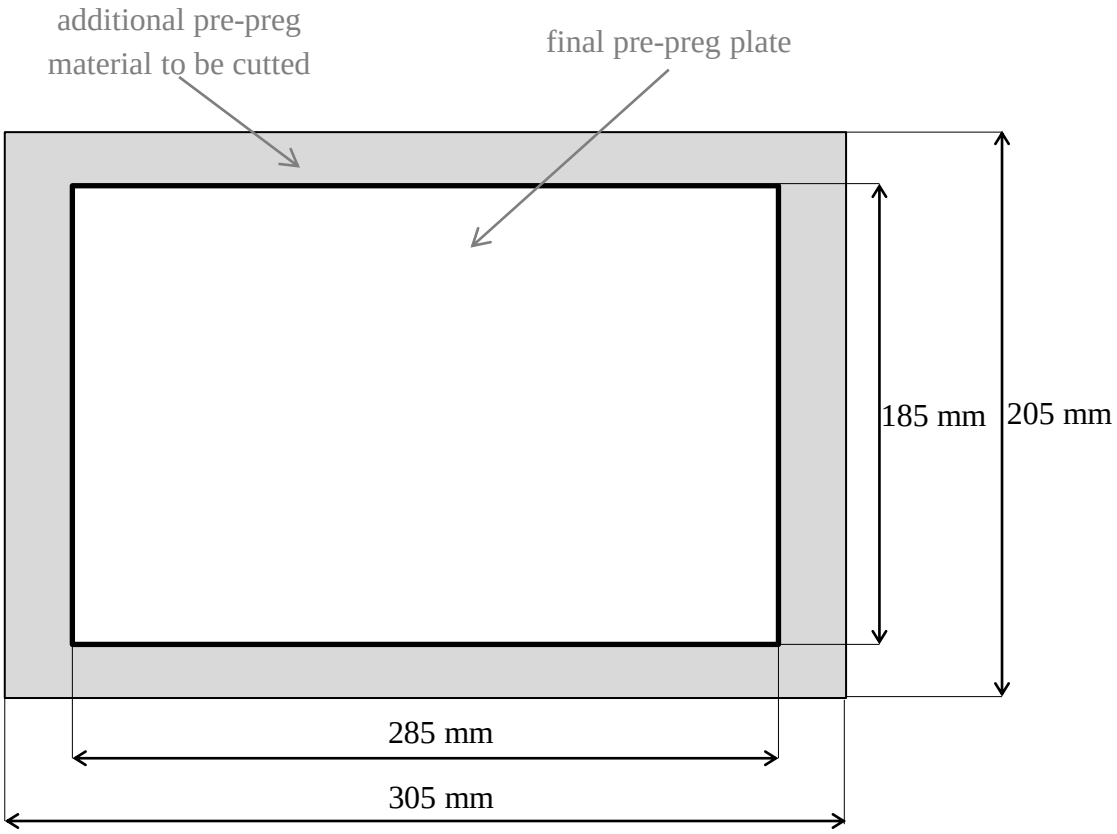

Fig. 30- Schematic of the pre-preg plate with additional material for subsequent steps.

Cleaning and surface preparation of metallic parts

All aid tools that were employed inside the autoclave were cleaned with isopropanol to ensure contamination-free surfaces for the curing cycle. The metallic toolings were furthermore release agent treated by applying two coats of Marbocote TRE45ECO (one and half an hour before starting the curing cycle), to prevent bonding to the laminate.

5.4 Autoclave

Finally, autoclave set-up was prepared according to the following steps and as shown in Fig. 31:

i. Positioning of the aluminium base plate (1) on top and in the center of the autoclave base table;

ii. The bottom mesh (2) was then placed on the bottom of the base plate (1) with its edges facing the inner bottom edges of the base plate. Several small pieces of high-temperature resistant tape were applied on the bottom mesh (2) and on the base plate (1) to prevent moving of the meshes when laying the metallic reinforcements into the respective windows of the meshes;

iii. In a consecutive step, the metallic reinforcement sheets (3) were placed inside the windows of the bottom mesh (2), by ensuring a correct positioning *i.e.*, that any reinforcement sheet was laying underneath the bottom mesh;

iv. Then, a sheet of insulation foil (4; A 6200 from Richard Aircraft) was applied and fixed onto the upper mesh (5) with several pieces of high-temperature resistant tape. Besides preventing sticking of the two meshes (2 and 5) to each other, the insulation foil also avoided bonding of the pins' carrying structure to the laminate;

v. The upper mesh (5) was then placed onto the bottom mesh (2). After ensuring that both meshes were aligned *i.e.*, that the edges of the reinforcements were facing the edges of the respective windows of both meshes, the upper mesh (5) was glued to the base plate (1). Some pressure had to be manually applied on the upper mesh to ensure spikes to penetrate the foil prior to temperature increase;

vi. The wet pre-preg plate (6) was then laid on top of the upper mesh (5) with its edges at a distance of approximately 10 mm from the inner faces of the base plate (1);

vii. A sheet of Wela polyamide peel ply fabric (T0098) was laid on top of the uncured laminate for excess epoxy resin absorption and to provide a rough finished surface, requiring minimal preparation in future bonding;

viii. A 300 x 200mm flexible silicone pressure plate (7) was then placed on top of the peel fabric covering the entire uncured laminate. This plate ensured an evenly distributed pressure over the entire prepreg and thus, an orthogonal penetration of the pins into the laminate during curing cycle;

ix. A sheet of vapour permeable release film (A 6200 from Richard Aircraft) was also laid on top of the pressure plate; the whole set-up was held in place by gluing several pieces of high-temperature resistant tape on its sides;

x. Two thick layers of a fleece breather fabric (model RC 300-10E polyester breather) covered the entire set-up to avoid the vacuum bag from being perforated by the sharp edges of the tooling during curing cycle;

xi. The set-up was finally sealed by gluing a vacuum film (Vac Pak HS-81719) to the base table of the autoclave using a double layer of Tacky Tape®.

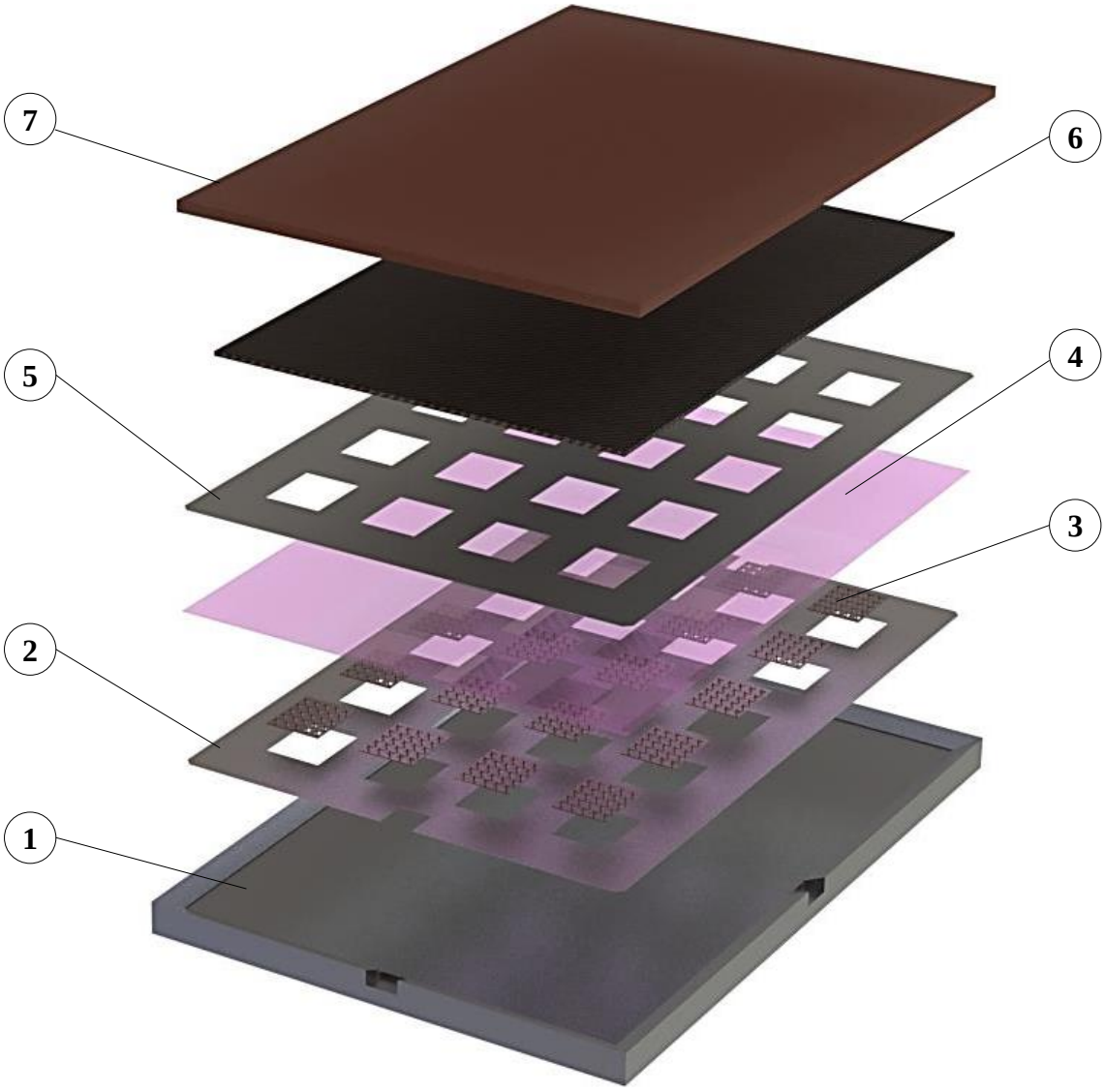

Fig. 31- Autoclave set-up.

The typical curing cycle for a M21 epoxy matrix features an autoclave cure of 2-hour dwell at 180°C with 7 bar pressure gauge applied at the beginning of the heat-up ramp. However, as it was explained in a related investigation [28, 57], this typical curing cycle had to be modified in order to prevent severe fibre breakage during pin insertion. Hence, the pressure level was increased to 7 bar, starting at 120°C. The cure cycle used for manufacturing the specimens is depicted in Fig. 32.

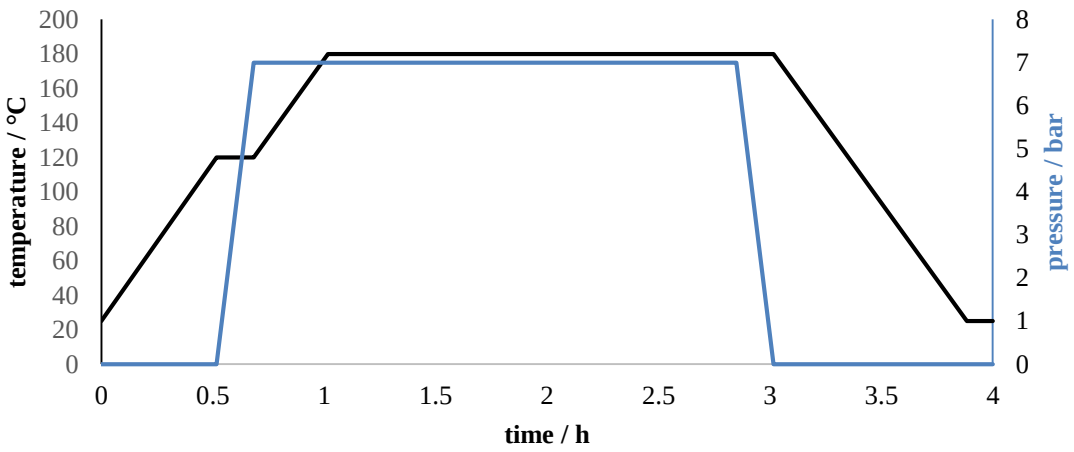

Fig. 32- Autoclave curing cycle.

After the autoclave cure, each plate was cut in table saw to obtain the 20 coupons for mechanical testing. This was a delicate step since specimens should have specific dimensions for the later step of bonding these to the pull-out tabs. Therefore, specimens were cut to a dimension that was slightly greater than the final desired one, so that specimens' edges could then be ground down in a consecutive step, to the exact dimensions of 25x30 mm.

5.5 Bonding

Preparation for bonding

After cutting and grinding specimens' edges to the right dimensions, a surface treatment was applied to both specimens and pull-out tabs to ensure a good bonding quality between them. The side of the specimen containing the metallic reinforcement sheet was firstly mechanically treated by grit-blasting its surface with Al_2O_3 (grain size 250-500 µm and blasting pressure of 7 bar) in order to roughen and increase the active surface. The first tested specimens were indeed simply treated by means of this treatment. However, during these first trials, it was found that this treatment was insufficient, as some specimens failed adhesively on the mechanically treated surface. Therefore, in addition to the mechanical treatment, a physical surface treatment (laser irradiation) was thereafter applied to the side of the specimens featuring the reinforcement sheet. Combining mechanical and physical treatments, lead to an enhanced adhesion quality since two levels of mechanical interlocking were created: a micro-roughness scale provided by grit-blasting treatment and a nano-structured surface realized by laser irradiation. Fig. 33 a) illustrates a set of specimens being treated by laser irradiation while Fig. 33 b) contrasts two different specimens after grit-blasting (right) and after both grit-blasting and laser irradiation treatment (left).

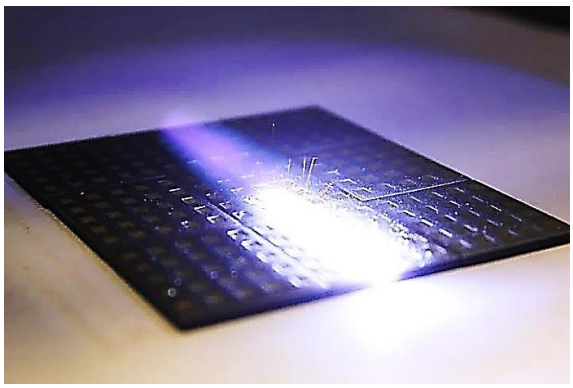

(a) laser irradiation of the reinforcement sheets

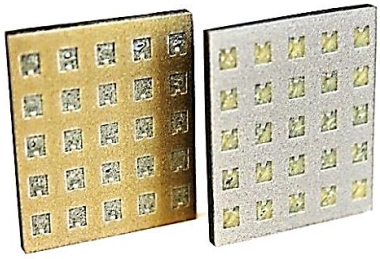

(b) specimen post reinforcement (left) laser treatment and (right) grit-blasting

Fig. 33- Specimens' surface preparation for bonding.

The side of the specimen containing the CFRP laminate was manually abraded with silicone carbide (SiC) abrasive paper (grain size of 220 µm) until disappearance of gloss and until the first plie of the laminate (+45°) was visible. Both, ground and grit-blasted faces of the specimens were subsequently cleaned with an isopropanol drenched fluff less cloth to ensure free contamination bonding surfaces.

Physical surface treatment by means of laser irradiation was also applied to the loading tabs, as some specimens were to be subjected to hot and wet environmental conditions. It was decided to apply this treatment because ingress of moisture could be critical for the adhesion quality between loading tab and specimen when any other surface treatment was applied instead. Fig. 34 a) shows the mentioned pull-out tabs being laser pre-treated and Fig. 34 b) shows a pull-out tab before (left) and after (right) physical surface treatment.

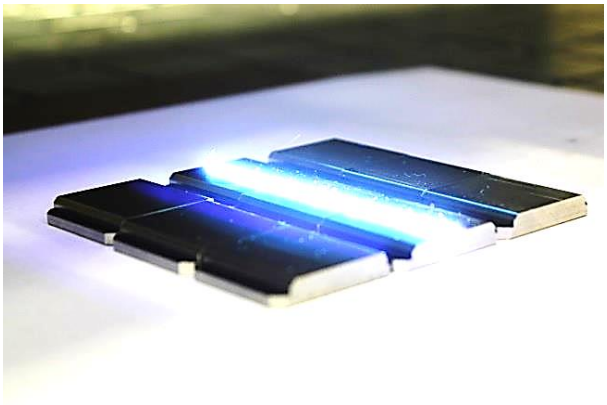

(a) laser irradiation of the pull-out tabs

(b) pull-out tab before (left) and after (right) laser treatment

Fig. 34- Pull-out tabs' surface preparation for bonding.

All specimens were bonded applying a 3M™ Scotch-Weld™ Structural Epoxy Adhesive EC-9323-2 B/A, commonly used for aircraft applications. To control the bond line thickness approximately 1 wt. % of solid spacer glass beads of 75-150 µm diameter supplied by Potters Industries LLC, were added to the adhesive.

Bonding procedure

A specific procedure was also drawn and additional tools were manufactured for a robust bonding process.

Prior to bonding, some kind of release agent treatment had to be applied to all the surfaces of the metallic tools that were to be in contact with the specimens, so that removal of those from inside the plates without any damage was possible. Thus, two coats of Marbocote TRE45ECO were applied to all surfaces of both plates (2 and 4), with a break of 30 minutes in between.

Bonding of the specimens to the pull-out tabs was then divided into two steps, as depicted in Fig. 35. In the first step (Fig. 35 a)), specimens (1) were inserted into the bonding plate (2) with the side featuring the CFRP laminate facing the bottom window of the plate (2). After adhesive and space glass beads application, upper pull-out tabs (3) were carefully laid down on top of the adhesive and manually pressured as the adhesive cure began shortly afterwards. To ensure an evenly distributed pressure during curing of the adhesive, the plate (4) was laid on top of the entire set-up. The whole set-up was then placed into a dry oven for adhesive curing, for 2 hours at 65°C, which is indicated for this type of adhesive. In the second step (Fig. 35 b)), the same procedure was repeated for the side of the specimen showing the CFRP laminate. The function of the two plates (2 and 4) was reversed in this step, with the plate (4) ensuring the correct alignment of both pull-out tabs and specimens and the other plate (2) serving as a pressure plate.

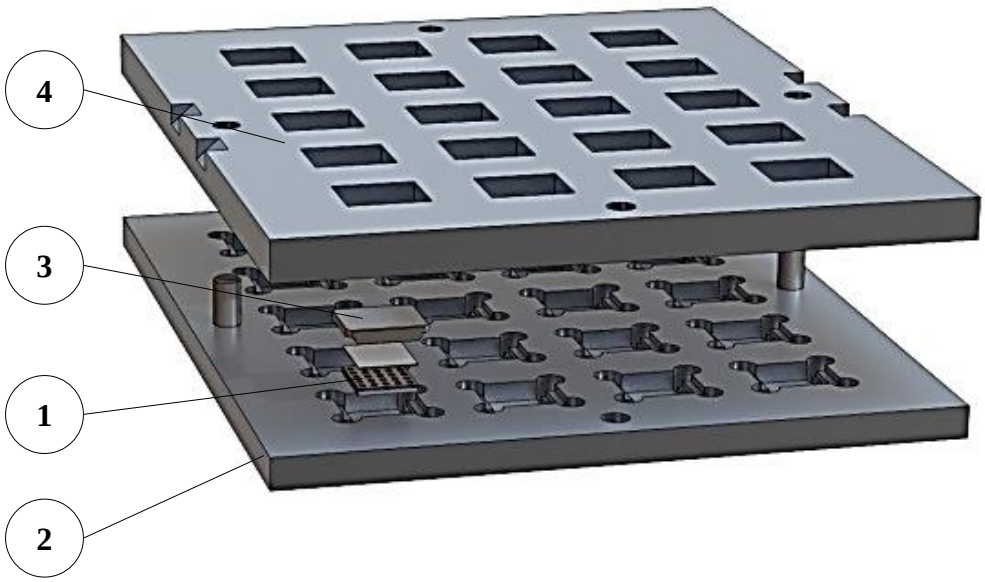

(a) bonding step 1: bonding of the upper pull-out tabs to the specimens

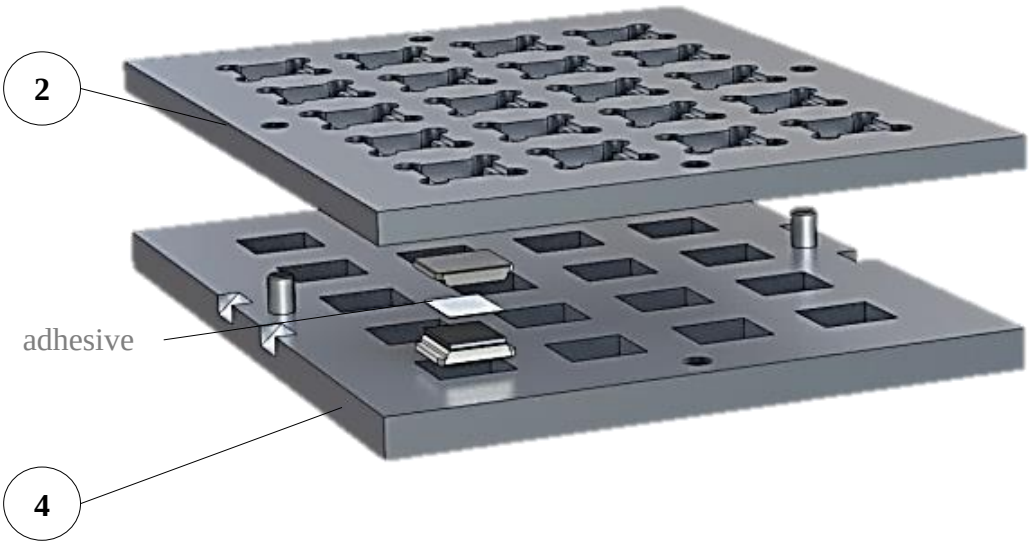

(b) bonding step 2: bonding of lower pull-out tabs to the specimens

Fig. 35- Bonding procedure.

After bonding the specimens to the pull-out tabs there was always some undesirable excess cured adhesive, squeezed out of the specimen; this could result in bonding between the laminate and the metallic reinforcement sheet. Therefore, this excess adhesive had to be erased by filing the edges of the specimen until full detachment between laminate and reinforcement was assured. Fig. 36 a) presents a picture of a final specimen.

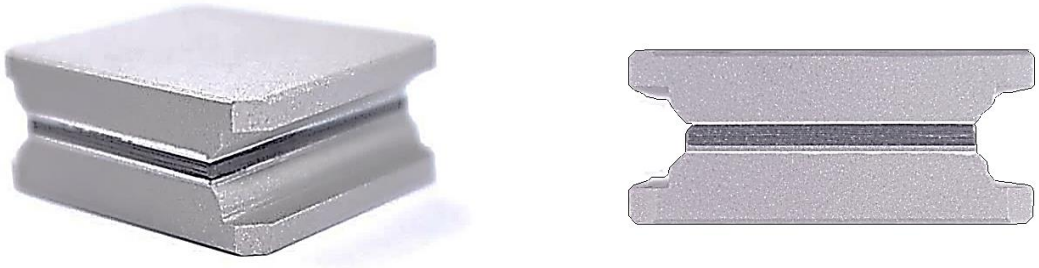

(a) side view of a final specimen

(b) front view of a final specimen

Fig. 36- Final specimen.

6 Experimental investigation

6.1 Reinforcement (post surface pretreatment) chemistry

After applying the respective surface pretreatment and before introducing into the laminate, the surface of a set of reinforcements was chemically analysed by means of x-ray photoelectron spectroscopy (XPS) to assess the degree of contamination and activation which is indicated by the content of carbon and oxygen, respectively.

As it can be seen from Table 3, both SAE 304 and Ti 15-3 physically treated reinforcements display the lowest content of carbon compounds and the highest degree of activation. Similar but slightly lower levels of activation were found for grit blasted surfaces but also significantly higher values of carbon contaminations were documented. Wet-chemically treated surfaces lead to the less favourable results, with the highest and lowest degrees of contamination and activation, respectively.

Given the same surface pretreatment, degree of contamination was considerably higher for stainless steel surfaces. In addition, registered values of oxygen content were mildly greater for Ti 15-3 pretreated surfaces.

Table 3- Carbon and oxygen compunds on reinforcements' surfaces: average content [2]

Material	Surface pretreatment	Carbon (%)	Oxygen (%)
SAE 304	HF/HNO_3	43.3	35.9
	GB blasting and plasma	31.3	52.5
	Laser irradiation	28.1	53.7
Ti 15-3	Turco 5578®	36.6	45.8
	Grit blasting and plasma	26.5	52.7
	Laser irradiation	25.2	52.8

6.2 Mode I pull-out testing

6.2.1 Testing procedure

Mode I pull-out tensile tests were performed to determine the traction-displacement relation of a CFRP reinforcing multi-pin structured sheet. Testing aid tools were designed and manufactured for this specific test.

Loading grips (1 and 2) were firstly screwed to a 10 kN Z010/TN testing machine (Zwick GmBH & Co. KG) with little clearance so as to allow small lateral displacements. As referred in chapter 4.2, two pull-out tabs (3 and 4) were glued to the top and bottom surfaces of the specimen (5). The specimen (equipped with pull-out tabs) was then inserted into the loading grips (1 and 2) in a way allowing the load to be applied at the tabs' outer flanks. By doing so, a uniform stress distribution along the sample could be ensured. The whole test set-up is depicted in Fig. 37.

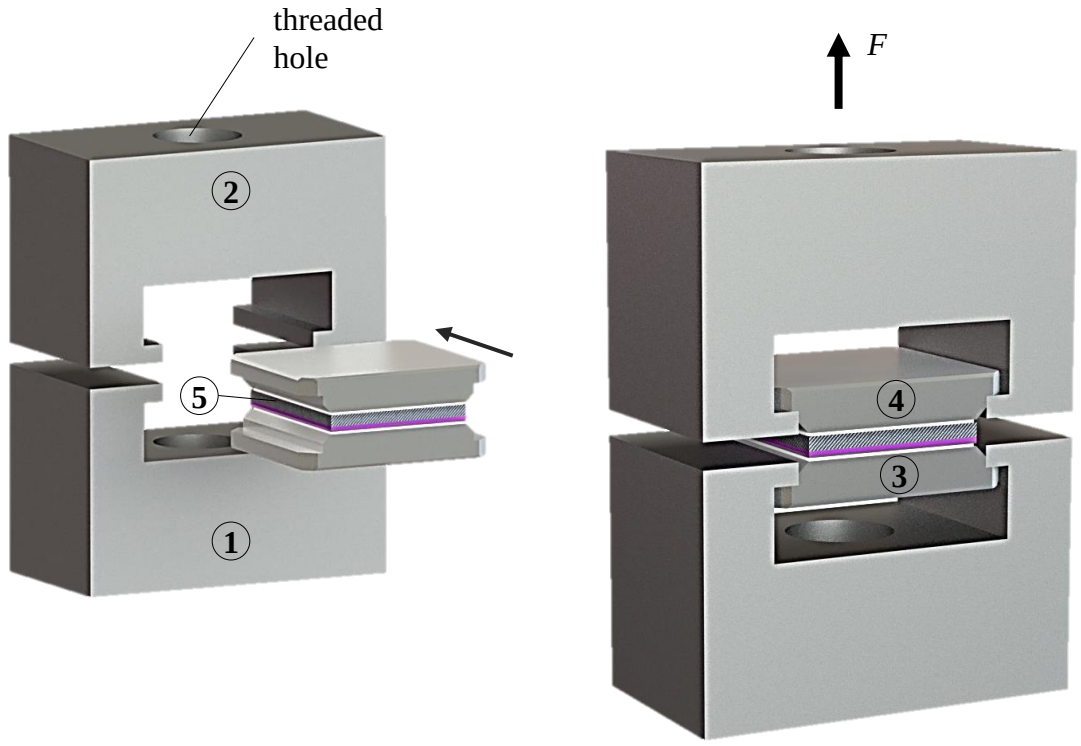

(a) coupling of the specimen (b) testing procedure

Fig. 37- Experimental set-up for mode I pull-out test.

All tests were performed at an average temperature and humidity of 23°C and 50%, respectively. Load-displacement curves were recorder at a constant cross-head speed of 1 mm/min until failure or complete pull-out of the pins. At least 4 specimens of each combination, *i.e.* reinforcement material, pin geometry and surface pretreatment were tested under mode I pull-out displacement. It should be noted that raw data supplied by the testing machine included the deformation of the whole experimental setup. Therefore, additional tests were performed on bonded only tabs and measured displacements were subtracted from the total displacement of the original specimens. Overall load applied was then divided by the number of spikes per specimen to derive the average bridging load of one single spike.

6.2.2 Force vs. displacement results

Mode I pull-out force-displacement results of all investigated configurations can be found in APPENDICES A and B. Within the same configuration, force-displacement curves showed very similar patterns. Hence, one representative curve of each configuration was selected and considered as the bridging law. Fig. 38 and Fig. 39 shows the selected representative curves of each configuration for straight and arrowhead pins, respectively.

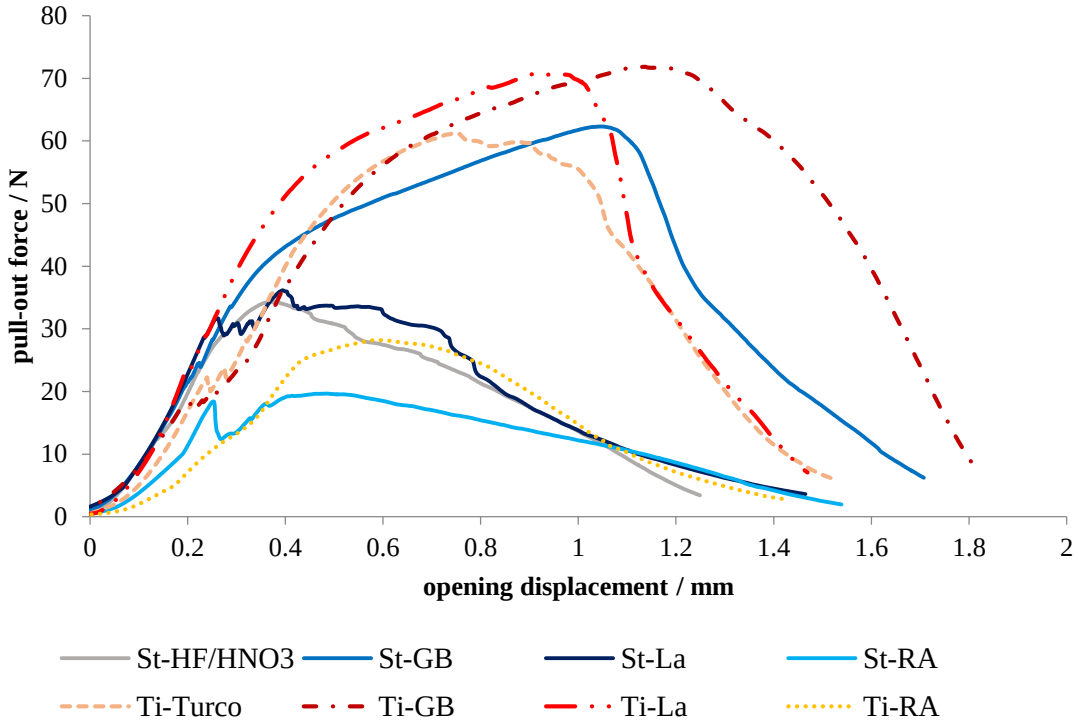

Fig. 38- Force vs. displacement representative curves of straight pins (mode I).

Contrary to what was expected, the functional relationship between bridging forces and associated opening displacement of these type of z-reinforcements does not follow a bi-linear nor a tri-linear law, as it was the case for the titanium rods and CF z-pins [33, 34, 37]. Notwithstanding the observable differences between curves of distinct configurations, the majority of measured load-displacement curves can be divided into three major stages. In the first stage, bridging forces increase at a linear rate with the pull-out displacement. During the second stage, bridging forces still increase linearly but with a slightly decreased slope. The third and final stage starts with a nonlinear force increase up to its max. value, followed by almost a linear load drop until "full-length" pin pull-out. This force drop seems to be more progressive and abrupt for SAE 304 reinforcements and Ti 15-3 spikes, respectively.

Besides those specimens featuring release agent pretreated reinforcements, all configurations displayed during their first stages, a discontinuity of their force-displacement curves that was also audible during testing through a "crackling" noise. At this point, applied bridging force on straight stainless steel reinforcements almost equals its maximum value (except grit blasted surfaces). In contrast to the titanium reinforcements, no consecutive linear stage was documented for these reinforcement material. Instead, a short non-linear "plateau"-like section is followed by the linear force decrease until complete pin pull-out.

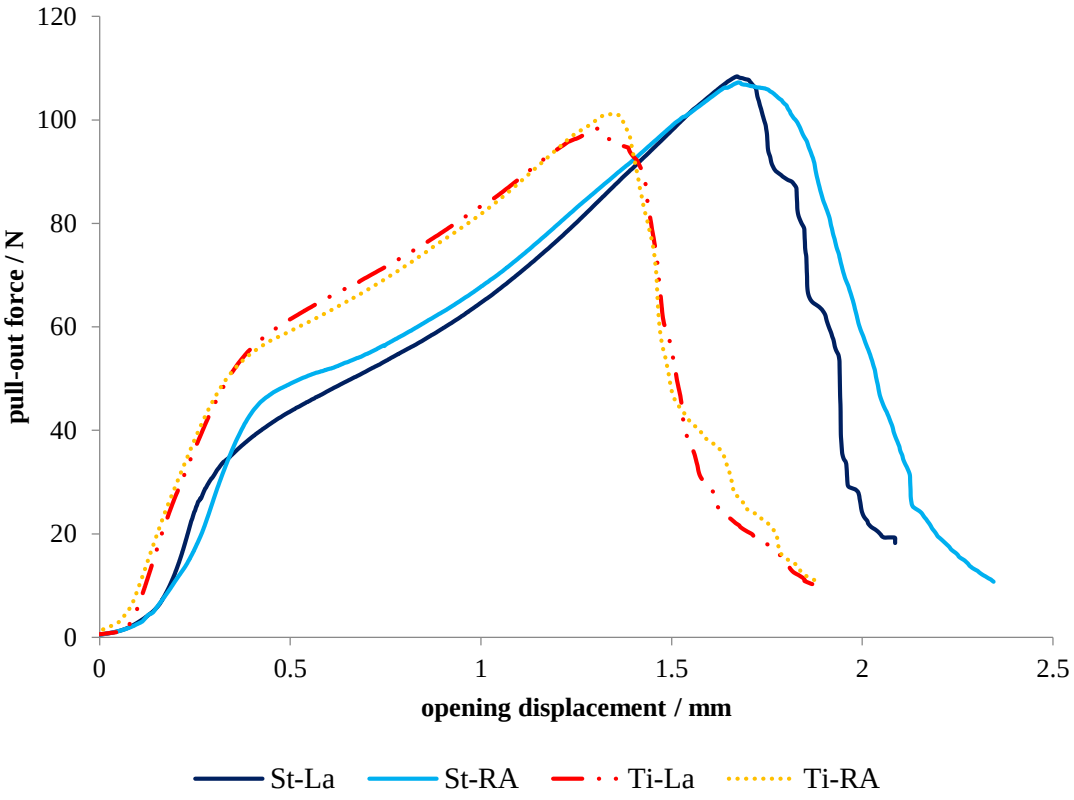

Fig. 39- Force vs. displacement representative curves of arrowhead pins (mode I).

It is furthermore observable for the straight and arrowhead Ti 15-3 and SAE 304 reinforcements' curves to nearly follow the same initiated path until a further increase of 70% and 28% on the applied load, Fig. 40 a) and b) respectively. While straight stainless steel reinforcements enter the second plateau-like stage post initial failure with a negative force offset, titanium reinforcements featuring a straight pins' geometry, proceed the same slope as that followed by the arrowhead spikes until stage three entering.

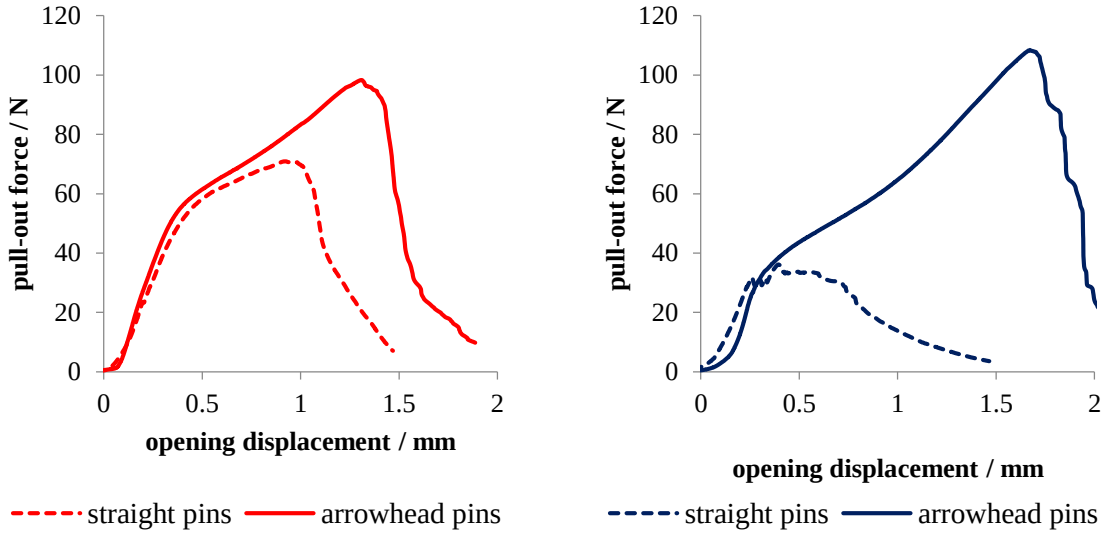

(a) Ti 15-3 pins

(b) SAE 304 pins

Fig. 40- Straight vs. arrowhead force-displacement curves (mode I).

Table 4 documents stiffness figures for the first two stages of the representative curves. Except for the physically pretreated sheets, SAE 304 specimens exhibited stiffer characteristics

than their titanium counterparts (1.1 up to 1.36 times higher). However, according to the intrinsic properties of the reinforcement materials (Table 1), one would expect to find almost to times higher stiffer characteristics for the steel reinforcements. According to Table 4, both materials display during the first stage of their force-displacement plots a considerable dependence between applied surface pretreatment and stiffness attributes. Maximum specimens' elasticity was documented for those reinforcements that received a coat of release agent, followed by the Al_2O_3 pretreated samples. On the other hand, laser structured surfaces were the ones revealing more rigid characteristics during this stage with slightly smaller values being documented for those configurations treated by wet-chemical means.

Table 4- Average stage I and II stiffnes figures for all configurations (mode I; dimensions em N/mm).

stage	**SAE 304**						**Ti 15-3**					
	straight				Arrowhead		straight				arrowhead	
	GB	HF/ $HN0_3$	La	RA	La	RA	GB	Turco	La	RA	La	RA
I	134.9	153.1	178.1	148.5	257.1	200.1	116.9	143.4	197.4	109.0	184.2	175.9
II	29.3	-	-	-	53.3	54.7	27.0	28.8	31.1	-	46.8	47.9

6.2.3 Post failure analysis

Post testing campaign, the fracture surface of a set of reinforcements was analysed via light microscopy in order to assess the spikes' degree of plasticization and in this way infer about the energy absorbing mechanisms prevalent in the pull-out process. For this purpose, for each analysed pin, deformations in the x and z directions (see Fig. 42) were measured. Deformation in the x direction was directly obtained by simply measuring the horizontal distance of the gap edges (between pin root and its previously surrounding resin), whereas deformation in the z direction was calculated by subtracting the original height of the pin (height of several reference untested pins was measured) from the final height of the deformed pin. These height measurements were made through the focus variation (FV) method, a 3d measurement technique- Fig. 41.

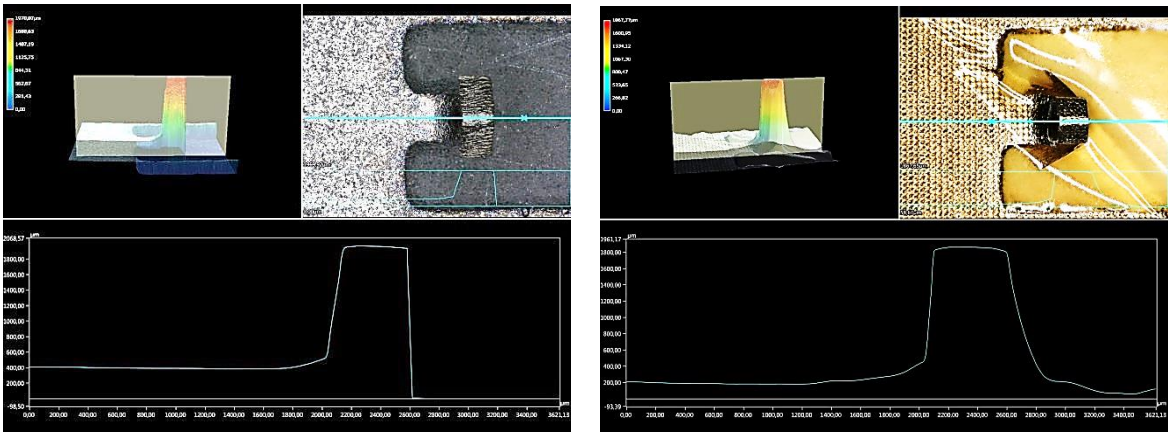

(a) Ti-S untreated and untested pin (reference) (b) post pull-out testing St-S-La pin

Fig. 41- Reinforcements' light microscope (top) top and (bottom) front view profiles (100x magnification; mode I).

Post failure analysis of the reinforcements via light microscopy allowed the definition of three particular states of deformation (state A, B and C), as depicted in Fig. 42. Side view of straight release agent treated spikes (both SAE 304 and Ti 15-3) initially suggested that no plasticization occurred to those pins during testing, namely state A. Aside from the grit-blasted

surfaces, the same was observed for the remaining straight SAE 304 configurations. Yet, resin cracks around pin root (see Fig. 43 a)) and lateral offset between laminate and reinforcement sheet observed during testing, indicated that those spikes were subjected to elastic deformation before pin-laminate sliding onset, as in state B. To confirm this, a sample of each of these configurations was tested close to their limits of linearity and released subsequently; no gap between reinforcement sheet and laminate was visible or only barely visible. This way, a temporary state of deformation (state B) was confirmed for those specimens that due to elastic recovery no post failure residual plasticization was documented (state A).

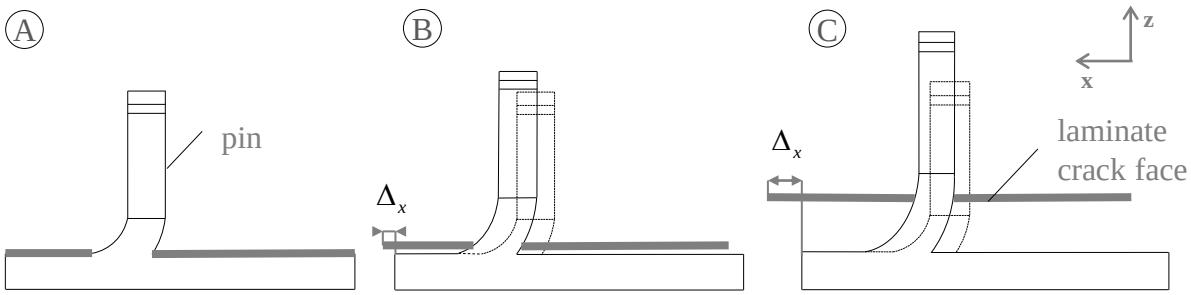

Fig. 42- Spikes' possible states of deformation during mode I pull-out test [2].

For the remaining straight configurations, a considerable residual pin deformation was detected in both x and z directions as indicated in state C, in ascending order: St -GB, Ti -GB, Ti -La, Ti - Turco. Besides resin cracks around the pin root (Fig. 43 a)), light microscopy analysis revealed considerable gaps between root and surrounding resin (Fig. 43 b)).

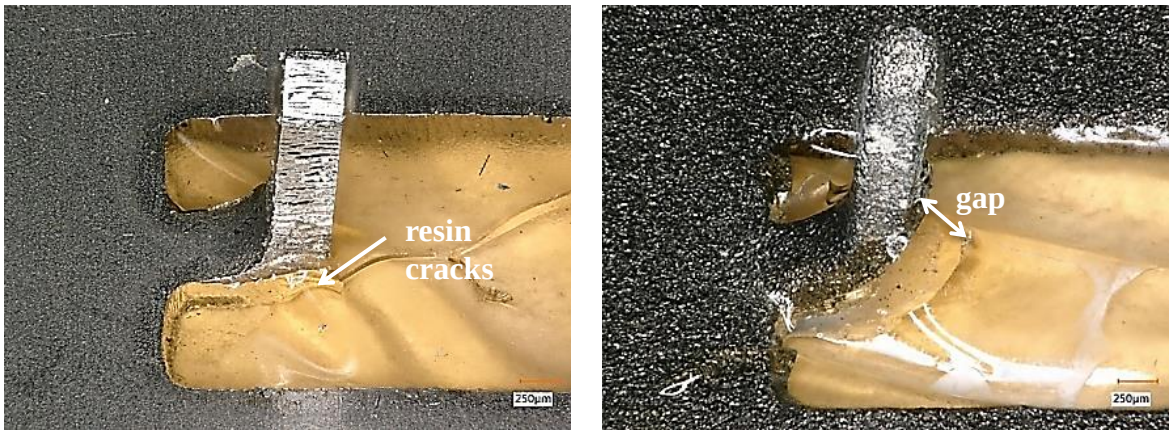

(a) St-S-RA spike (gap barely visible)

(b) St-S-GB spike (gap clearly visible)

Fig. 43- Post pull-out reinforcements' side views.

Fig. 44 and Fig. 45 present the measured deformation values in the x and z directions as well as the total derived plasticization experienced during the pull-out process for straight and arrowhead shaped spikes, respectively.

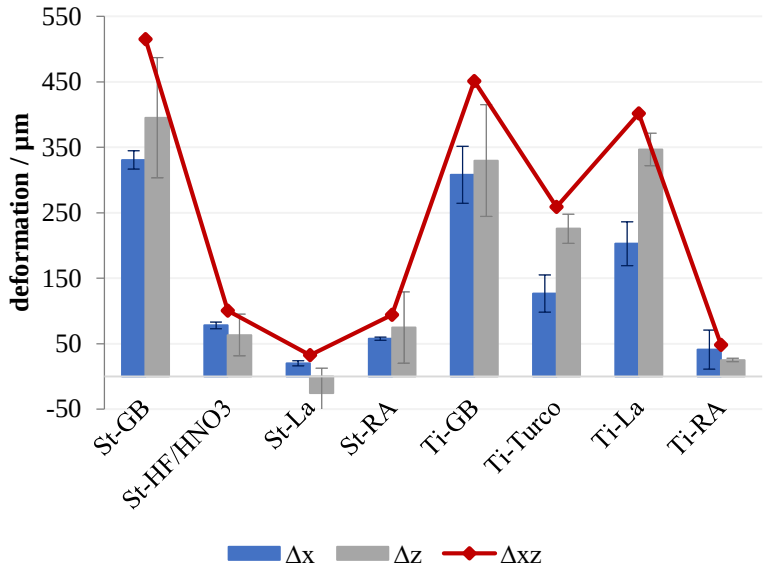

Fig. 44- Straight pins' measured deformations post pull-out failure (mode I; dimensions in µm)

Among the straight batches, grit-blasted surfaces revealed the highest levels of deformation in both x and z directions, with the SAE 304 spikes displaying slightly higher values than the Ti counterparts (Δxz=515,1µm vs. Δxz=451,27 µm). This fits well with the measured load-displacements curves where energy absorption levels of grit blasted samples were higher due to not only greater bridging forces but also a longer second stage and a more convex third bridging stage. Physically treated titanium spikes also showed considerable plasticization levels, close to the Al_2O_3 treated counterparts (Δxz=401,53 µm). This was not observed for the SAE 304 batches that were also pretreated by means of laser irradiation. Actually, this configuration displayed the poorest levels of deformation among straight configurations. While wet-chemically Ti 15-3 treated spikes also revealed a substantial degree of deformation (Δxz=258,85 µm), SAE 304 acid etched reinforcements showed little deformation, even comparable with those spikes coated with a release agent liquid film (Δxz=100.34 µm against 94,11 µm, respectively).

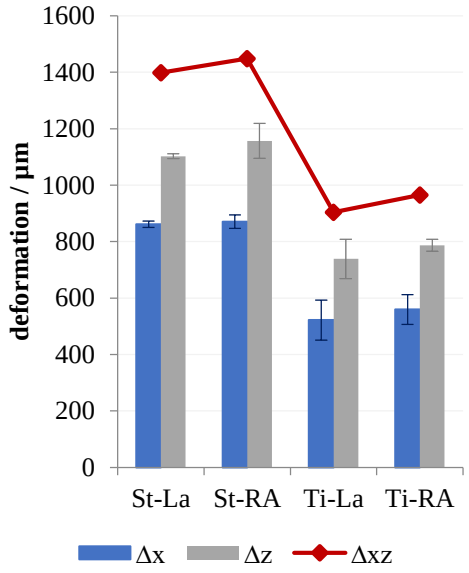

Fig. 45- Arrowhead pins' measured deformations post pull-out failure (mode I; dimensions in µm)

Reinforcements featuring arrowhead shaped pins revealed degrees of plasticization that were more than two times higher than the same straight configurations, *i.e.* with the same surface morphologies. Both SAE 304 and Ti 15-3 release agent pretreated spikes' residual deformations were higher than those treated by means of laser, which strongly indicates that induced pretreatment adhesion and surface morphology attributes do not have a considerable influence on the performance of these spikes. At last, it should be mentioned that SAE 304 reinforcements featuring an undercut geometry display more than 1,5 times the extent of deformation documented for the Ti batches (Δxz=1399,3 µm and Δxz=1448,2 µm vs. Δxz=904,6 µm and Δxz=965,8 µm for laser and release agent pretreated spikes, respectively).

6.2.4 Initial failure force vs. max. force vs. energy absorption

For a better understanding and comparison between transition points of the load-displacement curves from Fig. 38 and Fig. 39, recorded initial and max. failure forces are correlated with levels of energy absorption capacity in Fig. 46. Initial failure force levels were recorded by registering the first audible "crackling" noise during testing, whereas the amount of absorbed energy was calculated by measuring the total area under the force-displacement plots.

As shown in Fig. 46, physically pretreated reinforcements were the ones bearing the highest bridging loads prior to failure initiation, with titanium spikes failing slightly earlier than the SAE 304 counterparts, though (21.84 ± 1.36 N vs. 27.17 ± 3.32 N). When compared with traditional grit blasting surface pretreatment, both laser structured surfaces (SAE 304 and Ti 15-3) revealed increased bridging forces of up to 15% prior to failure onset. The trend of SAE 304 spikes showing in general higher bridging forces at failure initiation was also documented for the remaining configurations, both straight and arrowhead pinned samples, except for the wet-chemically pretreated sheets (17.00 ± 4.94 N against 19.79 ± 1.85 N). Within the same material, wet-chemically treated sheets were the ones revealing the worst bearing capabilities prior to the aforementioned discontinuity. It is furthermore noticeable for the configurations featuring an undercut pins' geometry to display slightly higher values of force at initial failure than those with a straight pin shape (laser). At last, as it was referred before, no crackling noise during testing was detected for release agent treated batches and therefore no initial failure forces were included in Fig. 46 for this configuration.

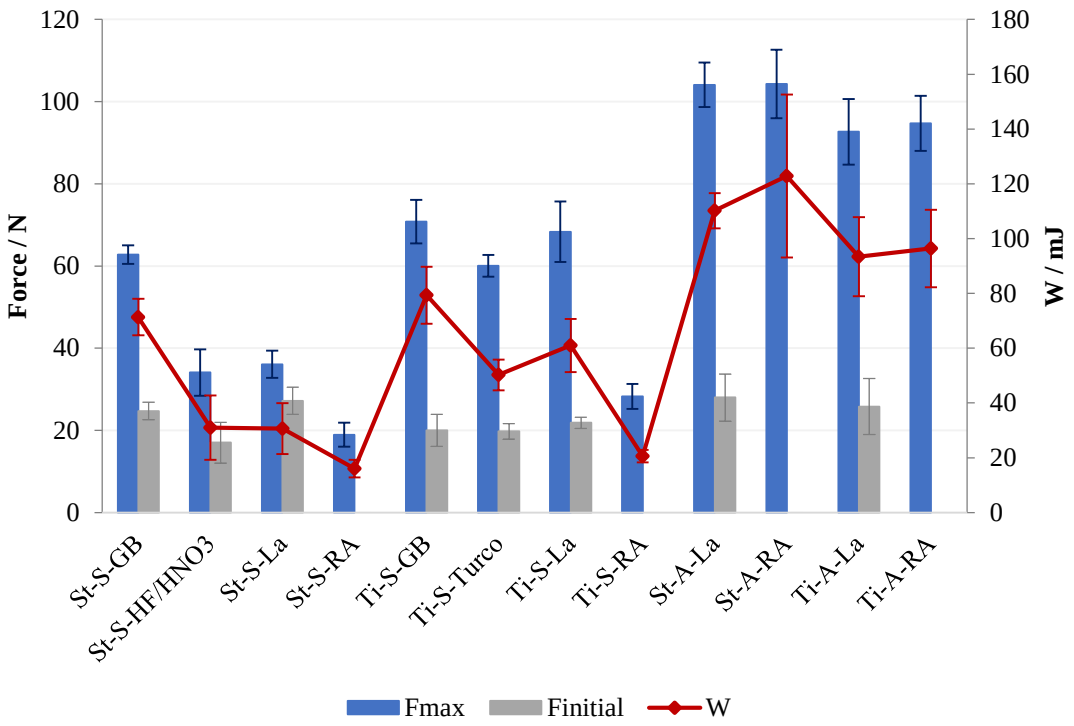

Fig. 46- Initial and max.failure forces and energy absorption for mode I pull-out test [2].

Contrary to what was reported for bridging loads at failure initiation, higher levels of max. force were, in general, documented for titanium spikes. In fact, Ti 15-3 reinforcements can carry nearly twice as many forces displayed by stainless steel pins (except grit-blasted surfaces). Still, Al_2O_3 pretreated titanium surfaces endured significantly higher loads than the SAE 304 counterparts (70.79 ± 5.27 N against 62.78 ± 2.29 N), with a high scatter though.

Given the same reinforcement material, arrowhead reinforcements showed very similar load bearing capabilities regardless of the surface morphology. For this reason, it can be concluded that for such reinforcements, the applied surface pretreatment only has influence on the previously mentioned first stage of the bridging law.

For both materials, among all investigated surface pretreatments, grit blasted configurations revealed the highest levels of energy absorption *i.e.*, greatest work against pull-out. This is not only a consequence of higher bridging forces at ultimate failure but also due to a more extended second stage and a more convex shaped third stage (particularly for the SAE 304 spikes). Laser pretreated titanium configurations also displayed increased levels of maximum force and energy dissipation, close to the grit blasted ones. The same was not documented for the SAE 304 counterparts as they exhibited only half of the max. forces and energy absorption capacity values of the mechanically pretreated sheets, close to the HF/HNO_3 treated batches. Marbocote TRE45ECO reinforcements obviously showed the lowest load bearing capabilities and therefore work against pull-out (both investigated reinforcement materials).

6.2.5 Discussion

Experimental results from multi-pin pull-out tests suggest the functional relationship between bridging force and associated crack opening displacement to be highly dependent on induced surface pretreatment morphology scale and CTE of the reinforcement material. Still, it is possible to observe a similar trend in the evolution of the distinct curves. Three major stages in the pull-out force-displacement curves can be distinguished, established by different energy absorbing mechanisms, as schematically depicted in Fig. 47.

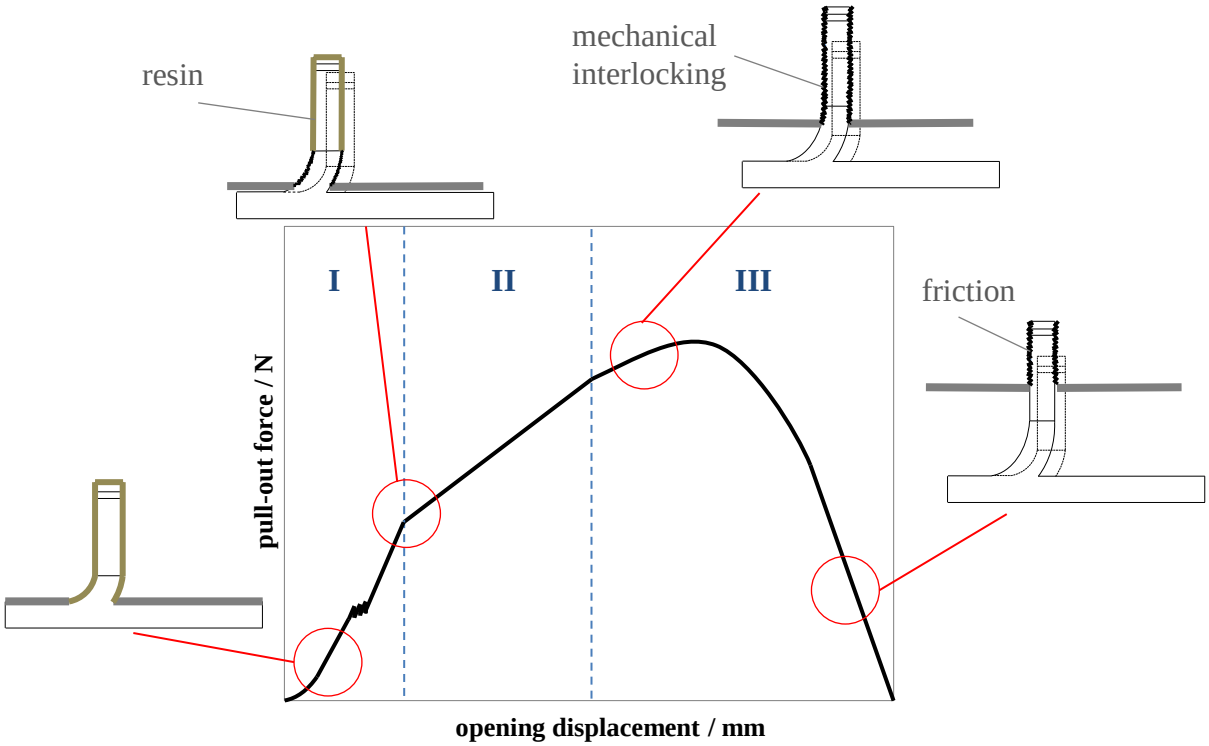

Fig. 47- Mode I pull-out generic bridgign law [2].

In the first stage, a linear force increase provokes elastic deformation only of the pin. At some point in this stage, a discontinuity of the force-displacement curves was detected and heard through a "crackling" sound during testing. It is strongly suggested that this discontinuity represents the initial adhesive failure at the bottom of the pin (where its maximum elongation occurs). Before the discontinuity, the tensioned pin is then fully bonded to the surrounding resin. As adhesion failure starts, the bonded part of the pin experiences stretching whereas the debonded part is subjected to interfacial friction. As the crack propagates from the bottom towards the pin tip, adhesion forces diminish and interfacial friction gains importance.

It seems that at this first stage, overall stiffness of the specimens is determined by adhesion and materials properties. A clean and chemically activated nanostructured surface documented in Table 3 for a laser irradiated surface is known to possess a further dimension of mechanical interlocking between metal and surrounding resin epoxy and therefore an increased adhesion quality between metal spike and host laminate [38, 60, 67, 71]. The stiffer characteristics and the comparatively higher bridging loads before discontinuity documented for these surfaces support the assumption of enhanced adhesion features for a nano-structured surface. By contrast, the surface morphology on a macro-scale created by a grit blasting surface pretreatment, resulted in a more elastic behaviour of those specimens at this stage due to inferior adhesion features and significantly higher degree of contamination. Also, reinforcements that received a release agent coat did not show any discontinuity in their bridging laws since no special adhesion attributes were present for those surfaces.

The comparatively lower stiffness of titanium reinforcements resulted in specimens with a slight inferior global stiffness and higher stress concentrations at the bottom of the pin. Therefore, given the same surface morphology, a more premature initial adhesion failure was documented for specimens featuring a Ti 15-3 reinforcement, when compared to those reinforced by SAE 304 pins. However, comparatively larger mismatch between CTE of a SAE 304 reinforcement and laminate induces higher thermally residual stresses post specimen curing cycle. Obviously, these stresses lead to less contact between pin and surrounding laminate post

(initial) adhesive failure and consequently lower frictional forces at the debonded pin part. This was confirmed by the force-displacement curves of those specimens that were pretreated with release agent and that did not feature any sizable surface morphology nor adhesion at all; bearing load capacity of those specimens was slightly higher when a Ti 15-3 reinforcement was used instead of a stainless steel one (see Fig. 46).

A tri-linear relationship between stage two entry, measured residual deformations and work done against pull-out is apparent. On the one hand, failure analysis of a set of specimens that were tested only until the end of the linearity in stage one and unloaded subsequently, showed only barely or no visible deformation of the pins. Also, specimens tested until complete pin pull-out but did not enter the second stage (particularly SAE 304 configurations), revealed a negligible or no plasticization at all. Hence, it can be concluded that the second stage of the bridging law is the one in which virtually all the plasticization of the pin occurs. Once the equivalent stresses at the critical cross section of the pin reach the material´s yield strength, plastic deformation begins at this section and force-displacement curves' characteristics enter the consecutive second stage. This explains why for some particular configurations (Al_2O_3 treated spikes), despite bridging forces being higher for Ti 15-3 spikes, SAE 304 counterparts display larger residual deformations; this is due to the comparatively lower yield strength of the stainless steel reinforcements. Still, the ratio between applied loads at stage two entry of the two reinforcement materials is significantly smaller than that between yield strengths. This issue will be addressed later on in chapter 7.1.1, by analyzing the pin's micromechanics through a structural approach. Bridging forces at this second stage still evolve linearly, but with a considerable decreased slope.

At the end of the plasticization stage, pins have already debonded completely from the surrounding epoxy resin. As force-displacement curves enter the consecutive final third stage, bridging forces still increase slightly but in a non-linear fashion up to its max. value. This is most probably due to the interfacial mechanical interlocking effect between the rough debonded pin's surface and surrounding CF/epoxy resin. As soon as applied loads reach their max. value, pin-laminate sliding begins with bridging forces decreasing in an almost linear way until "full-length" pull-out of the spikes. During this sliding phase, closure forces against further crack opening are then entirely driven by frictional pull-out. Thus, pretreatment induced surface morphology determines the progression of the bridging laws at this stage. This is particularly visible for the Ti 15-3 force-displacement curves where grit-blasted batches display an extended second and a more convex third stage curve shape whereas a nano-structured laser surface displays a short second and a more narrowed final stage. This is a direct consequence from the roughness scale created by the different surface pretreatments. As it was described in chapter 5.2, an Al_2O_3 blasting treatment creates the roughest surface on a macro-scale that obviously, provokes higher coefficients of friction when compared to the laser treated surfaces that display the smallest morphology scale on a nano-dimension. Besides the lower roughness scale of nano-structured surfaces, as the crack propagates around the pin, the nano-cavities are infiltrated with resin implicating further lower friction with the surrounding laminate.

Considering the ratio between energy absorption and load bearing capabilities of straight pins, while SAE 304 reinforcements benefit from higher strains to failure, higher strength of titanium spikes allows them to further sustain the applied load until forces are high enough to cause laminate fragmentation.

Regarding the arrowhead reinforcements, the mechanical constraint effect induced by an undercut geometry obviously prevails over adhesion and friction attributes. Hence, for those specimens applied surface pretreatment only impacts on their failure behaviour during the first linear stage, with material properties gaining importance thereafter.

As outlined before, arrowhead and straight force-displacement curves tend to progress identically until adhesive failure of the latter named. Given the same surface morphology, curve characteristics of arrowhead Ti 15-3 spikes follow the same slope as their straight counterparts until a further increase on the applied load of approximately 70% of its max. bridging force. At this point, straight reinforcements have failed adhesively with curves' characteristics entering the consecutive third stage starting in non-linear force increase up to its max. value followed by more a less force drop (laser pretreated surfaces). Arrowhead spikes further sustain the applied loads by additional deformations until forces are high enough to provoke laminate fragmentation and failure. In the case of specimens featuring SAE 304 reinforcements, it was observed for the arrowhead configurations to only follow the same curve path of the straight counterparts until beginning of the second stage (28% of maximum load). By then, straight pins have failed completely without going through the previously mentioned second stage of the bridging curve. This clearly suggests that induced frictional features from physical pretreatment on a stainless steel surface are weaker than that created on a titanium alloy. Arrowhead spikes further deform plastically with higher bridging forces until laminate failure.

6.3 Mixed-mode I/II test

6.3.1 Testing procedure

In order to simplify the manufacturing process of the specimens, a modified shear jig (Fig. 48) that enables the usage of the same pull-out tabs conceived for mode I tensile tests, was developed for this test. Initially, the aim was to develop a testing procedure that would allow almost pure mode II loading conditions to be applied on the z-reinforced laminates. Hence, the opposing shear arms (1 and 2) were restricted from rotation by firmly fixation to the robust Steinel Normalien ST 40 load cells (3 and 4, respectively). However, as demonstrated in [31, 37, 42] and observed during testing, pure shear-out loading conditions cannot be applied in practice due to opening mechanisms acting at the delamination crack.

According to Fig. 48, the bottom part of the load cell (3) was simply supported at the machine's base (stationary), whereas the upper part (4) was attached to the machine's driven cross head. After attaching the shear arms (1 and 2) to the load cell (3 and 4), driving grips (5 and 6) were introduced into them. The specimen (7) was then carefully inserted with some clearance between the two driving grips (5 and 6). Finally, a driving screw (8 and 9) allowed the adjustment of the specimen's clearance through the relative transversal motion between shear arms and driving grips.

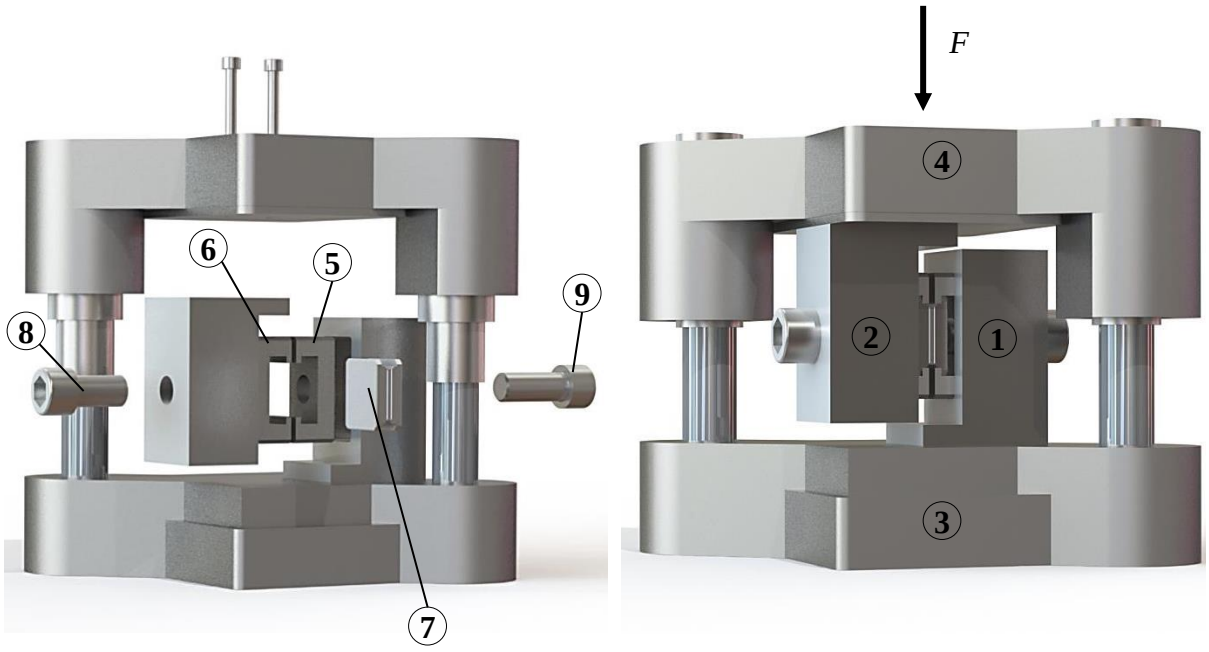

(a) exploded view of the mixed-mode test shear rig (b) mixed-mode I/II testing procedure

Fig. 48- Experimental set-up for mixed-mode I/II test.

All tests were conducted on a 10 kN Z010/TN testing machine (Zwick GmBH & Co. KG) at an average temperature and relative humidity of 23°C and 50%, respectively. Load-displacement data was recorded at a constant cross-head speed of 0.5 mm/min until failure or complete pull-out of the pins. At least 4 specimens of each combination/configuration *i.e.*, reinforcement material, pin geometry and surface pretreatment were tested under mixed-mode I/II shear displacement. As for mode I traction tests, raw test data supplied by the load machine included the deformation of the whole experimental setup. Hence, additional tests were

conducted on bonded only tabs and derived displacements were subtracted from the original plots. Overall load applied to the set-up was then divided by the number of pins in one specimen to derive the average bridging load per single spike.

6.3.2 Force vs. displacement results

Multi-pin shear-out tests were conducted for all investigated configurations. Mixed-mode I /II force-displacement curves of all tested specimens can be found in APPENDICES C and D. Within the same configuration (surface pretreatment, reinforcement's material and pin geometry), the difference between experimental results is reasonably small. Thus, one curve of each combination was selected and considered as the representative bridging law of such configuration. Fig. 49 and Fig. 50 presents the representative mixed-mode I/II derived bridging laws for straight and arrowhead configurations, respectively.

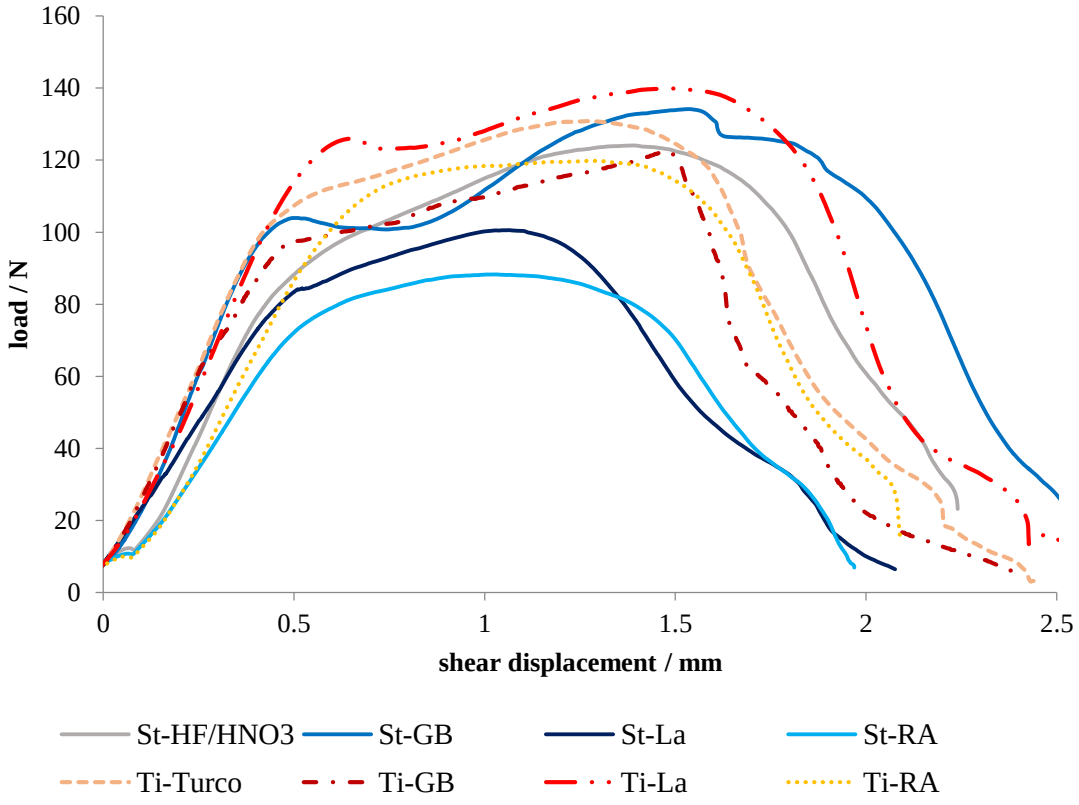

Fig. 49- Force vs. displacement representative curves of straight pins (mixed-mode I/II).

Both pins' geometries show a similar trend of their force-displacement curves that can be divided into three main stages. In the first stage, a linear load increase is followed by a transitional section where forces either develop progressively slowly or continue at the same rate until a sudden force drop occurs. Unlike to what happened for mode I tensile tests, no "crackling" sound was detected while testing, neither any apparent discontinuity was observed during this first loading stage of the derived force-displacement curves. Within the same configuration, curve's course of some specimens at the transitional section is progressive with lower force levels being reached and with its slope decreasing gradually until stage two entering. For others, force-displacement curves proceed the initiated slope (stage I) up to higher bridging forces, followed by a "shoulder"-like shaped curve where a sudden load decrease is accompanied by an extensive crack displacement until curve characteristics enter the subsequent second stage. At this second stage, derived force-displacement curves still develop in a linear manner but with a considerable decreased slope, though.

To the above mentioned second stage succeeds a third final stage starting in non-linearity until forces reach their max. value. During this non-linear load increase, bridging forces provided by those specimens that displayed a considerable amount of sheared-off spikes, fall suddenly with almost no additional crack displacement (straight grit blasted and arrowhead laser pretreated Ti 15-3 configurations). For the remaining configuration, as forces reach their max. value, a more or less linear load decrease follows. Also in this stage, a final section where forces evolve in a more stable way with the associated displacement can also be distinguished for most of the investigated configurations.

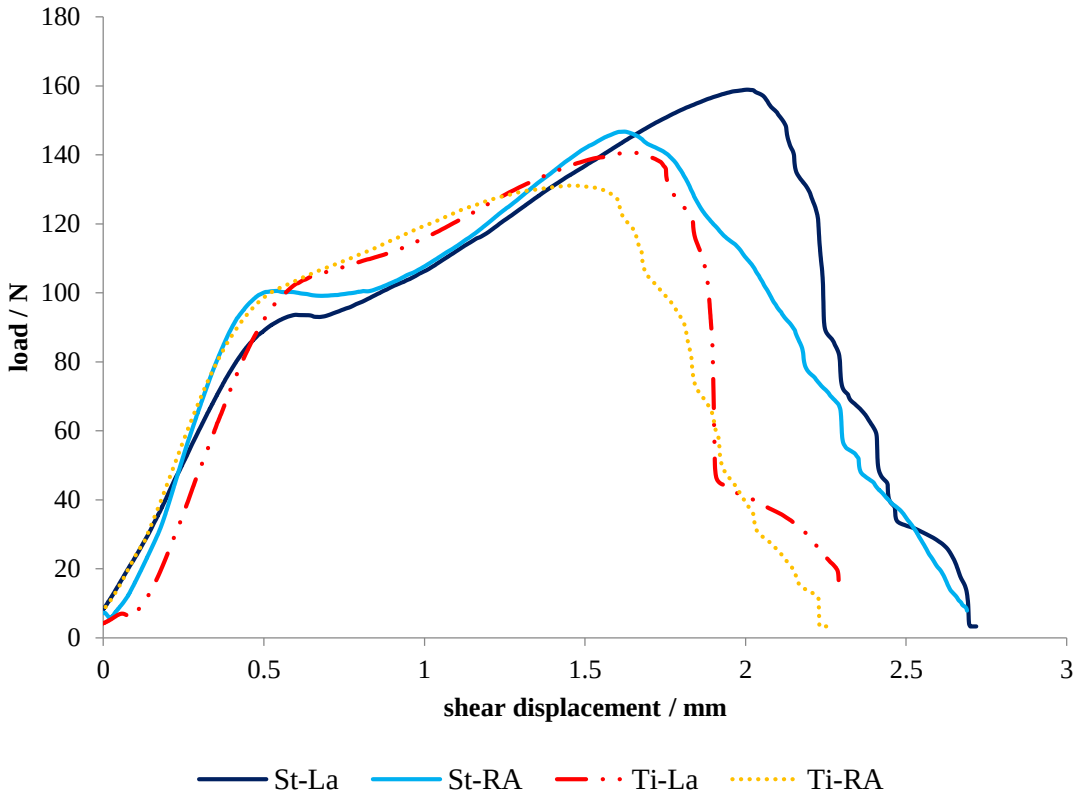

Fig. 50- Force vs. displacement representative curves of arrowhead pins (mixed-mode I/II).

Stiffness figures at the first two stages were also estimated for all derived load-displacement curves of all investigated configurations. Before the transition section, Ti 15-3 straight batches revealed comparable overall stiffness values of 267.7 N/mm ± 41.2, 263.01 N/mm ± 14.1, 273.43 N/mm ±12.4 and 226.5 N/mm ±20.2 for grit blasted, alkaline etched, laser and release agent pretreated surfaces, respectively. In contrast, among straight stainless steel configurations, a considerable scatter of measured values of rigidity was encountered. Furthermore, SAE 304 batches were in general less stiff (up to 30%) when compared to the titanium counterparts; values of 269.9 N/mm ± 35.0, 199.13 N/mm ± 13.3, 226.3 N/mm ± 34.8 and 199.4 N/mm ± 53.1 could be determined for the sequence indicated above. All configurations enter the subsequent second stage with their curves featuring a considerable slope decrease of up to 90%. Specimens featuring an undercut pin geometry revealed analogous stiffness characteristics for the first stage but remarkably stiffer characteristics of up to 3.6 times higher than their straight counterparts during the second stage of their bridging laws.

As shown in Fig. 51, force-displacement curves of arrowhead shaped pins tend to follow upon the path of their straight counterparts up to at least second stage entry. At this point, both geometries enter the subsequent second stage with a considerable slope decrease that is more pronounced for straight configurations. It is furthermore noticeable for the straight configurations (both materials) to display a more concave final third stage with forces

decreasing continuously with the transversal displacement instead of a third narrow stage where forces drop suddenly, documented for the arrowhead configurations. Finally, it should be pointed out that while an arrowhead SAE 304 pin bears significantly higher bridging loads through additional deformations than those endured by a straight stainless steel spike (Fig. 51 a)), maximum resistance of a Ti 15-3 spike is more or less identical regardless of its geometry (Fig. 51 b)).

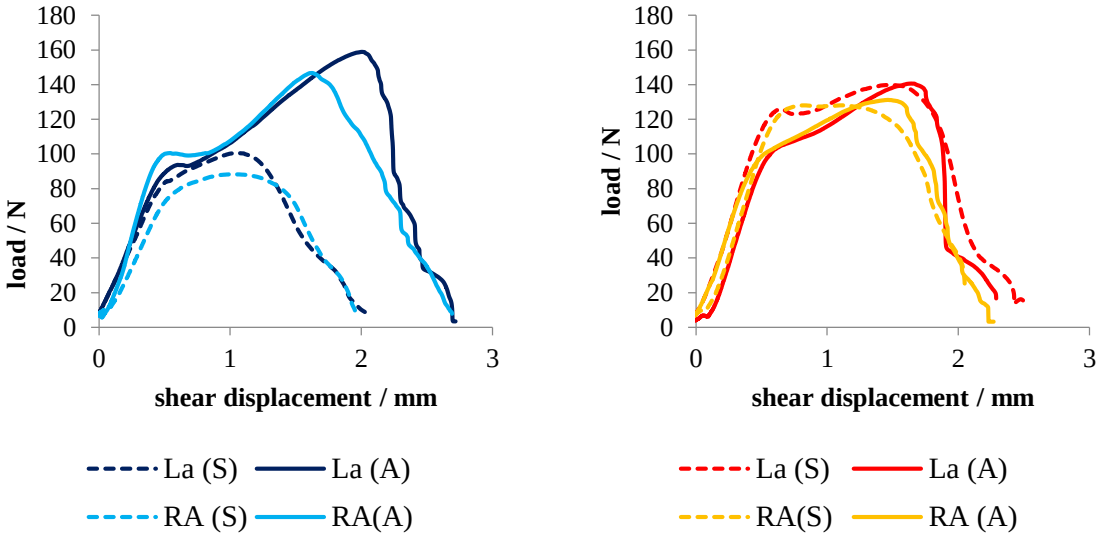

(a) SAE 304 pins (b) Ti 15-3 pins

Fig. 51- Straight vs. arrowhead force-displacement curves (mixed-mode I/II).

6.3.3 *Post failure analysis*

Similar to mode I traction tests, a set of reinforcements of each configuration was light microscopically examined post failure in order to analyze the failure behavior of such pins under shear loading conditions. Deformation in the x direction was directly obtained as depicted in Fig. 52 and registered in Table 5.

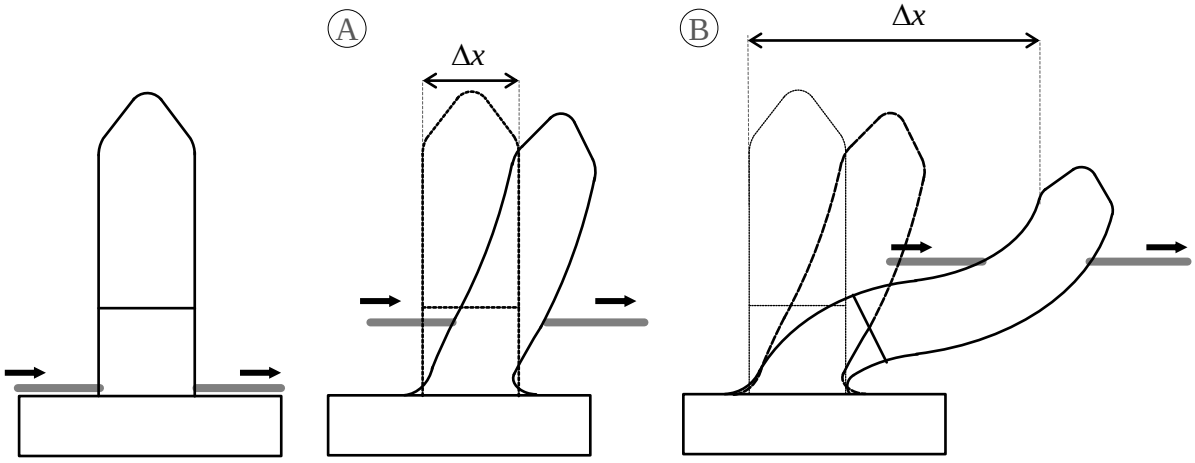

(a) no deformation of the pin (b) pin bends around its root (c) pin bends around its root and crack face

Fig. 52- Spikes' possible states of damage during mixed-mode I/II test.

Front view analysis of specimens subjected to mixed-mode I/II forces allowed the definition of two particular states of damage, as illustrated in Fig. 52 b) and c). Except Ti 15-3 release agent treated pins, which simply bent around their roots, namely state A (Fig. 52 b)), all configurations investigated in this work displayed a type B-like post failure deformation state as schematically depicted in Fig. 52 c). Fig. 53 a) contrasts the simple post failure deformation exhibited by a release agent coated spike with a highly plasticized Al_2O_3 pretreated pin (Fig. 53 b)).

(a) Ti-S-RA spike (b) Ti-S-GB spike

Fig. 53- Post shear-out reinforcements' front view.

During this test, a significant number of pins was sheared-off, particularly in those specimens featuring an undercut spike geometry. The number of sheared spikes per specimen is therefore presented in Table 5. Among both investigated metals, a max. number of broken pins was found for the titanium samples. Particularly, grit blasted reinforcements where an average of 19.5 sheared-off pins per specimen was determined. Also in physically pretreated sheets, a considerable number of broken spikes was documented, especially for those featuring an undercut geometry with an average of 16.2 sheared-off spikes per single specimen. Obviously, for such geometry a greater amount of sheared spikes was expected to be encountered, even for the SAE 304 batches. However, this number was never as high as for the titanium counterparts. In contrast, among straight stainless steel configurations, only exceptionally some broken pin was found (Al_2O_3 treated reinforcements).

Table 5- average measured deformation (dimensions in µm) and nr. of sheared-off spikes post pin shear-out failure.

		straight								arrowhead			
		SAE 304				Ti 15-3				SAE 304		Ti 15-3	
		GB	HF/ $HN0_3$	La	RA	GB	Turco	La	RA	La	RA	La	RA
def. (µm)	$\overrightarrow{\Delta x}$	2089	1515	1545	1161	1873	1518	1644	1357	2051	1993	1510	1373
	$std(x)$	81	22	66	46	127	35	62	188	61	121	40.1	87.3
n° sheared-off spikes	$\overline{n}$	0.6	0.0	0.0	0.0	19.5	3.8	7.0	1.2	10.0	5.3	16.2	7.8
	upper dev.	0.6	0.0	0.0	0.0	2.5	3.3	8.0	0.8	5.0	1.8	3.8	2.3
	lower dev.	0.6	0.0	0.0	0.0	4.5	2.8	7.0	1.2	2.0	3.3	7.2	1.8

6.3.4 *Max. force vs. energy absorption*

Maximum bridging forces applied and energy absorption capacity derived from the force-displacement curves were found to agree well. These two parameters can be correlated for all configurations as quantified in Fig. 54.

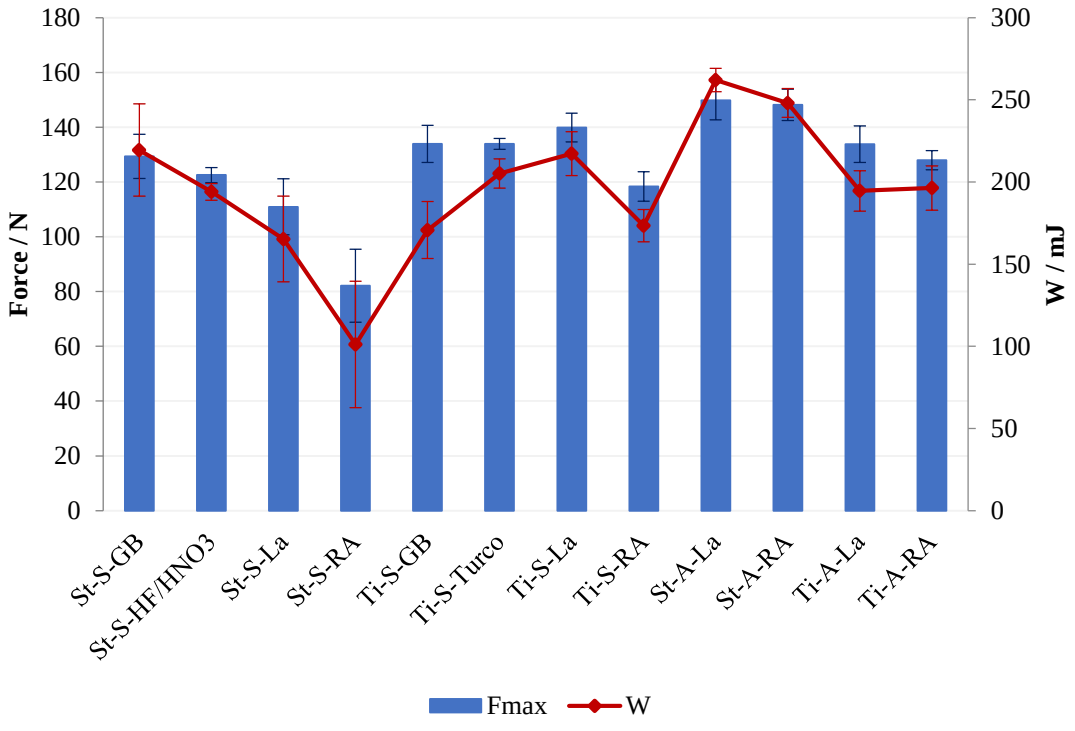

Fig. 54- Max. force and energy absorption for mixed-mode I/II test.

As shown in Fig. 54, titanium straight surfaces show in general greater energy absorption capabilities when compared to the stainless steel analogous reinforcements due to slightly greater maximum bridging forces. However, grit blasted straight surfaces do not follow this trend as SAE 304 configurations display larger areas under their respective plots and consequently higher residual deformations. In fact, among all investigated straight configurations, this is the one revealing the best performance with greater levels of energy

released against further crack transversal opening (219.4 mJ ± 28.1). Since maximum bridging forces are actually lower than those provided by the titanium counterparts (129.34 N ± 6.82 vs. 133.91 N ± 6.82), this is probably due to a more extended second stage and progressive third stage documented for the SAE 304 spikes. Obviously, a third vertical stage (titanium Al_2O_3 pretreated sheets) where forces decrease rapidly to zero does not contribute for an enlarged area under its force-displacement plot.

Among the straight Ti 15-3 batches, the amount of absorbed energy was maximal for the physically pretreated spikes (217.3 mJ ± 13.3) and slightly higher than for those treated by means of wet-chemical processes (205.2 mJ ± 8.9), due to modest superior bearing loads (139.9 N ± 5.2 vs. 133.9 N ± 2.0). Even though maximum closure forces were similar for the grit blasted surfaces (133.9 N ± 6.82), this surface pretreatment resulted in very little energy dissipation, even below release agent treated batches (170.7 mJ ± 17.4 against 173.4 mJ ± 9.9). Once again, this can be explained by the little resistance against further crack growth exhibited by these spikes during the previously mentioned third stage.

SAE 304 straight reinforced configurations revealed a more solid correlation between dissipated energy, maximum sustained loads and residual plasticization. This is probably due to the fact that for those specimens, almost no spike was sheared-off with the laminate sliding along the entire length of the pin throughout the test, as opposed to what happened with the titanium configurations. Slightly lower forces than those required for the grit blasted pins were needed to pull-out the acid etched spikes from inside the laminate (122.5 N ± 2.) which resulted in less absorbed energy (194.0 mJ ± 5.1). Even though bearing capacity load of laser structured counterparts is even lower (110.9 N ± 10.2), a more convex shaped third stage curve observed for these batches reflected in slightly higher values of residual plasticization.

Contrary to the registered observations for the straight reinforcements, stainless steel reinforcements featuring an undercut geometry remarkably outperformed those made of a titanium alloy. The greater levels of energy absorption (1.35 times higher) due to higher maximum closure forces and more importantly larger endured strains (1.5 times higher), proved the superiority of the arrowhead SAE 304 reinforcements over the titanium counterparts (laser pretreated surfaces). Also for this geometry, physically pretreated spikes were expected to show a much more efficient response against crack growth than those treated with a release agent coat. However, the difference was minimal for both materials. As shown in Fig. 54, Ti 15-3 release agent pretreated configurations reveal higher levels of energy absorption than the nano-structured surfaces (196.4 mJ±13.4 vs. 194.5 mJ ± 12.32). Given the same surface morphology, SAE 304 reinforcements with an arrowhead pin shape revealed enhanced levels of energy dissipation of 2.5 times (release agent pretreated pins) or 1.6 times (laser irradiation) when compared to the straight geometry. On the other hand, no extraordinary improvements were accomplished for the titanium spikes when considering an undercut geometry rather than a straight one. In fact, for those surfaces that were pretreated by laser irradiation, a remarkable deterioration of the performance was verified when using arrowhead pinned reinforcements (133.8 N ± 6.6 and 194.53 mJ ± 12.3).

6.3.5 Discussion

Experimental mixed-mode I/II results suggest that the mechanics by which these particular metallic reinforcements resist against crack sliding are highly dependent on the material properties of the reinforcement, particularly strain to failure, stiffness and yield and shear strength. Also, pin's geometry and applied surface pretreatment seems to have a distinct impact on the failure behaviour of the two investigated reinforcements' materials. Still, a generic bridging law composed by three distinct stages, where different energy absorbing mechanisms are involved, can be defined as depicted in Fig. 55.

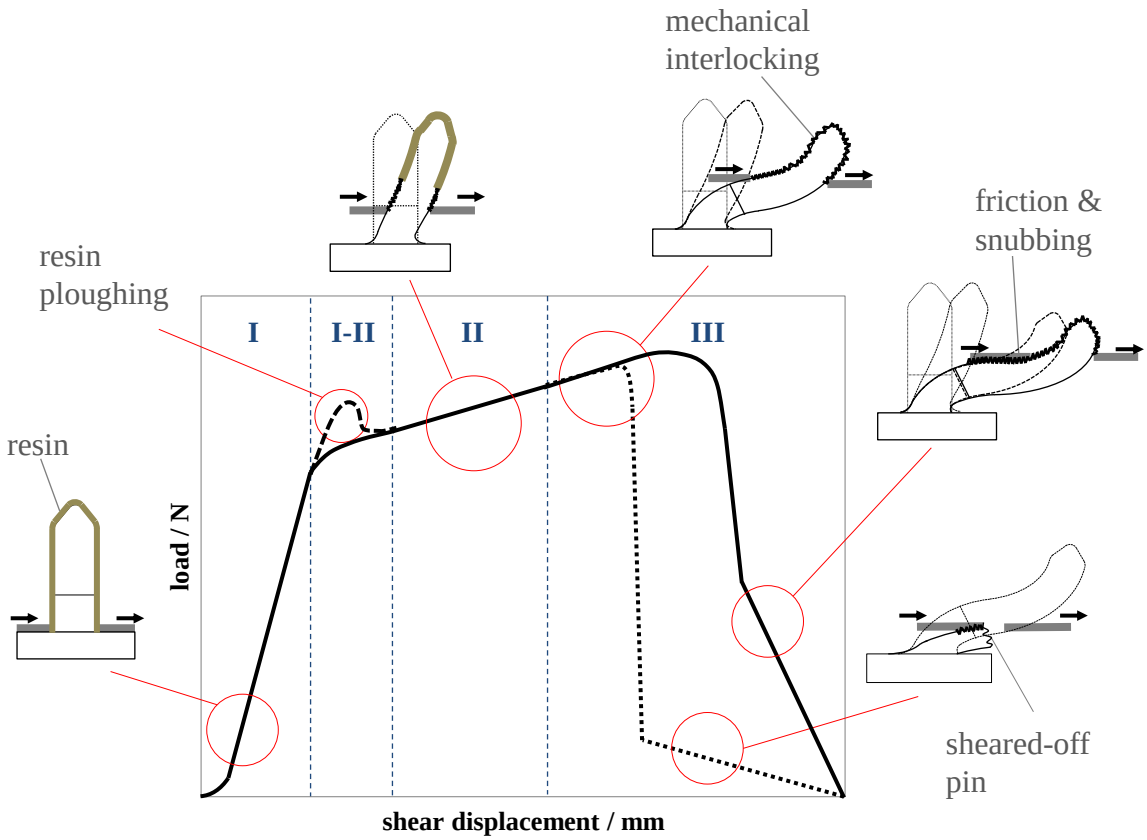

Fig. 55- Mixed-mode I/II shear-out generic bridgign law.

As described in Fig. 55, the fully bonded pin at the beginning of the first linear stage bends around its root and stretches along its displacement axis by elastic deformation only. As opposed to what happened for mode I loading conditions, no discontinuity (representing adhesion failure onset) was detected during this stage of the shear loaded spikes. However, adhesion failure is also expected to start somewhere around this stage as even though forces develop mainly at a linear rate with the associated displacement, a slight continuous slope drop from certain point onwards was observable for most investigated configurations. The non-detection (audible or through a curve discontinuity) can be explained by the fact that more complex energy absorbing mechanisms are involved for the pin shear-out process. In the previous tensile test, as soon as a small crack around the pin root emerged, opening displacement expanded rapidly without almost no additional force increase (observed discontinuity during the first stage of the force-displacement plots) due to the conversion of an adhesive zone to a less resistant frictional region. In this test, this does not necessarily happen as the fast transversal displacement of the laminate after debonding initiation is constrained by the orthogonal pin disposition “on the crack’s growth path”. In fact, this phenomenon as well as “ploughing” and “snubbing” effects that will be addressed further below represent the main differences between the pin’s response to pull- and shear-out loading conditions.

As it was the case for multi-pin pull-out tests, overall specimens’ stiffness at this first stage seems to be determined by adhesion and material properties (CTE). Despite the higher elasticity presented in Table 1, titanium reinforced specimens were shown to be stiffer at this stage than those featuring stainless steel spikes. This is most probably because SAE 304 configurations are exposed to higher thermal residual induced stresses after curing cycle. In fact, force-displacement curves of the fully bonded stainless steel spikes, right at the beginning of this stage are initiated at the same or even with a greater slope than the correspondent Ti 15-3

batches. However, as soon as the pin starts to debond from the neighbouring resin, a larger gap between pin and laminate exists as a consequence of the higher CTE values presented by this material (Table 1). Obviously, this is then translated into lower coefficients of friction between the debonded SAE 304 pin part and surrounding resin and therefore less inclined curves at this stage. Particularly, release agent straight pretreated configurations support this assumption since no special adhesion features exist; a reduced contact area due to higher residual post-curing stresses for the SAE batches resulted in lower frictional forces and therefore least amount of absorbed energy (see Fig. 49).

To the above mentioned first stage succeeds a transitional I-II section where force-displacement curves show a high scatter of their shape even within the same configuration (see APPENDICES C and D). This phase is believed to represent the elasto-plastic threshold, with pins deforming plastically from that point onwards. For some specimens, a progressive curve's slope drop until its stabilization at second stage entry was documented (solid line in Fig. 55). For others, bridging forces kept growing at the initiated rate (stage I), followed by almost a sudden extensive transversal crack displacement, represented by a "shoulder"-like shaped curve until entering the subsequent plasticization stage (thick dashed line in Fig. 55). This dispersion can, in fact, be explained by appealing to Fig. 56. Indeed, during pin insertion process in the autoclave, voids are formed where the fibres of the not entirely cured pre-preg have been pushed aside to accommodate the spikes. Supposedly, these cavities are then filled with resin during the curing cycle [24]. However, as shown in Fig. 56 a), part of these voids remain empty because the epoxy resin gelled during curing, before all cavities have been filled [47]. This way, it is believed that a progressive I-II elasto-plastic transition verified for some specimens happens because a considerable amount of air exists around the pins as shown in Fig. 56 a), so there is little resistance (by the resin) to the pins' continuous deformation motion which is accompanied by a gradual crushing of the resin (Fig. 56 c)). On the other hand, for those specimens whose load-displacement curves show a typical "S" transitional shaped curve, it is suggested that a greater amount of resin is surrounding the contour of the pins as in Fig. 56 b); as soon as bridging loads are high enough for the pin to start plasticizing, the adjacent resin obstructs its motion (with forces further increasing) until induced stresses at the interface are high enough to provoke fragmentation of a relatively large portion of resin (Fig. 56 d)). This phenomenon is similar to the "ploughing" effect, first detected by Treiber *et al.* in [42] during single-tuft shear-out experiments. Once resin ploughing occurs, the pin is again free to deform. Since induced stresses are generally high enough for the pin to begin to deform plastically, curve characteristics enter the following second stage.

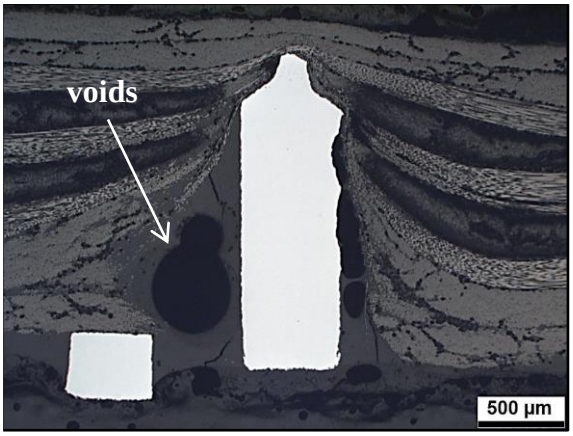

(a) post-curing micrograph (large amount of pores surrounding the pin)

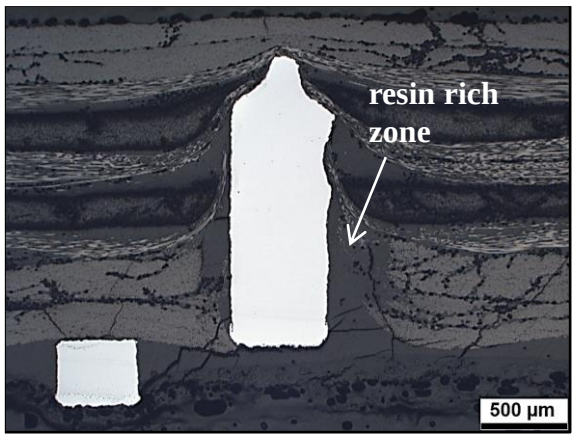

(b) post-curing micrograph (resin agglomerations)

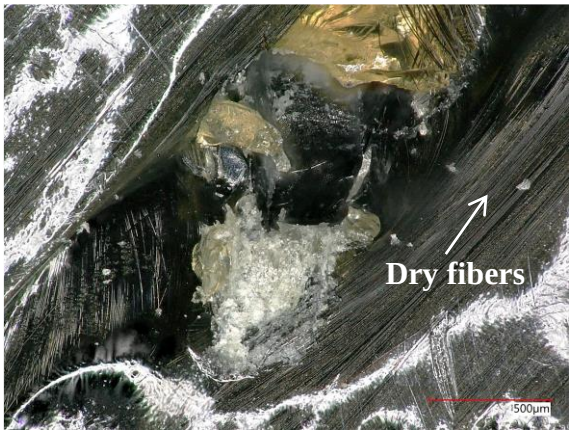

(c) post failure light microscopy top view of CFRP laminate (dry fibres suggest continuous ploughing)

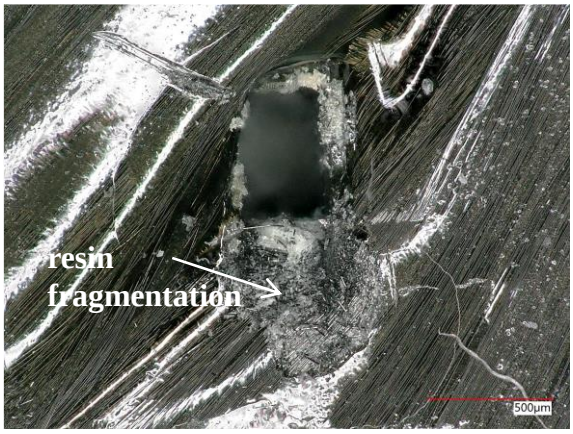

(d) post failure light microscopy top view of CFRP laminate (resin fragmentation indicates sudden "ploughing")

Fig. 56- Micrographs of random straight pins after curing cycle [29] and post-failure CFRP fracture surfaces [3].

Post total adhesion failure at second stage exit, all configurations enter the consecutive third stage with forces still increase slightly in a non-linear style due to a mechanical interlocking between the debonded pin's rough surface and neighboring fibres/resin. For some configurations (straight grit blasted and arrowhead laser pretreated Ti 15-3 reinforcements), induced stresses during this non-linear force increase are high enough to shear almost all their pins off, represented by the following sharp force drop (thin dotted line in Fig. 55). For those specimens, after pins have been sheared-off, a final section where forces evolve in a more horizontal manner can be distinguished; this is due to the friction between laminate's crack face and the contour of the broken pins (see bottom right pin sketch in Fig. 55). Others bear all applied loads with few pins (arrowhead SAE 304 and remaining Ti 15-3 configurations) or no pin (straight SAE 304 configurations) being sheared-off until complete pin pull-out. For those, as soon as bridging forces reach their max. value, the interlocked interface yields and sliding of the laminate along the pin begins with forces decreasing continuously and with frictional pull-out as the only energy dissipating mechanism acting against further crack propagation. As soon as distance between crack faces is large enough for pin "full-length" pull-out, the process remains mechanically. This can only be attributed to the so-called "snubbing" effect, first detected by Cartié et al. in [31, 37], during CF and titanium rods shear-out experiments. As explained before, this phenomenon represents an enhancement of frictional forces after a

considerable deflection of the pin's length into the laminate's crack face due to an increased contact pressure.

For this specific test, the applied surface pretreatment seems to have a distinct impact on the bridging behaviour of the two investigated reinforcement's materials. Considering measured areas under the load-displacement curves, recorded levels of bearing loads and also the ratio between both, roughness scale created by the surface pretreatment is suggested to determine the performance of the SAE 304 spikes. As referred before, among all investigated pretreatments, an Al_20_3 blasting surface treatment creates the larger morphology scale. As a consequence, higher coefficients of friction post pin adhesion failure initiation are present for this configuration. This is then translated into a more inclined and extended second stage of the bridging laws, as shown in Fig. 57 a). Also, an enhanced mechanical interlocking between the debonded pin part and surrounding fibres/resin of the laminate that delays laminate sliding onset is achieved when a grit blasting surface pretreatment is applied due to a pin's surface macro-roughness. This is also confirmed through the higher load bearing capabilities documented for these specimens (Fig. 57 a)). On the other hand, as mentioned in chapter 6.3.5, a physically transformed surface structure on the nano-scale results in a smooth debonded interface. A poor resistance against sliding initiation post debonding onset is therefore suggested to explain the barely visible second and the short third stage with reduced bearing load capabilities observed for the SAE 304 laser irradiated pins (Fig. 57 a)).

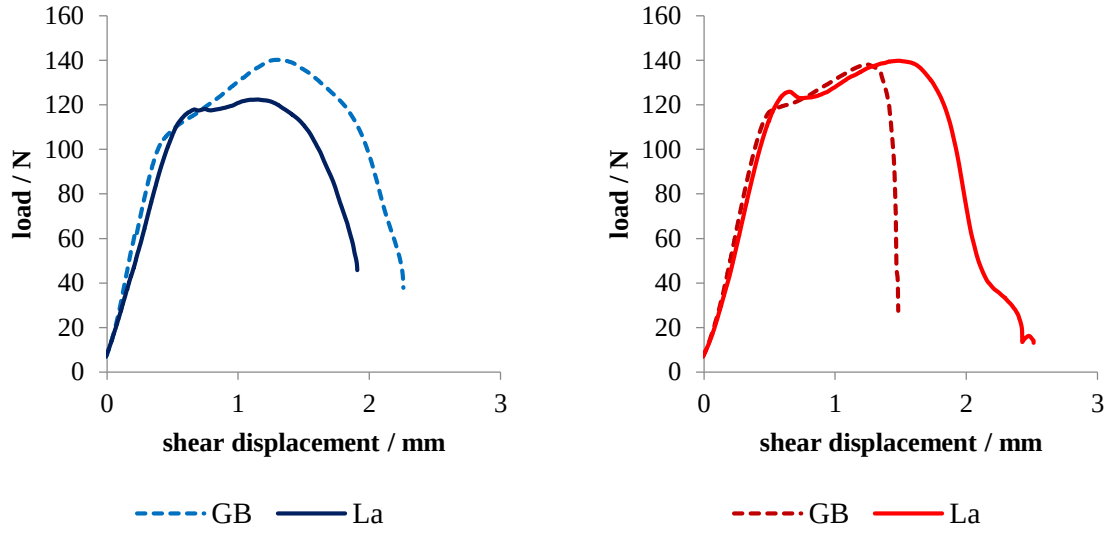

(a) SAE 304 spikes

(b) Ti 15-3 spikes

Fig. 57- Grit-blasted vs. laser pretreated straight spikes (mixed-mode I/II).

Following the same line of thought, one would expect for the titanium mechanically pretreated batches to exhibit an even better performance in terms of energy absorption capacity as higher frictional features are present for this material due to lower residual induced stresses post-curing cycle. However, this was not the case as many of their spikes failed even before pins' frictional pull-out phase. Still, applied surface pretreatment seems to play an important role on the performance of reinforcements made from this alloy. Even though load bearing capabilities of laser pretreated spikes are slightly better than those of Al_2O_3 treated surfaces (Fig. 57 b)), this configuration does not see as many of its spikes being sheared-off during testing. No solid explanation was found for this fact. However, one can speculate that this is related either with the type or distribution of pretreatment induced residual stresses. In fact, tension and compression residual stresses are induced on the reinforcements' surface when a laser and a Al_2O_3 blasting surface pretreatment is applied, respectively. Thus, while tensile

stresses induced by a laser treatment (Fig. 58 a)) relieves the state of tension on the surface of the pin that is subjected to shear stresses, grit-blasting induced compression residual stresses (Fig. 58 b)) are added to the applied loads during testing. As a consequence, shear strength of grit-blasted spikes is more quickly attained. This explains why despite level of applied loads during testing are similar for the two pretreatments, a greater number of broken pins is documented when a mechanical treatment is applied, which is then obviously translated into smaller amounts of absorbed energy due to absence of a stage of friction.

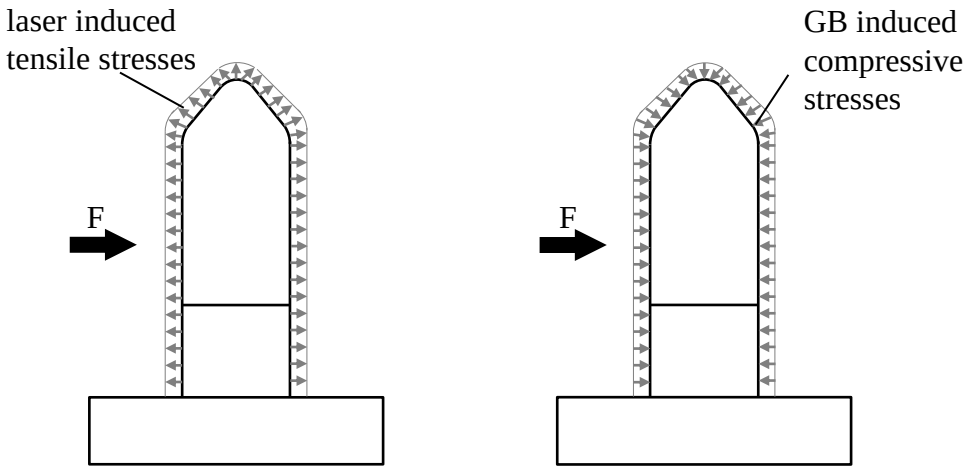

(a) laser irradiation induced tensile stresses (against the load)

(b) grit-blasting compressive induced stresses (load direction)

Fig. 58- Laser pretreatment (a) and grit-blasting (b) induced residual stresses

The alternative approach to explain the scatter in the documented number of sheared-off spikes among Ti 15-3 reinforcements is related with the distribution of the same above mentioned residual stresses. As described in chapter 5.2, a distinct roughness scale is created by the different investigated surface pretreatments (Fig. 59). Indeed, nano-cavities or -protrusions created by a laser pretreatment not only are smaller but are also organized in a more structured way (pulsed structure; see Fig. 59 a)) than those resulting from a coarse grit blasting treatment (Fig. 59 b)). Seeing these irregularities as local stress concentration spots, the overall end notch factor on a critical spot of a mechanically pretreated reinforcement sheet is obviously higher. This is then translated into lower bridging forces required for shearing-off the first pin. After first pin breakage, induced stresses previously withstood by this, have to be redistributed among the remaining spikes resulting in abrupt shearing of these, represented by the sharp force drop in Fig. 57. In contrast, the more organized and smaller pulsed structure (Fig. 59 a)) created by a more accurate laser irradiation surface pretreatment allows the applied loads to be evenly distributed among all pins and therefore higher forces being bore. Eventually, during frictional pull-out stage (load decrease), some spikes are progressively sheared-off due to imposed large deformation levels at this stage. Even though forces decrease during pins' frictional pull-out, this does not mean that induced stresses are getting lower as the pin is being stretch and therefore its cross sectional area being reduced.

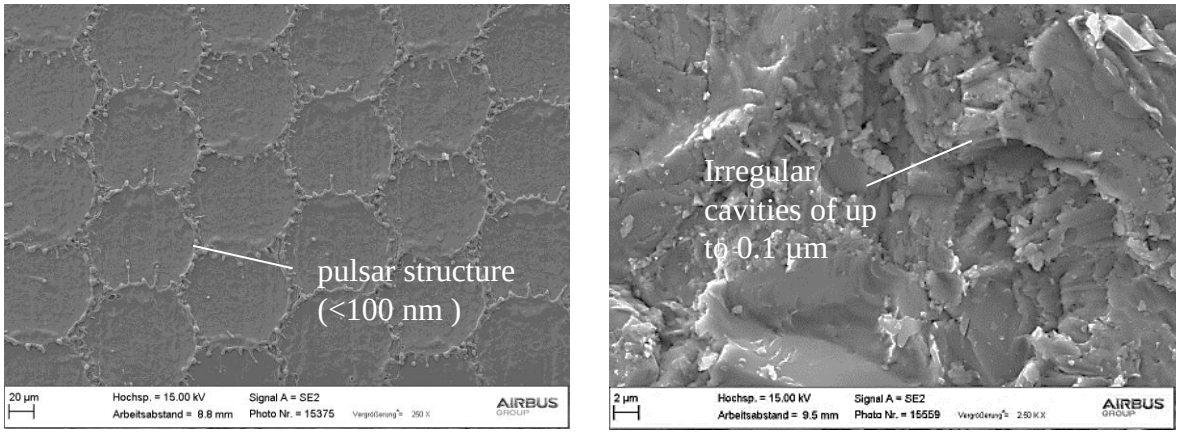

(a) pulsed-structured resulting from a laser pretreatment (regular nano-cavities)

(b) irregular structure on a macro-scale resulting from a grit blasting pretreatment

Fig. 59- Laser (a) and grit-blasting (b) typical induced surface morphologies.

As opposed to what happened for the straight configurations, energy absorption capacity of arrowhead stainless steel reinforcements is remarkably greater than that revealed by titanium spikes. Larger elongations to failure of the SAE 304 reinforcements resulted in fewer sheared-off spikes and consequently a more gradual frictional third stage. As pull-out of the straight SAE 304 pins from inside the laminate occurred before induced stresses reached the reinforcement's material shear strength, consideration of an undercut geometry instead was proven to be worthwhile with more than 1.8 and 2.4 documented maximum endured forces and energy absorption capacities, respectively. On the other hand, the use of an undercut geometry rather than a straight one for a Ti 15-3 reinforcement was shown to be counterproductive for this test. Shear strength or maximum elongation of many straight titanium spikes is attained even before the mechanical interlocking effect has any considerable influence. As a consequence, levels of maximum force and work done against pull-out are approximately the same or even lower when an undercut geometry is considered.

7 Analytical investigation

7.1 Pin's micromechanics

For both mode I and mixed-mode I/II loading conditions, it was postulated that once induced stresses at the pin's critical cross section reach the material's yield strength, plastic deformation starts at this section, at the beginning of the second stage of the derived bridging laws. To confirm this statement, a simple microstructural-mechanical approach was considered. The aim is to verify how much of a vertical (mode I) or a lateral (mixed-mode I/II) force at the top or at the side of the pin, respectively, is required to trigger plasticization at its critical section.

7.1.1 Mode I

Side view post failure analysis (Fig. 43) suggests that higher stresses are induced at the bottom of the pin. Thus, equivalent stresses induced by a force F at the top of the pin were calculated for a section at the pin's bottom radius as depicted in Fig. 60.

A section (A-A), that is inclined with an angle of $(\pi/2)-\theta$ radians from the pin's root, is subjected to flexural (σ_f), normal (σ_n) and also transversal shear stresses (τ_{xy}) as depicted in Fig. 61. Normal resulting stresses to the section plane can be expressed as

$$\sigma_z = \sigma_f + \sigma_n \tag{3.1}$$

where,

$$\sigma_f = -\frac{My}{I_x} \tag{3.2}$$

$$\sigma_n = \frac{F\cos\theta}{A} \tag{3.3}$$

in which A is the cross-sectional area, M is the induced bending moment and I_x is the moment of inertia with respect to the x-axis, given by

$$A = bh \tag{3.4}$$

$$M = Fl \tag{3.5}$$

$$I_x = \frac{bh^3}{12} \tag{3.6}$$

b and h are the width and length of the cross section respectively, and l is the horizontal distance between force F and the centre of gravity calculated as follows

$$l = \left(R + \frac{h}{2}\right)(1-\cos\theta) \tag{3.7}$$

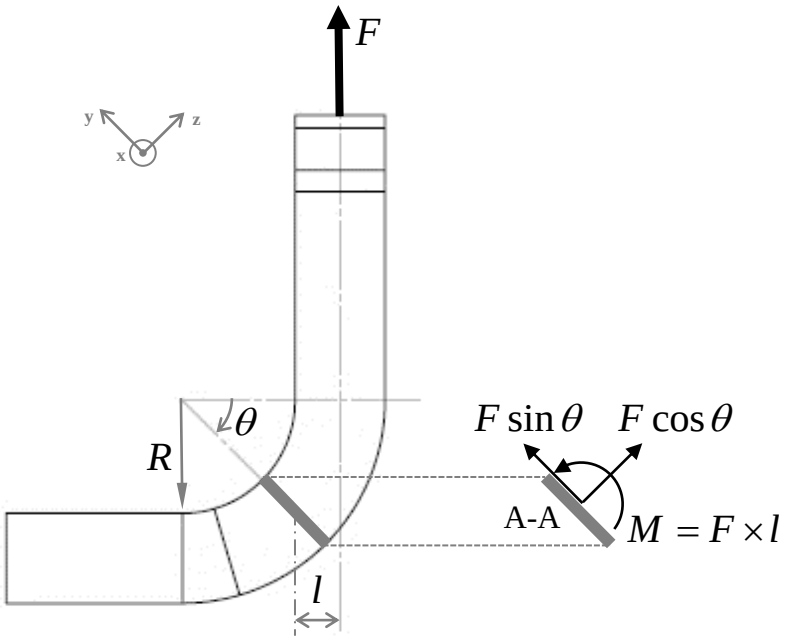

Fig. 60- Schematic of a pin subjected to tensile loads and induced forces in a section of the pin's bottom radius.

Transversal shear stresses at the section plan are expressed by

$$\tau_{xy} = \frac{FQ_y \sin\theta}{I_x b} \tag{3.8}$$

in which Q is the first moment of area with respect to the y-axis, defined as

$$Q = \frac{1}{2}\left[\left(\frac{h}{2}\right)^2 - y^2\right]b \tag{3.9}$$

Considering von Mises' criterion as the yield criterion we have

$$\sigma_{VM} = \sqrt{\sigma_z^2 + 3\tau_{xy}^2} \tag{3.10}$$

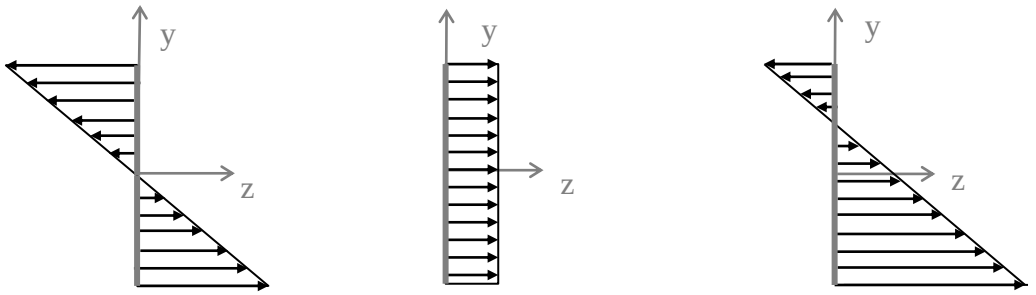

$$\sigma_f = -\frac{M \times y}{I_x} \qquad \sigma_n = \frac{F\cos\theta}{\mathrm{A}} \qquad \sigma_z = \sigma_f + \sigma_n$$

(a) flexural induced stresses (b) normal induced stresses (c) resulting normal stresses

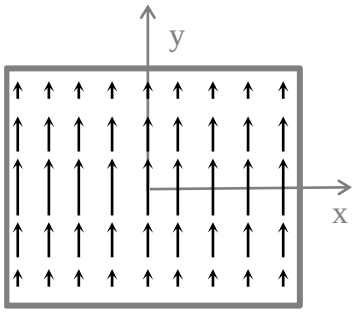

$$\tau_{xy} = \frac{FQ_y \sin\theta}{I_x b}$$

(c) transversal shear induced stresses

Fig. 61- Resulting induced stresses in a section at the pin's bottom radius.

Equation (3.10) is then depending on the angle θ and on the position y. Fig. 62 a) illustrates the evolution of von Mises' stress (normalized) for a point y of a section inclined with a $(\pi/2)-\theta$ radians angle from the pin's root. According to Fig. 62 a), the critical section of the pin's structure is located at the top and bottom edges $(y=\pm h/2)$ of the pin's root $(\theta=\pi/2)$. This was also observed during post failure light microscopy analysis where a well pronounced plasticization at the pin's root was detected for some configurations (Fig. 43 b)). Since at these sites $(y=\pm h/2)$ there are no shear stresses, von Mises' stress can be rewritten as follows

$$\sigma_{VM} = \sigma_z \tag{3.11}$$

By introducing into equations (3.1)-(3.9) the appropriate geometrical dimensions of the pin, it is possible to express von Mises' stress at this location as a function of the applied force F as follows

$$\sigma_{VM} = 26.25 A^* F \tag{3.12}$$

in which,

$$A^* = 1\left[\frac{1}{\mathrm{mm}^2}\right] \tag{3.13}$$

According to Table 1, yield strength of both metals considered as reinforcement elements in the current investigation is

$$\begin{aligned} \sigma_y^{SAE304} &= 200 \text{ MPa} \\ \sigma_y^{Ti15-3} &= 1050 \text{ MPa} \end{aligned} \tag{3.14}$$

Finally, replacing von Mises' stress by the yield strength of the reinforcement material, it is possible to calculate the force F that provokes plastic deformation onset at the pin's root

$$\begin{aligned} F_y^{SAE304} &= \frac{\sigma_y^{SAE304}}{26.25A^*} = \frac{200}{26.25} = 7.62\ N \\ F_y^{Ti15\text{-}3} &= \frac{\sigma_y^{Ti15\text{-}3}}{26.25A^*} = \frac{1050}{26.25} = 40\ N \end{aligned} \tag{3.15}$$

The obtained value of minimal force necessary to trigger plasticization of Ti 15-3 spikes agrees well with the load-displacement curves of Fig. 38. However, for stainless steel reinforcements, a considerable deviation between the calculated force and observed loads at the beginning of the second stage of the bridging law is evident (7.62 N vs. approximately 40 N; see Fig. 38). This divergence most probably results from the mechanical forming (stamping) process selected for the manufacture of the metallic inserts. In fact, this cold forming process implies strain hardening of the metallic spikes; work hardening is a phenomenon that occurs when the metal is strained beyond its limit of elasticity, leading to a stronger and harder material after load release. This hardening process is schematically depicted in Fig. 62 b) for both materials. Assuming that during the conformation process of the metallic pins, loads were applied up to close to their ultimate resistance, the new yield strength values are, according to Table 1

$$\begin{aligned} \sigma_{y_2}^{SAE304} &= 700 \text{ MPa} \\ \sigma_{y_2}^{Ti15-3} &= 1060 \text{ MPa} \end{aligned} \tag{3.16}$$

Yield strength of the cold formed SAE 304 pins is now more than 3 times higher than before the conformation process. Thus, higher levels of force are required to trigger pins' plastic deformation. On the other hand, the bending process of titanium spikes did not impact their hardness. This happens because the plastic deformation threshold of this alloy is significantly smaller than that exhibited by a stainless steel material. As a consequence, yield strength of titanium reinforcements after bending process remains almost unchanged. By replacing now the equivalent stress by the new yield strength values in equation (3.12), it is possible to recalculate the force F that triggers spike's plasticization

$$\begin{aligned} F_{y_2}^{SAE304} &= \frac{\sigma_{y_2}^{SAE304}}{26.25A^*} = \frac{700}{26.25} = 26.67\ N \\ F_{y_2}^{Ti15\text{-}3} &= \frac{\sigma_{y_2}^{Ti15\text{-}3}}{26.25A^*} = \frac{1060}{26.25} = 40.38\ N \end{aligned} \tag{3.17}$$

As shown by the load-displacement curves of Fig. 38, bridging forces of SAE 304 batches at stage two enter can still be slightly higher than those calculated in equation (3.17). This is most probably because the yield strength of the hardened pin can still be higher than that considered in equation (3.16). In theory, strain hardening of a metallic material is limited by its tensile

strength. In practice, this does not happen as the yield strength of the hardened metal often exceeds its original tensile strength (before hardening).

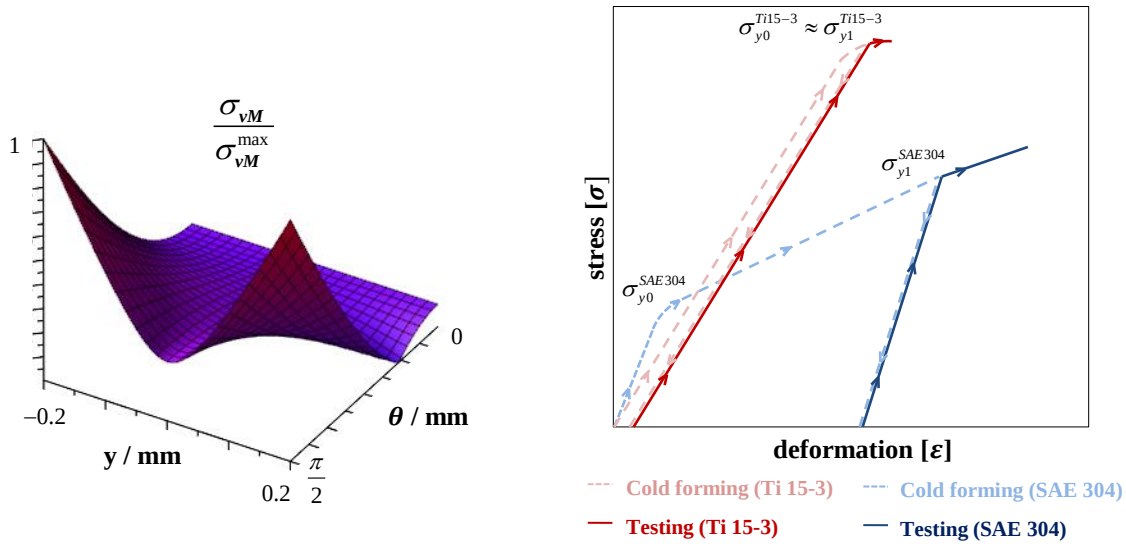

(a) von Mises' equivalent stress (normalized) for $0 \leq \theta \leq \pi/2$ and $-h/2 \leq y \leq h/2$

(b) strain hardening of a SAE 304 and Ti 15-3 spike due to bending process

Fig. 62- Von Mises' stress (a) and strain hardening due to cold-forming manufacture process (b).

7.1.2 Mixed-mode I/II

To estimate the value of the lateral force that provokes plasticization onset at the critical section of a pin subjected to mixed-mode I/II loading conditions, the reasoning presented in the previous chapter is adapted. The goal is to verify if this force matches the level of bridging forces of the load-displacement curves presented in chapter 6.3.2, at stage two entering (plasticization stage).

Front view failure analysis of those specimens in which some pins where sheared-off suggests that higher stresses are induced at the bottom of the pin, particularly at its root. To confirm this, two different sections, namely section T-T and B-B, were considered as depicted in Fig. 63.

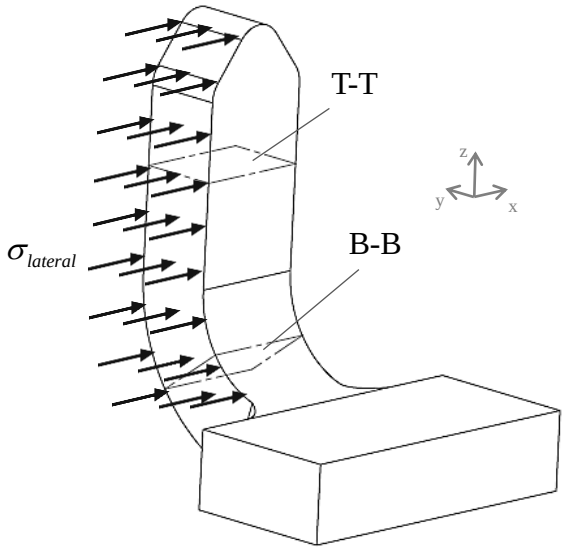

Fig. 63- Schematic of a pin subjected to shear loads with considered sections (T-T and B-B).

When a force F is applied at spike's lateral face, as in Fig. 63, section T-T is simply subjected to transversal shear stresses (Fig. 64 a)), expressed by

$$\tau_{zx} = \frac{FQ_x}{I_y b} \tag{4.1}$$

where Q_x is the first moment of area in relation to the x-axis and I_y is the moment of inertia with respect to the y-axis, given by

$$\begin{aligned} Q_x &= \frac{1}{2}\left[\left(\frac{h}{2}\right)^2 - x^2\right] b \\ I_y &= \frac{bh^3}{12} \end{aligned} \tag{4.2}$$

in which b and h are the width and length of section T-T, respectively. On the other hand, a section B-B at the pin's radius is subjected not only to transversal shear stresses (τ_{xz}) but also normal stresses (σ_y) as depicted in Fig. 64 b), that can be written as follows

$$\tau_{zx} = \frac{FQ_x}{I_z b} \tag{4.3}$$

$$\sigma_y = \frac{Mx}{I_z} \tag{4.4}$$

M and I_z are the flexural moment induced by the force F and the moment of inertia with respect to the z-axis, respectively, defined as in equation (4.5)

$$\begin{aligned} M &= Fl \\ I_z &= \frac{bh^3}{12} \end{aligned} \tag{4.5}$$

where l is the horizontal distance between force F and the centre of gravity of section B-B.

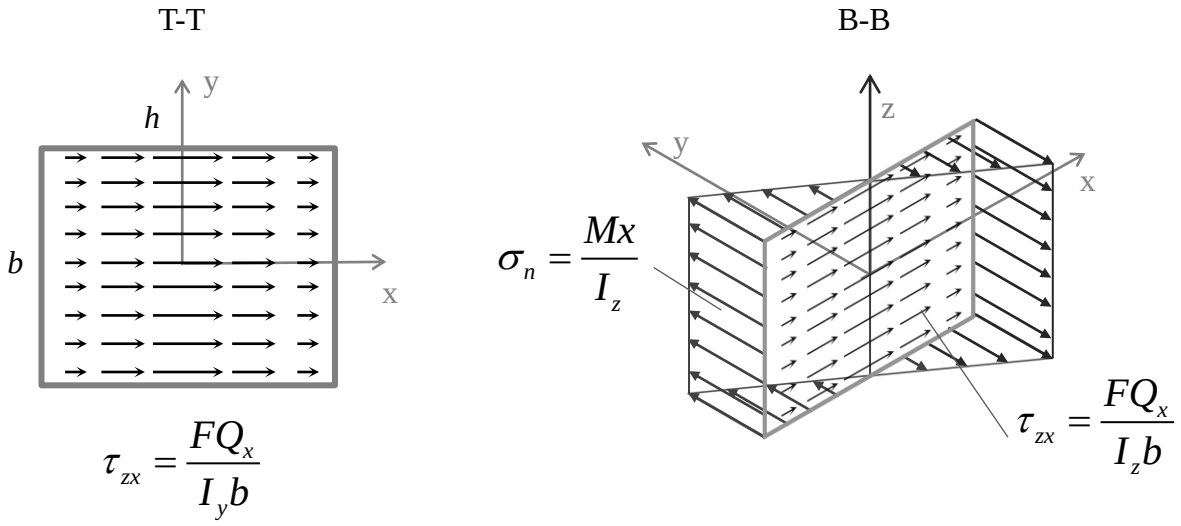

(a) resulting stresses at section T-T (only shear stresses)

(b) resulting stresses at section B-B (shear and normal stresses)

Fig. 64- Resulting stresses at section T-T (a) and B-B (b)

As the moment of inertia with respect to z-axis in section T-T is equal to that of Section B-B, shear stresses at the two distinct sections are the same. Since section B-B is furthermore subjected to normal stresses provoked by the flexural moment M, state of tension at this section is obviously more severe. Moreover, the induced moment is maximum for the farthest section from the application point of force F. Hence, it can be concluded that the critical section where plastic deformation starts is located at the pin's root, confirming observations during post-failure light microscopy analysis.

Considering, once again, von Mises' criterion as the yield criterion, we have

$$\sigma_{VM} = \sqrt{\sigma_y^2 + 3\tau_{xz}^2} \tag{4.6}$$

By substituting into equations (4.2)-(4.5) the appropriate geometrical parameters of the pin, it is possible to express von Mises' equivalent stress as a function of the applied force F and the x-coordinate at the critical section as follows

$$\sigma_{VM} = F\sqrt{441B^* x^2 + 3\left(3.75 - 15C^* x^2\right)^2} \tag{4.7}$$

where,

$$\begin{aligned} B^* &= 1\left[\frac{\mathrm{N}^2}{\mathrm{mm}^6}\right] \\ C^* &= 1[\mathrm{N}] \end{aligned} \tag{4.8}$$

From equation (4.7), one can easily verify that stresses are higher at the lateral edges of the pin, *i.e.*, when $x = \pm h/2$. Von Mises' equivalent stress at this location can then be expressed as only a function of F as follows

$$\sigma_{VM} = 10.5D^* F \tag{4.9}$$

with,

$$D^* = 1\left[\frac{1}{\mathrm{mm}^2}\right] \tag{4.10}$$

By substituting von Mises' stress in equation (4.9) by the recalculated yield strength (after pin bending process) of the hardened pin (equation (3.16)), the force F that, in theory, triggers plasticization at its root is estimated as

$$\begin{aligned} F_y^{SAE304} &= \frac{\sigma_y^{SAE304}}{10.5D^*} = \frac{700}{10.5} = 66.7 \text{ N} \\ F_y^{Ti15-3} &= \frac{\sigma_y^{Ti15-3}}{10.5D^*} = \frac{1060}{10.5} = 101 \text{ N} \end{aligned} \tag{4.11}$$

Once again, calculated value of yield force for the titanium spikes agrees well with the observed values of bridging force at stage two entering (see Fig. 49). Yet, stainless steel derived plots can reveal load levels for plasticization onset that are slightly higher than that calculated in equation (4.11). This fact further supports the idea that was stated in the previous chapter *i.e.*, that the cold forming process results in a yield strength of the hardened spikes that is, in fact, greater than the original tensile strength of this material before hardening.

7.2 Thermal residual stresses

Mode I and mixed-mode I/II test results strongly indicate CTE to be one of the main factors that determines the difference in the mechanisms and amount of energy absorption between stainless steel and titanium reinforcements. In previous sections, it was suggested that the comparatively larger mismatch between CTE values of SAE 304 reinforcements and host laminate results in less contact between the debonded part of the pin and surrounding laminate, thus implicating a lower coefficient of friction. In this section, a simple macro-mechanical approach on the pin's scale is considered to assess and compare induced thermal residual stresses post-curing cycle.

Considering one single expanded pin and the fully cured surrounding laminate at the end of the co-curing cycle (around 180°C) as depicted in Fig. 65, two extreme boundary conditions can be distinguished. On the one hand, if the pin is free to shrink to its original shape (with the bonded laminate behaving ideally as a highly ductile material, *i.e.* opposing no constraint to pin's reshaping motion), its transversal strain is given by

$$\varepsilon_{free} = \alpha_{pin} \Delta T \tag{5.1}$$

where α_{pin} is the CTE of the spike's material and ΔT is the difference between maximum curing and room temperature, respectively.

The other extreme situation is to consider the surrounding composite laminate as a non-deformable material, thereby precluding pin's contraction. In this case, the pin is considered to be fully clamped around its contour and post cooling residual stresses at the pin-laminate interface can be written as

$$\sigma_{pin}^{residual} = E_{pin} \varepsilon_{free} \tag{5.2}$$

in which E_{pin} is the Young's modulus of the pin.

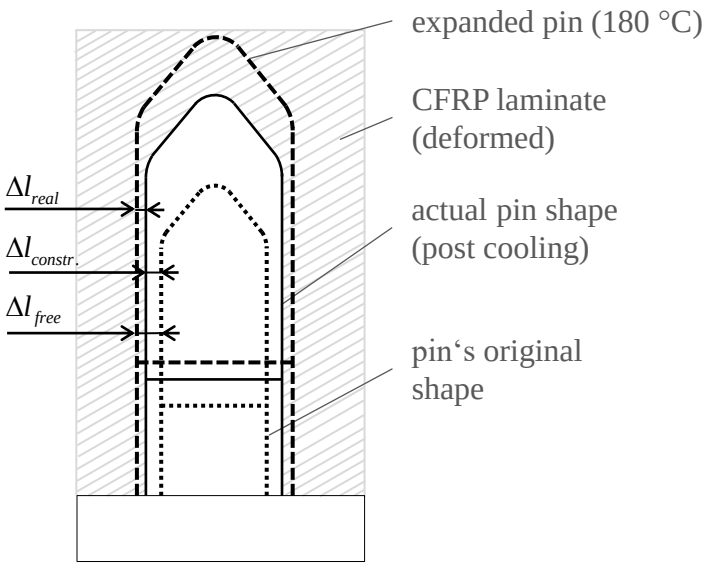

Fig. 65- Scheme of possible pin/resin deformation modes post curing cycle (during cooling).

For this model, an intermediate situation is considered. It is assumed that the pin and surrounding laminate are free to deform up to an equilibrium situation, *i.e.* until induced stresses in the pin's surface are equal to those at the resin's bonding interface. This can be written as

$$\sigma^{residual} = \sigma_{pin}^{residual} = \sigma_{CFRP}^{residual} \tag{5.3}$$

Under such scenario, induced residual thermal stresses at the pin's outer surface are given by

$$\sigma_{pin}^{residual} = E_{pin}\varepsilon_{const.} \tag{5.4}$$

where $\varepsilon_{constr.}$ is considered to be the amount of necessary strain that was left for the pin to contract back to its original shape, *i.e.*

$$\varepsilon_{constr.} = \varepsilon_{free} - \varepsilon_{real} \tag{5.5}$$

ε_{real} is the actual strain suffered by the spike and also by the CFRP at the bonding interface. It is important to point out that equation (5.5) is valid only when $\varepsilon_{real} = \Delta l_{real} / l_0$ is comparatively small. Thus, it is possible to write

$$\sigma_{pin}^{residual} = E_{pin}\left(\varepsilon_{free} - \varepsilon_{real}\right) \tag{5.6}$$

Composite laminate induced residual stresses due to the contraction of a fully bonded pin can be expressed as

$$\sigma_{CFRP}^{residual} = E_{CFRP}\varepsilon_{real} \tag{5.7}$$

in which E_{CFRP} is the Young's modulus of the CFRP laminate that shall be calculated through Classical Laminate Theory [73] or similar approach. According to equation (5.3), it is possible to match equations (5.6) and (5.7) as follows

$$\sigma^{residual} = E_{pin}\left(\varepsilon_{free} - \varepsilon_{real}\right) = E_{CFRP}\varepsilon_{real} \tag{5.8}$$

Solving equation (5.8) under consideration that $\varepsilon_{free} = \alpha_{pin}\Delta T$ (equation (5.1)), ε_{real} is expressed as

$$\varepsilon_{real} = \frac{E_{pin}\left(\alpha_{pin}\Delta T\right)}{E_{pin} + E_{CFRP}} \tag{5.9}$$

Finally, by combining equations (5.8) and (5.9) one obtains

$$\sigma_{residual} = \frac{E_{pin}\alpha_{pin}\Delta T}{E_{CFRP} + E_{pin}} E_{CFRP} \tag{5.10}$$

From equation (4.10), it can be easily verified that given the properties of the composite laminate, induced residual thermal stresses are dependent on the Young's modulus and CTE of the reinforcement material. Thus, considering the materials' properties given in Table 1, it can be concluded that residual stresses are generally higher when a SAE 304 material is used as the reinforcement element instead of a titanium 15-3 alloy.

7.3 Analytical approach for mode I delamination of z-reinforced laminates

7.3.1 Theoretical model

An analytical approach based on that model developed by Liu *et al.* [39] for z-pinned laminates (chapter 3.1.3) was adapted to predict the delamination behaviour of DCB laminates reinforced through the technology under investigation in this work.

As in the model developed for z-pinning, fracture energy method was used as the delamination criterion of the pre-cracked laminated beam. It is assumed that the crack divides the DCB reinforced laminate into two symmetric beams reinforced with r rows and c columns of pins as in Fig. 66. Applying Castigliano's theorem and according to equation (2.3), the strain energy release rate is

$$G_I = \frac{1}{2E_x I_x b}\frac{\partial}{\partial a}\left[\int_0^a M(x)^2\,dx\right] \tag{6.1}$$

where E_x is the Young's modulus and I_x is the moment of inertia of the laminated beam in relation to the *x*-axis. E_x is obtained, once again, through Classical Laminate Theory or similar, whereas I_x is calculated as in equation (3.6); b is the width of the beams and a is the delamination crack length.

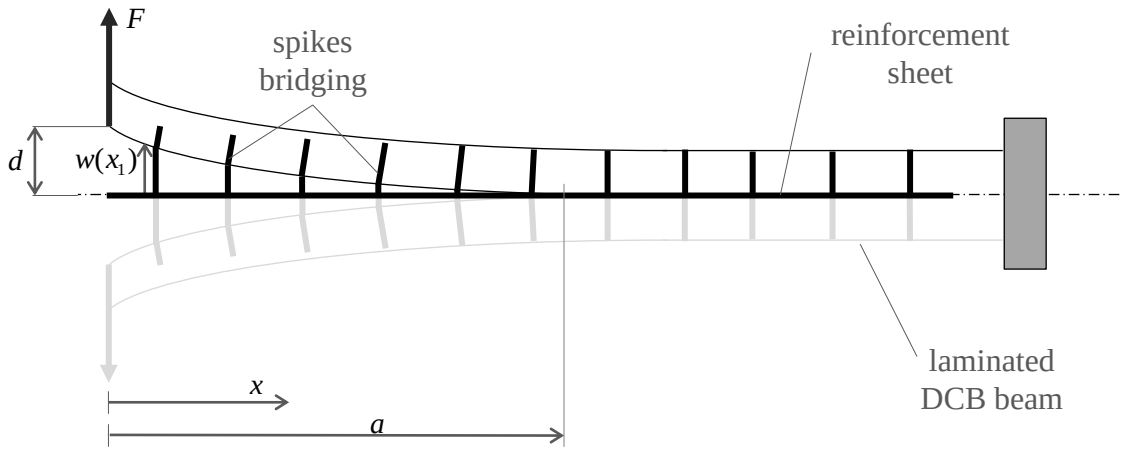

Fig. 66- Scheme of a DCB laminate reinforced with the integrated reinforcement structure considered in this investigation.

After the crack has passed the first column of pins, the bending moment $M(x)$ is not only dependent on the applied load at the beam's end (F) but also dependent on the bridging forces of the reinforcement's pins (P_i), as described in chapter 3.1.3. It can be expressed as follows

$$M(x) = Fx - \sum_{i=1}^{c} P_i (x - x_i) \tag{6.2}$$

where P_i and x_i are the bridging force and the location of the ith column of pins, respectively. Assuming that all pins of the same column provide the same level of closure forces, calculation of the bridging load P_i of the ith column of pins is made by multiplying the number of rows (r) by the bridging force P_s of a single spike. Bridging force of a single spike is obtained by introducing the measured deflection of the beam at the pin's location $(w(x_i))$ into its bridging law. From the generalized beam theory, the equation that expresses the deflection $w(x)$ of a bent beam at the location x is given by

$$E_x I_x \frac{\partial^2 w(x)}{\partial x} = M(x) = \begin{cases} Fx & (0 \le x \le x_1) \\ Fx - \sum_{j=1}^{i} P_j (x - x_j) & (x_i \le x \le x_{i+1}) \end{cases} \tag{6.3}$$

Equation (6.3) unveils the dependence of the deflection of the beam $w(x)$ on the bending moment M and thereby also on the closure forces provided by the spikes (P_j). Thus, it is mathematically difficult to obtain a closed-form analytical solution for equation (6.1). An iteration method was considered instead. In this approximate method, the applied displacement at the beam's end is added step by step. In the first step, no additional displacement is considered but a tiny increase on the crack's length, *i.e.*

$$\begin{aligned} d_1 &= d_0 \\ a_1 &= a_0 + da_0 \end{aligned} \tag{6.4}$$

As the displacement of the first pin is very small, its effect can be neglected. The solution of equation (6.3) can be written as follows:

$$EIw(x) = \begin{cases} \frac{1}{6} Fx^3 + Cx + E_x I_x d & (0 \le x \le x_1) \\ \frac{1}{6} Fx - \frac{1}{6} \sum_{j=1}^{i} P_j (x - x_j)^3 + Cx + E_x I_x d & (x_i \le x \le x_{i+1}) \end{cases} \tag{6.5}$$

in which,

$$C = -\frac{1}{2} Fa^2 + \sum_{j=1}^{c} \frac{1}{2} P_j \left(a - x_j\right)^2 \tag{6.6}$$

$$F = \frac{\sum_{j=1}^{c} P_j \left(a - x_j\right)^2 \left(2a + x_j\right) + 6E_x I_x d}{2a^3} \tag{6.7}$$

The displacement of the ith column of pins is then

$$w(x_i) = \frac{1}{EI} \left[\frac{Fx_i^3}{6} - \sum_{j=1}^{i-1} \frac{P_j}{6} \left(x_i - x_j\right)^3 + Cx_i + E_x I_x d \right] \tag{6.8}$$

By introducing the obtained displacement $w(x_i)$ into the measured bridging law, the bridging force of each column of pins (P_i) can be calculated. Adding the displacement step by step $(d = d + \Delta d)$ and using the solved bridging force (P_i), a new set of displacements $w(x_i)$ can be obtained. The above process is repeated until the energy release rate is large enough to enough to cause the delamination to grow, *i.e.*, when $G_I > G_{Ic}$.

7.3.2 Application of the model with measured bridging laws

For validation, the model described above was implemented with the measured bridging laws (chapter 6.2) under Maple 2015 environment and compared with the experimental results of a DCB testing campaign carried out in previous related investigations. In those tests, a continuous metallic carrying sheet featuring twenty eight columns of windows containing two spikes each (bent in opposite directions), was used to reinforce the DCB laminate. The laminated beams of 1.93 mm thickness and 25 mm width were manufactured by stacking a quasi-isotropic layup [+45°/-45°/0°/90°/0°]s of carbon-fibre Hexply® M21/35%/198/T800S medium grade unidirectional pre-preg layers. Young's modulus in the beam's length direction $(E_x = 83.3\ \text{GPa})$ was calculated through Classical Lamination Theory. The critical strain energy release rate (G_{Ic}) for delamination was obtained by testing an unreinforced DCB beam. The first column of reinforcements was located 0.85 mm away from the pre-crack tip. Fig. 67 depicts the architecture of the DCB laminated reinforced specimen.

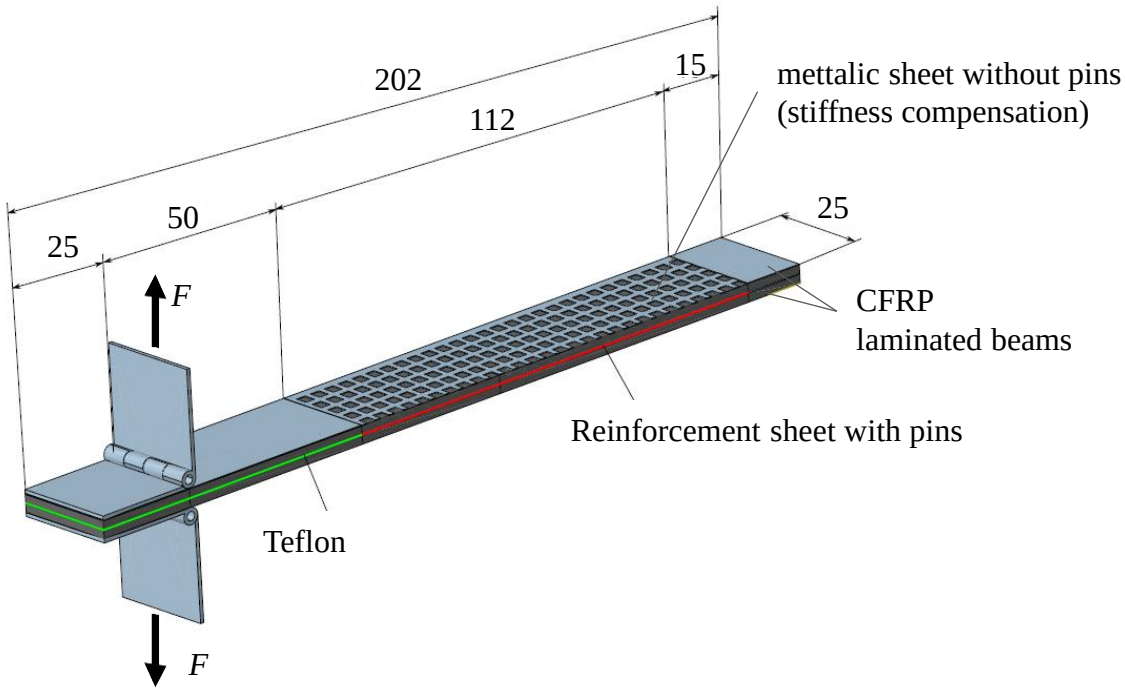

Fig. 67- Architecture of the DCB specimen featuring the metallic reinforcement sheet considered in the current investigation.

Several simulations were performed for different configurations, *i.e.*, reinforcement's material, pin geometry and applied surface pretreatment. Difference between simulated and experimental results was resembling for all investigated configurations. Fig. 68 contrasts between simulated (blue) and experimental (black) results for a DCB specimen featuring a grit blasted stainless steel reinforcing sheet with straight spikes.

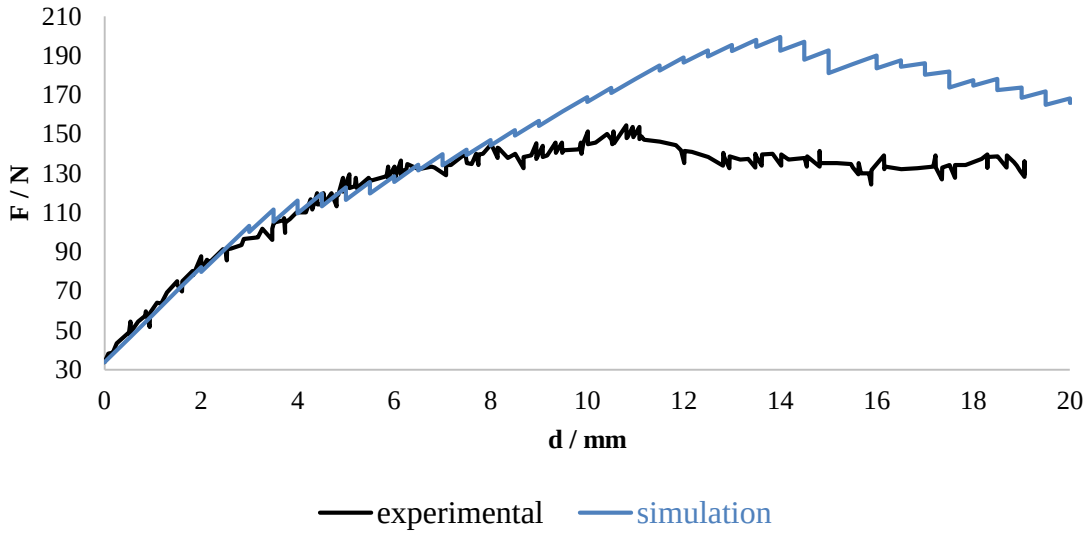

Fig. 68- Load vs. displacement experimental (black line) and analytical (blue line) curve of DCB mode I delamination.

As shown in Fig. 68, simulated results agree well with the experimental data until approximately half of the test trial $(d \approx 10\ \text{mm})$. At this point, the difference between theoretical and experimental results exceeds 15% and significantly increases during the remaining test. However, despite a quantitative mismatch between simulated and experimental data, a qualitative appreciation of Fig. 68 unveils a similar evolution of the two curves. This suggests that for large displacements, the analytical model presented above (chapter 7.3.1) is not suitable for the technology discussed in the current work. Particular assumptions considered for the development of this model are seen as the main cause for this fact.

First of all, as described in chapter 7.3.1, this model considers a symmetrical DCB specimen that can be divided into two identical laminated beams with spikes being pulled out in this same manner throughout the test. However, in practice, spikes are only pulled from within one of the two beams as one side of the integrated carrying sheet is bonded to the other beam (see Fig. 69).

More importantly is that this model assumes that during opening of the delamination crack, pins only provide axial forces. This assumption is appropriate for small displacements. Yet, for larger displacements, pins are subjected to both axial tension and bending, as shown in Fig. 66. Indeed, by accounting the bending effect of the spikes (which probably has a considerable impact when the distance between crack faces is large enough), applied forces would most probably be smaller as part of the spikes' strain energy is dissipated in its deflection rather than in its stretching (crack closing).

Finally, it is also important to point out that for estimation of the critical value of energy release rate, the inappropriate specimen was utilized. A standard laminated DCB beam, featuring no reinforcement was tested and considered as the reference for energy release rate comparison. Thus, defects induced by placing a metallic carrying sheet within the laminated beam were not accounted; a DCB specimen featuring a metallic sheet (with no spikes) is proposed to be used instead. Under that scenario, values of critical energy release rate would have probably been smaller.

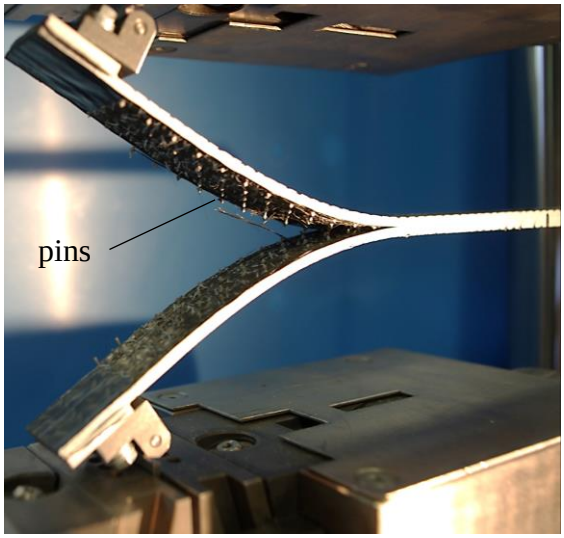

Fig. 69- Picture of a DCB mode I delamination test.

8 Conclusions and outlook

Testing methods were successfully developed and implemented to determine the pull- and shear-out failure behaviour of bent surface structured z-reinforcements. By designing flexible testing procedures with an adjustable tooling system, the same specimen concept was used for the two distinct tests while respecting the specifics and restrictions of the integrated reinforcement structure used in this technology.

The high reproducibility of experimental results allowed the definition of generic pull- and shear-out bridging laws that relate bridging forces of the structured z-reinforcements with crack displacement. The mechanisms by which these metallic reinforcements resist to crack opening or sliding deviates significantly from traditional CF pins [33, 35, 37, 41, 42, 44]. Besides the obvious difference on the reinforcements' geometry, this is explained by the more ductile elasto-plastic failure behaviour exhibited by these metallic z-reinforcements in contrast to the elastically dominated fracture mechanics of CF pins. Hence, no tri-linear (mode I) nor bi-linear (mode II) force-displacement curve was recorded. Yet, the response of this particular spikes to mode II type loads was quite similar to insights from previous related research [36, 43] for titanium reinforcing rods.

Three main stages of the derived bridging laws can be differentiated for both mode I and mixed-mode I/II loading conditions where different energy absorption mechanisms are involved. In the first stage, pins deform elastically only. When interfacial shear stresses reach the shear strength of the bonded pin/resin interface, debonding starts at the bottom of the pin. While a tensioned pin simply stretches along its longitudinal axis, transverse crack displacement induced shear loads provoke bending of the spike around its root. Debonding begins at the bottom pin, somewhere around this stage, when interfacial shear stresses reach the shear strength of the bonded pin/resin interface. From this point onwards, while the bonded part of the pin continues experiencing elastic deformation, the debonded part provides closure forces through interfacial friction. As soon as bridging loads are high enough to trigger plasticization, both force-displacement curves enter the consecutive second stage. This was confirmed through a simple structural approach to the pin's micromechanics, wherein for both loading conditions, calculated values of force required to cause plasticization of the pin fit nicely with those at second stage entry of the bridging laws. Specimens subjected to mixed-mode I/II loads displayed prior to this second stage an elasto-plastic threshold where a high scatter of the curves' shape was detected even within the same configuration. Force-displacement curves' progression at this section is believed to be dependent on the way how resin ploughing occurs during testing, which in turn is associated with the autoclave co-bonding manufacturing process of the specimens. At the beginning of the final third stage, the pin has already debonded completely from the surrounding resin (both loading cases) but forces still increase slightly due to the mechanical interlocking effect of the rough debonded interface. As forces reach their max. value, pin-laminate slipping begins with frictional pull-out as the only mechanism acting against further crack growth. Under shear loads, when the displacement is large enough for pin full-length pull-out, the process remains mechanically stable which can only be accounted for, if one considers the effect of "snubbing" [36, 43], *i.e.* a boosting of frictional forces due to a large contact pressure increase when the pin deflects onto the laminate's crack face.

Consideration of three distinct combinations of specimens allowed the distinction between the impacts of the induced pretreatment (surface morphology and chemistry), of the interlocking effect induced by the spikes' geometry and also of the intrinsic properties from the reinforcement material.

It seems that the mechanisms by which these structured reinforcements provide closure forces against crack opening/sliding are primarily dependent on induced pretreatment morphology scale with adhesion features not necessarily improving the energy dissipation

capacity as opposed to what was suggested in previous investigations [57]. Laser pretreated spikes on the one hand endure higher bridging loads prior to adhesive failure onset. However, as soon as the crack propagates upon the pin, the nano-structure surface lacks of frictional features not only due to a less rough pin's surface but also due to a smoothened debonded interface (nano-cavities of laser-structured surface are infiltrated with resin). By contrast, macro-roughness scale of a grit-blasted surface results in greater amounts of dissipated energy, not only due to enhanced mechanical interlocking, but also due to considerable higher coefficients of friction at the debonded pin/laminate interface.

Material properties also play an important role on the response of these reinforcements to tensile and shear loads. Under mode I loading conditions, a titanium reinforcement benefits from its superior load bearing capabilities whereas a stainless steel spike subjected to shear loads endures higher strains before failure. Imposed displacements during mixed-mode I/II tests were often large enough to exceed the titanium reinforcements' strain to failure, implicating pins' breakage. Despite levels of max. force are practically the same for all titanium configurations, not all of them saw their spikes being sheared-off during testing. It is strongly suggested that is related with the extent of induced pretreatment residual stresses. Those residual stresses can either help relieving or aggravating the state of tension at the pin's critical section. In other words, induced compressive or tensile residual stresses resulting from a grit-blasting or a laser pretreatment are added or subtracted to the applied load, respectively. This explains why even though, bearing load levels are similar for both configurations, a greater number of Al_2O_3 pretreated spikes are sheared-off when compared with those treated by means of laser.

Reinforcements' stiffness also has an important impact on the failure behaviour of these z-reinforced laminates, especially during the first stage of their bridging laws. However, despite the more rigid characteristics of the SAE 304 spikes, Ti 15-3 specimens were generally stiffer. This indicates metal's CTE impact to prevail over stiffness intrinsic features of the spike. A titanium to CF/epoxy interface is exposed to lower residual stresses post-curing cycle due to metal's CTE. This assumption was in fact verified through a simple analytical approach where it is assumed that both cured laminate and reinforcement are free to deform up to an equilibrium situation, *i.e.* until stresses are the same at the interface of both materials. This is then translated into higher coefficients of friction and therefore greater work against pin pull/shear-out due to a smaller gap at the pin/surrounding laminate interface.

Regarding the reinforcement geometry, induced mechanical interlocking effect of an undercut pin geometry overrides adhesion and friction effects. While the impact of the pin's surface morphology is still substantial under mode I loading conditions (particularly at the first stage), application of a surface pretreatment to those spikes featuring an arrowhead shape did not bring up any additional advantage under shear loads. Also, as imposed transversal deformations under mixed-mode I/II loads were already large enough to provoke breakage of some straight titanium pins, the consideration of an undercut geometry for this reinforcement material was proved counterproductive for this test. Given the same surface morphology, it was also verified that both arrowhead and straight reinforcements' force-displacement curves (both tests) follow the same path until sliding onset of the straight spikes. Hence, to conclude this part, it can be stated that the undercut geometry can be seen as an extension of their straight counterparts by increasing max. endured forces and therefore amount of absorbed energy, not necessarily changing the reinforcement failure behaviour. Still, it must be assessed and taken into account the knock-down to the laminate's in-plane properties caused by the microstructural damage due to the insertion of a pin featuring a more severe geometry. This was not a sought issue during this investigation.

A set of specimens was also placed inside a wet oven (75ºC, 85% RH) for 1000 hours to evaluate the impact of exposing z-reinforced laminates to a hot and wet environment, recurrent

in aeronautical structures. Due to time constrains, testing results of those specimens were not included in the current work. Still, first trials suggest an enhancement of both mode I and mixed mode I/II delamination toughness post hot and het exposure, as in [50]. Besides an increased plasticity of the matrix epoxy resin, this can only be accounted by considering that curing process induced thermal in-plane residual stresses are balanced or even overcompensated by laminate's swelling due to water absorption.

At last, despite the more complex failure mechanics of metallic z-reinforcements, a low scatter of pin pull-out results enabled application of the experimental data to a theoretical approach for prediction and description of the mode I delamination process of a DCB specimen reinforced through this technology. The implemented analytical model was based on that developed for CF z-pins [33]. Numerical results agree well with the experimental data (DCB tests performed in previous investigations [57]) up to the middle of the test. From that point onwards, a quantitative discrepancy between theoretical and experimental results exists still with a similar curves' progression. Consideration of a symmetrical pin pull-out process where spikes are tensioned in the same manner from both delamination faces and the disregarding of bending effects are some of the model assumptions that are seen as the main causes for this discrepancy. The use of an inappropriate DCB reference specimen (which did not feature the induced defects of placing a metallic sheet within the laminate) for estimation of the critical energy release rate, is also suggested to have a reciprocal impact on the analytical results.

References

[1] von Hafe Pérez Ferreira da Silva, M.T., et al., *3D-reinforcement techniques for co-bonded CFRP/CFRP and CFRP/Metal joints: a brief review*, in *17th Conference of Sociedade Portuguesa dos Materiais*. 2015, Elsevier ES; submitted for publication: Porto, Portugal.

[2] Juergens, M., et al., *Pull-out testing of multiscale structured metallic z-reinforcements for cfrp laminates.* Composite Part A; submitted for publication, 2015.

[3] Juergens, M., M.T. von Hafe Pérez Ferreira da Silva, and E. Ladstaetter, *Shear out failure behaviour of surface structured metallic z-reinforcements for CFRP laminates and joints*, in *17th European Conference on Composite Materials (ECCM17)*. 2016: Munich.

[4] Soutis, C., *Carbon fiber reinforced plastics in aircraft construction.* Materials Science and Engineering: A, 2005. **412**(1): p. 171-176.

[5] Donnet, J.-B. and R.C. Bansal, *Carbon fibers*. 1998: CRC Press.

[6] Marsh, G., *Airbus A350 XWB update.* Reinforced Plastics, 2010. **54**(6): p. 20-24.

[7] Brosius, D., *Boeing 787 update.* High Performance Composites, 2007. **2007**: p. 56-59.

[8] Kelly, G., *Joining of carbon fibre reinforced plastics for automotive applications.* 2004.

[9] Camanho, P.P. and M. Lambert, *A design methodology for mechanically fastened joints in laminated composite materials.* Composites Science and Technology, 2006. **66**(15): p. 3004-3020.

[10] Fink, A., Camanho, P.P., et al., *Hybrid CFRP/titanium bolted joints: Performance assessment and application to a spacecraft payload adaptor.* Composites Science and Technology, 2010. **70**(2): p. 305-317.

[11] Thoppul, S.D., J. Finegan, and R.F. Gibson, *Mechanics of mechanically fastened joints in polymer–matrix composite structures – A review.* Composites Science and Technology, 2009. **69**(3–4): p. 301-329.

[12] Banea, M. and L.F. da Silva, *Adhesively bonded joints in composite materials: an overview.* Proceedings of the Institution of Mechanical Engineers, Part L: Journal of Materials Design and Applications, 2009. **223**(1): p. 1-18.

[13] Baldan, A., *Adhesively-bonded joints and repairs in metallic alloys, polymers and composite materials: adhesives, adhesion theories and surface pretreatment.* Journal of materials science, 2004. **39**(1): p. 1-49.

[14] Matthews, F., P. Kilty, and E. Godwin, *A review of the strength of joints in fibre-reinforced plastics. Part 2. Adhesively bonded joints.* Composites, 1982. **13**(1): p. 29-37.

[15] Kweon, J.-H., et al., *Failure of carbon composite-to-aluminum joints with combined mechanical fastening and adhesive bonding.* Composite structures, 2006. **75**(1): p. 192-198.

[16] Tong, L., A.P. Mouritz, and M. Bannister, *3D fibre reinforced polymer composites*. 2002: Elsevier.

[17] Sickinger, C. and A. Herrmann. *Structural stitching as a method to design high-performance composites in future*. in *Proceedings TechTextil Symposium*. 2001.

[18] Tong, L., A.P. Mouritz, and M.K. Bannister, *Chapter 8 - Stitched Composites*, in *3D Fibre Reinforced Polymer Composites*, L.T.P.M.K. Bannister, Editor. 2002, Elsevier Science: Oxford. p. 163-204.

[19] Dell'Anno, G., et al., *Exploring mechanical property balance in tufted carbon fabric/epoxy composites.* Composites part A: applied science and manufacturing, 2007. **38**(11): p. 2366-2373.

[20] Cartié, D.D., et al., *3D reinforcement of stiffener-to-skin T-joints by Z-pinning and tufting.* Engineering Fracture Mechanics, 2006. **73**(16): p. 2532-2540.

[21] Chiu, C.-H. and C.-C. Cheng, *Weaving method of 3D woven preforms for advanced composite materials.* Textile research journal, 2003. **73**(1): p. 37-41.

[22] Tong, L., A.P. Mouritz, and M.K. Bannister, *Chapter 9 - Z-Pinned Composites*, in *3D Fibre Reinforced Polymer Composites*, L.T.P.M.K. Bannister, Editor. 2002, Elsevier Science: Oxford. p. 205-218.

[23] Chang, P., A.P. Mouritz, and B.N. Cox, *Flexural properties of z-pinned laminates.* Composites Part A: Applied Science and Manufacturing, 2007. **38**(2): p. 244-251.

[24] Mouritz, A.P., *Review of z-pinned composite laminates.* Composites Part A: Applied Science and Manufacturing, 2007. **38**(12): p. 2383-2397.

[25] Tu, W., F. Guild, and P. Hogg, *Comeld (TM) Joints: A Novel Technique for Bonding Composites and Metal.* RARE METAL MATERIALS AND ENGINEERING, 2009. **38**: p. 134-141.

[26] Ucsnik, S., et al., *Experimental investigation of a novel hybrid metal–composite joining technology.* Composites Part A: Applied Science and Manufacturing, 2010. **41**(3): p. 369-374.

[27] Parkes, P., et al., *Static strength of metal-composite joints with penetrative reinforcement.* Composite Structures, 2014. **118**: p. 250-256.

[28] Ana Carolina, N., D. Klaus, and H. Elke, *Analysis of the Static and Fatigue Strength of a Damage Tolerant 3D-Reinforced Joining Technology on Composite Single Lap Joints*, in *53rd AIAA/ASME/ASCE/AHS/ASC Structures, Structural Dynamics and Materials Conference*. 2012, American Institute of Aeronautics and Astronautics.

[29] Juergens, M., et al., *Influence of an optimized 3D-reinforcement layout on the structural mechanics of co-bonded cfrp joints*, in *16th European Conference on Composite Materials (ECCM16)*. 2014: Seville

[30] Yan, W., H.-Y. Liu, and Y.-W. Mai, *Mode II delamination toughness of z-pinned laminates.* Composites science and technology, 2004. **64**(13): p. 1937-1945.

[31] Cartié, D.D., *Effect of z-fibres™ on the delamination behaviour of carbon-fibre/epoxy laminates*. 2000, Cranfield University.

[32] Liu, H.Y. and Y.W. Mai. *Effects of z-pin reinforcement on interlaminar mode I delamination*. in *Proceedings of the 13th International Conference on Composite Materials, ICCM13, Beijing*. 2001.

[33] Dai, S.-C., et al., *Experimental study on z-pin bridging law by pullout test.* Composites Science and Technology, 2004. **64**(16): p. 2451-2457.

[34] Mouritz, A. and T. Koh, *Re-evaluation of mode I bridging traction modelling for z-pinned laminates based on experimental analysis.* Composites Part B: Engineering, 2014. **56**: p. 797-807.

[35] Liu, H.-Y., W. Yan, and Y.-W. Mai. *On mode I and mode II bridging laws and bridging mechanisms in z-pinned composite laminates*. in *ICF11, Italy 2005*. 2013.

[36] Liu, H.-Y., W. Yan, and Y.-W. Mai, *Z-pin bridging force in composite delamination.* European Structural Integrity Society, 2003. **32**: p. 491-502.

[37] Cartié, D.D.R., B.N. Cox, and N.A. Fleck, *Mechanisms of crack bridging by composite and metallic rods.* Composites Part A: Applied Science and Manufacturing, 2004. **35**(11): p. 1325-1336.

[38] Juergens, M., et al., *Interfacial phenomena of metallic z-reinforced cfrp joints after hydrothermal ageing.* Composite Part A; submitted for publication, 2015.

[39] Liu, H.Y. and W. Yan, *23 - Z-pin bridging in composite delamination*, in *Delamination Behaviour of Composites*, S. Sridharan, Editor. 2008, Woodhead Publishing. p. 674-705.

[40] Yan, W., H.-Y. Liu, and Y.-W. Mai, *Numerical study on the mode I delamination toughness of z-pinned laminates.* Composites science and technology, 2003. **63**(10): p. 1481-1493.

[41] Mouritz, A. and B. Cox, *A mechanistic approach to the properties of stitched laminates.* Composites part A: applied science and manufacturing, 2000. **31**(1): p. 1-27.

[42] Treiber, J., D. Cartié, and I. Partridge. *Determination of crack bridging laws in tufted composites*. in *Proceedings of 17th International conference on composite materials (ICCM-17)*. 2009.

[43] Larsson, F., *Damage tolerance of a stitched carbon/epoxy laminate.* Composites Part A: Applied Science and Manufacturing, 1997. **28**(11): p. 923-934.

[44] Dransfield, K.A., L.K. Jain, and Y.-W. Mai, *On the effects of stitching in CFRPs—I. mode I delamination toughness.* Composites Science and Technology, 1998. **58**(6): p. 815-827.

[45] Jain, L.K., K.A. Dransfield, and Y.-W. Mai, *On the effects of stitching in CFRPs—II. Mode II delamination toughness.* Composites Science and Technology, 1998. **58**(6): p. 829-837.

[46] Mouritz, A.P., et al., *Review of applications for advanced three-dimensional fibre textile composites.* Composites Part A: Applied Science and Manufacturing, 1999. **30**(12): p. 1445-1461.

[47] Chang, P., A.P. Mouritz, and B.N. Cox, *Properties and failure mechanisms of z-pinned laminates in monotonic and cyclic tension.* Composites Part A: Applied Science and Manufacturing, 2006. **37**(10): p. 1501-1513.

[48] Steeves, C.A. and N.A. Fleck, *In-plane properties of composite laminates with through-thickness pin reinforcement.* International Journal of Solids and Structures, 2006. **43**(10): p. 3197-3212.

[49] Cartié, D.D., M. Troulis, and I.K. Partridge, *Delamination of Z-pinned carbon fibre reinforced laminates.* Composites science and Technology, 2006. **66**(6): p. 855-861.

[50] Zhang, X., L. Hounslow, and M. Grassi, *Improvement of low-velocity impact and compression-after-impact performance by z-fibre pinning.* Composites Science and Technology, 2006. **66**(15): p. 2785-2794.

[51] Dickinson, L., G. Farley, and M. Hinders, *Prediction of effective three-dimensional elastic constants of translaminar reinforced composites.* Journal of composite materials, 1999. **33**(11): p. 1002-1029.

[52] Blackburn, J. and P. Hilton, *Producing surface features with a 200 W Yb-fibre laser and the surfi-sculpt® process.* Physics Procedia, 2011. **12**: p. 529-536.

[53] Tu, W., et al., *Optimisation of the protrusion geometry in Comeld™ joints.* Composites Science and Technology, 2011. **71**(6): p. 868-876.

[54] Zhang, H., W. Wen, and H. Cui, *Study on the strength prediction model of Comeld composites joints.* Composites Part B: Engineering, 2012. **43**(8): p. 3310-3317.

[55] Smith, F. and G. Wylde, *Comeld- an innovation in composite to metal joining.* Welding and Cutting, 2005. **4**: p. 182.

[56] Feng, J., H. Zhang, and P. He, *The CMT short-circuiting metal transfer process and its use in thin aluminium sheets welding.* Materials & Design, 2009. **30**(5): p. 1850-1852.

[57] Nogueira, A.C., *Investigation of a damage tolerant joining technology for lightweight structures (Ph.D. Thesis)*. 2015, Technische Universität München.

[58] Parkes, P., R. Butler, and D. Almond. *Growth of damage in additively manufactured metal-composite joints*. in *Proceedings of 15th European conference on composite materials, Venice, Italy*. 2012.

[59] Parkes, P.N., R. Butler, and D.P. Almond. *Fatigue of metal-composite joints with penetrative reinforcement*. in *Proceedings of 54th AIAA/ASME/ASCE/AHS/ASC structures, structural dynamics and materials conference, Boston, USA*. 2013.

[60] Juergens, M., et al., *Influence of surface treatment and design of 3D-Reinforcements on delamination resistance & mechanical properties of CFRP/CFRP joints under static & fatigue loading*, in *20th International Conference on Composite Materials*. 2015: Copenhagen.

[61] Tan, K.T., N. Watanabe, and Y. Iwahori, *Experimental investigation of bridging law for single stitch fibre using interlaminar tension test.* Composite structures, 2010. **92**(6): p. 1399-1409.

[62] Anderson, T.L. and T. Anderson, *Fracture mechanics: fundamentals and applications*. 2005: CRC press.

[63] Davis, J.R., *Stainless steels*. 1994: ASM international.

[64] Donachie, M.J., *Titanium: a technical guide*. 2000: ASM international.

[65] Rosenberg, H.W., *Ti-15-3: a new cold-formable sheet titanium alloy.* JOM, 1983. **35**(11): p. 30-34.

[66] Strohecker, D.E., *Forming of Titanium and Titanium Alloys*. 1967, DTIC Document.

[67] Kurtovic, A., et al., *Laser induced surface nano-structuring of Ti–6Al–4V for adhesive bonding.* International Journal of Adhesion and Adhesives, 2013. **45**(0): p. 112-117.

[68] Mertens, T. and H. Kollek, *On the stability and composition of oxide layers on pre-treated titanium.* International Journal of Adhesion and Adhesives, 2010. **30**(6): p. 466-477.

[69] Bouquet, F., J. Cuntz, and C. Coddet, *Influence of surface treatment on the durability of stainless steel sheets bonded with epoxy.* Journal of adhesion science and technology, 1992. **6**(2): p. 233-242.

[70] Rechner, R., I. Jansen, and E. Beyer, *Influence on the strength and aging resistance of aluminium joints by laser pre-treatment and surface modification.* International Journal of Adhesion and Adhesives, 2010. **30**(7): p. 595-601.

[71] M.Juergens, et al., *Effect of surface treatment for metallic z-reinforcements on interlaminar fracture toughness of cfrp/cfrp joints*, in *SAMPE Conference Proceedings*. 2015, Society for the Advancement of Material and Process Engineering: Baltimore, MD.

[72] Covino, B., et al., *Dissolution behavior of 304 stainless steel in HNO3/HF mixtures.* Metallurgical Transactions A, 1986. **17**(1): p. 137-149.

[73] Reddy, J.N., *Mechanics of laminated composite plates and shells theory and analysis*. 2nd ed ed. 2004, Boca Raton [etc.]: CRC. XXIII, 831.

APPENDIX A: Mode I pull-out test results, SAE 304 reinforcements

Straight pins

St-GB

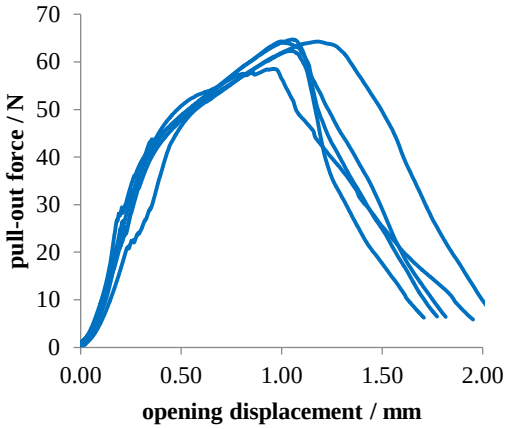

St-HF/HNO3

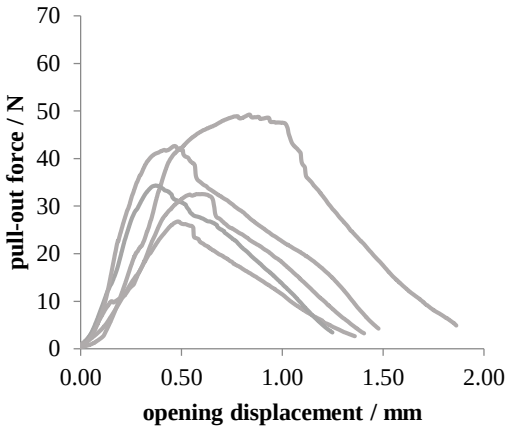

St-La

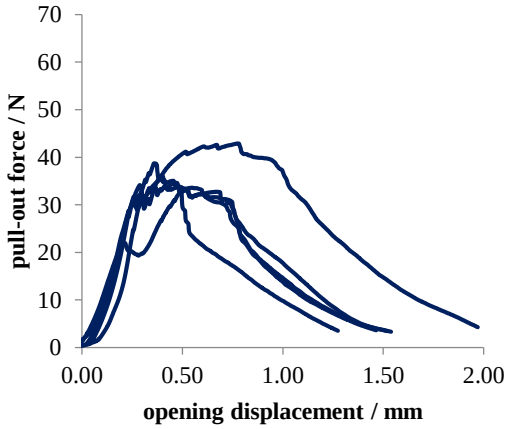

St-RA

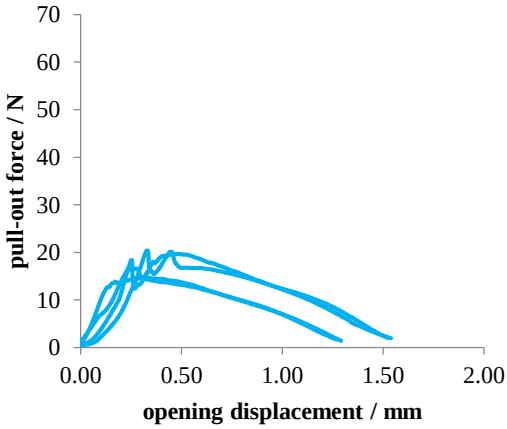

Arrowhead pins

St-La

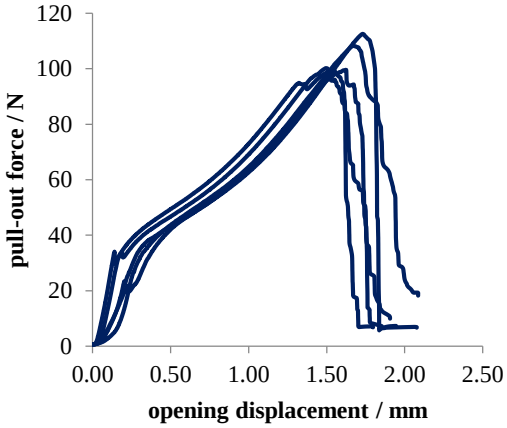

St-RA

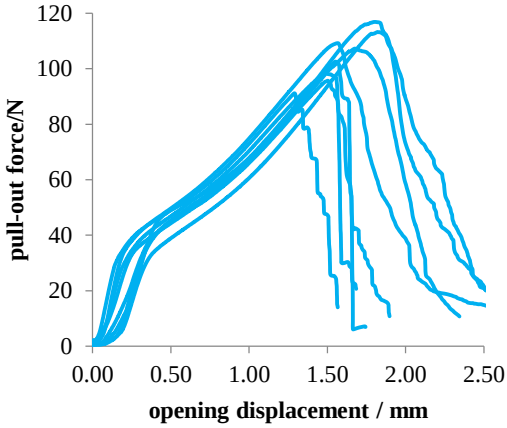

APPENDIX B: Mode I pull-out test results, Ti 15-3 reinforcements

Straight pins

Ti-GB

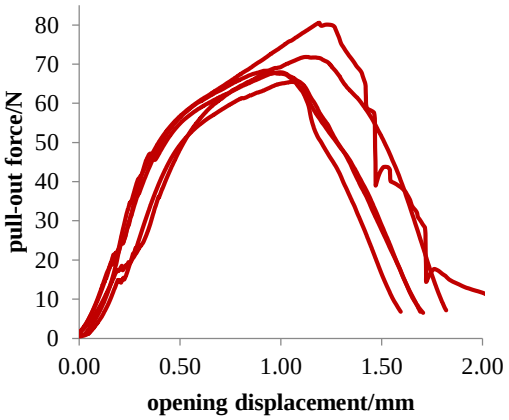

Ti-Turco

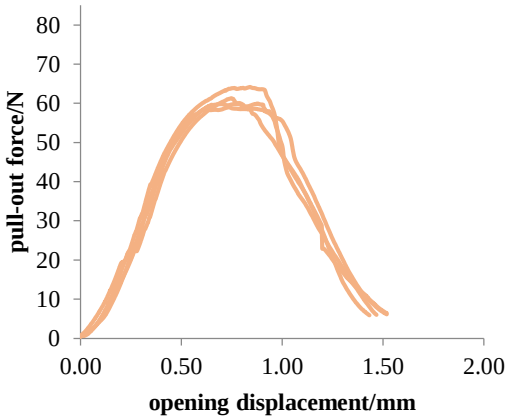

Ti-La

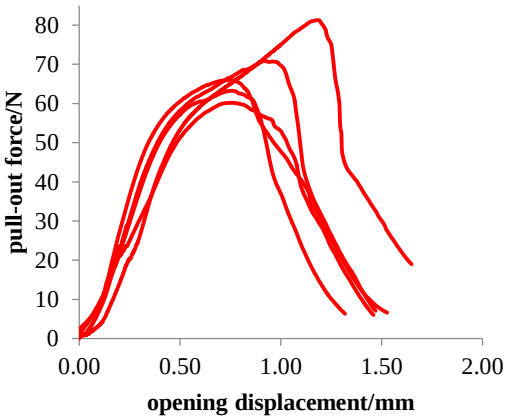

Ti-RA

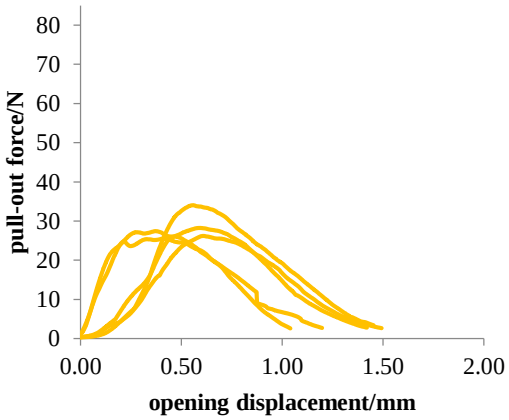

Arrowhead pins

Ti-La

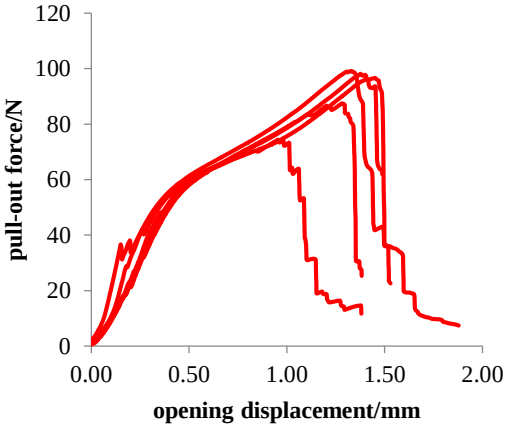

Ti-RA

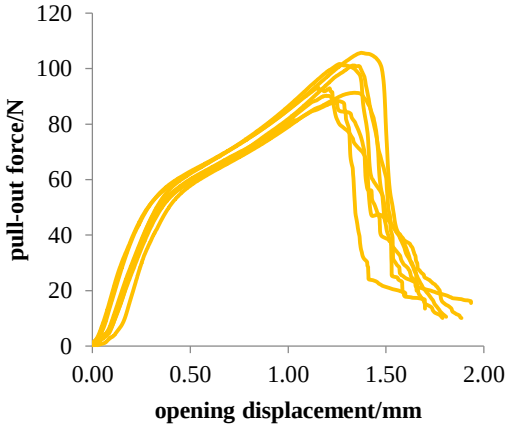

APPENDIX C: Mixed-mode I/II test results, SAE 304 reinforcements

Straight pins

St-GB

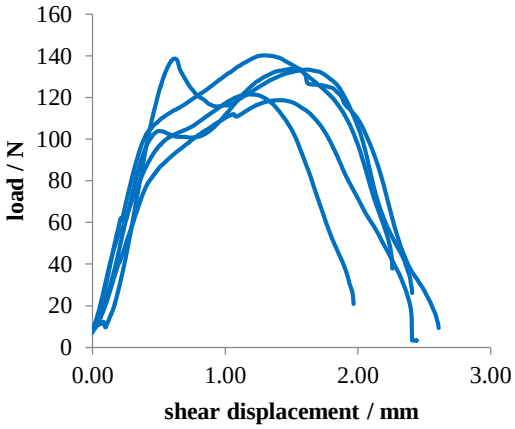

St-HF/HNO3

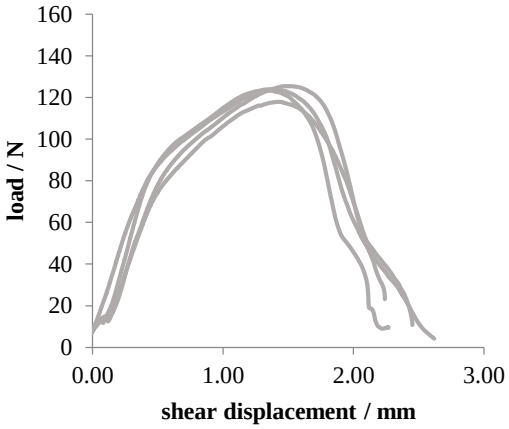

St-La

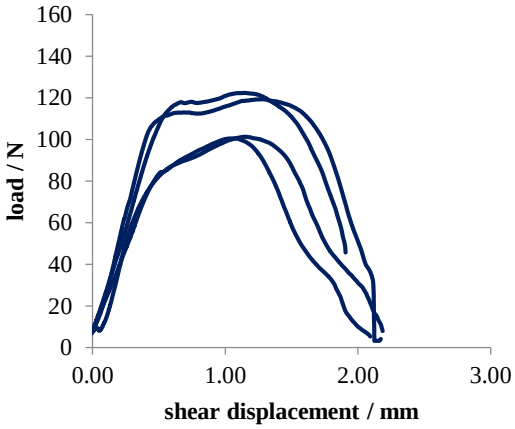

St-RA

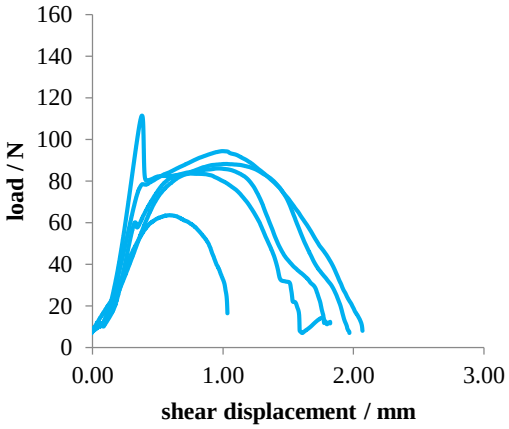

Arrowhead pins

St-La

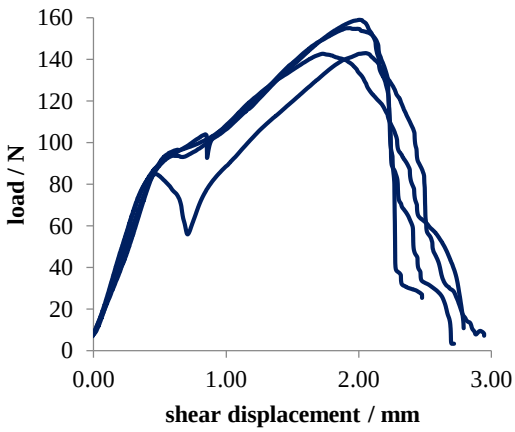

St-RA

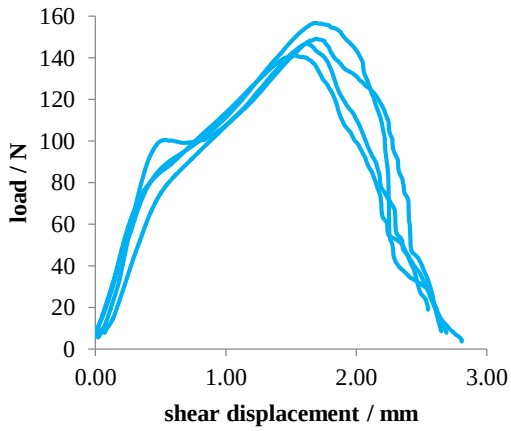

APPENDIX D: Mixed-mode I/II test results, Ti 15-3 reinforcements

Straight pins

Ti-GB

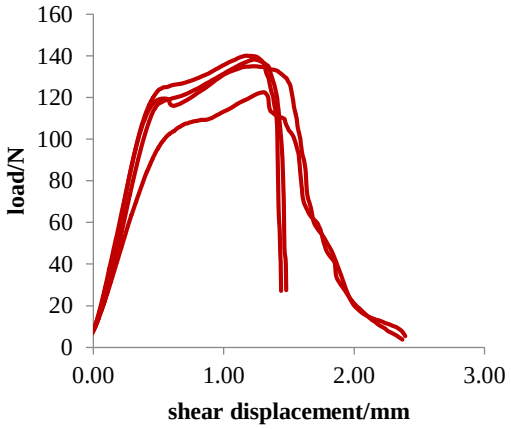

Ti-Turco

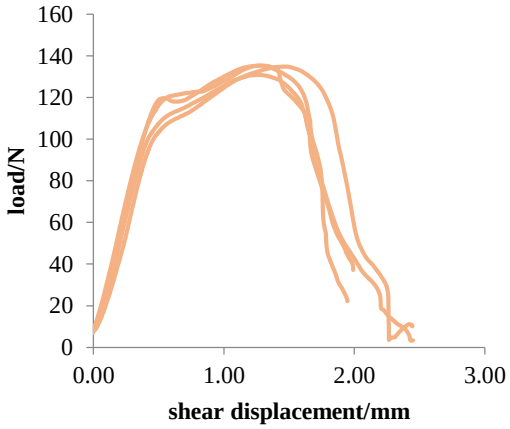

Ti-La

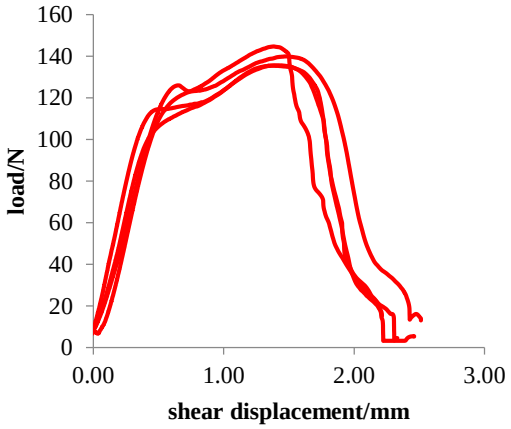

Ti-RA

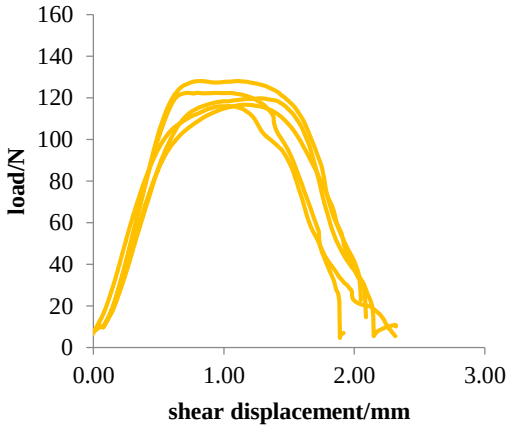

Arrowhead pins

Ti-La

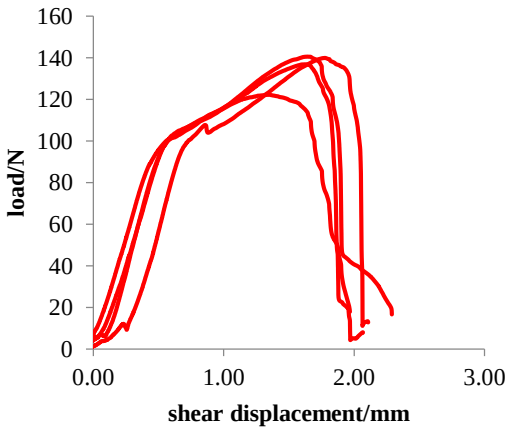

Ti-RA